ABSTRACT

Title of Dissertation: THREE DIMENSIONAL THEORY OF HELIX PASOTRON, A PLASMA-FILLED, BACKWARD WAVE OSCILLATOR

Tamer M. Abu-elfadl, Doctor of Philosophy, 2002

Dissertation directed by: Professor Victor L. Granatstein
Department of Electrical and Computer Engineering

PASOTRONs (Plasma Assisted Slow wave Oscillator) are new high power Cherenkov sources, working without the heavy magnetic field solenoids. Instead of the strong magnetic field, electron transportation in these devices is provided by plasma ions, which compensate the self space charge forces of the beam. The absence of strong guiding magnetic field, gives the electrons the freedom to move transversely by the RF fields besides the usual axial motion in these type of devices. The transverse motion greatly alter the operation of the Cherenkov device. The field intensity of the synchronous space harmonic is concentrated

around the SWS. So, transverse motion can be beneficial in electron wave interaction, as electrons experience this strong field as they move transversely towards the SWS. This stimulated interests in theoretical analysis of these devices.

For symmetrical slow wave structures (SWS), i.e. corrugated waveguide, employed in traveling wave tubes (TWT) and backward wave oscillator (BWO), filled with plasma, it is shown in this study that the operation of these devices can be enhanced by adding a small magnetic field. The small magnetic field helps avoid interception, while maintaining the preferable transverse motion.

A 3D "amplifier" model describing the steady state operation of the helix PASOTRON BWO is presented. The results showed that electrons injected inside the helix are those that contribute most to the device efficiency over those electrons injected outside the helix. It is also shown that by reducing the beam size, high efficiencies up to 55% can be achieved. Such high efficiency, which is unachievable in conventional BWOs driven by linear electron beams, can be explained by a favorable effect of the transverse motion of electrons.

Temporal study of the helix PASOTRON BWO is also presented. It is shown that for zero reflection device, there was no automodulation oscillations. This is attributed to the 3D electron motion together with the 90^o phase difference between the radial and longitudinal field components of the synchronous harmonic. For the non-zero reflection case, the reflection phase greatly affects the device operation.

THREE DIMENSIONAL THEORY OF HELIX PASOTRON, A PLASMA-FILLED, BACKWARD WAVE OSCILLATOR

by

Tamer M. Abu-elfadl

Dissertation submitted to the Faculty of the Graduate School of the
University of Maryland, College Park in partial fulfillment
of the requirements for the degree of
Doctor of Philosophy
2002

Advisory Committee:

Professor Victor L. Granatstein, Chairman/Advisor
Professor Thomas M. Antonsen, Jr.
Professor Wes Lawson
Professor Patrick O'Shea
Dr. Gregory Nusinovich
Professor George Goldenbaum

DEDICATION

To My Parents and My Wife.

ACKNOWLEDGEMENTS

First, I would like to thank Allah for his guidance and blessing to complete this work. I ask him to guide me to the right path through the rest of my life.

I would like to express my thanks and gratitude to my advisor, Prof. Victor Granatstein for his support and guidance during my PhD study. Special thanks go also to Dr. Gregory Nusinovich for his recommendations, which solved a lot of problems throughout my research. I also thank Prof. Thomas Antonsen, Jr. for the fruitful discussions that were of great help. I would also thank Dr. Yuval Carmel and Dr. Anatoly Shkvarunets for the collaboration, which gave the strength to this theoretical study. The communications with Dr. Dan Goebel, who is one of the inventors of the device under study, was very useful. Many thanks go to him. I would like also to thank Prof. Patrick O'Shea and Prof. George Goldenbaum for being in my exam committee.

The PASOTRON project was supported by the Air Force Office for Scientific Research. Their support is appreciated.

Special gratitude goes to my parents for their patience, support and encouragement along my study. Many thanks and appreciations go to my wife Doaa Ghaith for her patience and encouragement, especially during the last stage of my PhD work. Finally, I thank the rest of my family, friends, and colleagues, whom I can not mention their names due to the limited space, for helping and providing a nice environment to work in.

TABLE OF CONTENTS

LIST OF FIGURES

THREE DIMENSIONAL THEORY OF HELIX PASOTRON, A PLASMA-FILLED, BACKWARD WAVE OSCILLATOR

Tamer M. Abu-elfadl

October 25, 2002

This is where I can make all my comments on how the paper is going.

This comment page is not part of the dissertation.

Typeset by LaTeX using the `dissertation` class by Pablo A. Straub, University of Maryland.

Chapter 1

Introduction

1.1 Survey of Relativistic Backward-Wave Oscillators

Backward-wave oscillators (BWOs) are considered sources of coherent Cherenkov radiation. The operation of the BWO is based on the interaction between an electron beam and a synchronous space harmonic of an electromagnetic wave of a slow-wave structure (SWS). While the phase velocity of this wave is close to the electron velocity, the RF power flow is opposite to the streaming direction of the electron beam. This is why the device is called backward wave oscillator. The RF group velocity, which is the velocity of energy propagation, is opposite to the phase velocity of the synchronous harmonic. A slow wave structure (SWS) is employed to reduce the phase velocity of the EM wave, v_{ph}, to the axial velocity of the electrons, v_z, thus providing the condition for Cherenkov interaction. The corrugated waveguide is the typical SWS used, although it could be a helix type, depending on the desired operation frequency and power level. Figure 1.1 sketches the typical SWS employing an annular beam. The guiding of the

beam against its electrostatic forces is provided by a strong magnetic field. The excitation of BWO oscillations was first demonstrated by Kompfner et al. [2] using a ridged waveguide traveling wave amplifier, called a Millman tube [3]. The tube used a low energy electron beam, and showed frequency tunability only by changing the beam voltage. The first BWO employing a relativistic annular beam was by Nation [4] in 1970. He used a cylindrically symmetric, annular, ridged waveguide as a SWS. The output power level was about 10 MW with 0.05% efficiency. A higher efficiency higher power BWO was then developed with efficiency 12-15% [5] and 17% [6], where the measured RF power level was 500 MW. About 1 GW emission was obtained with 25% efficiency in the centimeter wavelength range [7]. Field emission breakdown is one of the limiting factor to the output high power level in this device. To overcome that, overmoded SWS, characterized by larger tube diameter compared to the operating wavelength, were employed [8, 9, 10].

The limitation of the BWO efficiency occurs because of the longitudinal profile of the RF field inside the tube. For matched output of the tube the field profile is zero at the electron downstream end and maximum at the electron entrance. This is disadvantageous to the beam, as the electron beam is bunched by the strong field at the entrance and the RF energy is extracted with interaction with the small field at the outlet. A modification to the tube and guiding magnetic field was performed by El'Chaninov et al. [11] to maximize the device efficiency by increasing the corrugation depth at the electron beam exit, hence increasing the coupling impedance, and reducing the guiding magnetic field allowing the electrons to be closer to the SWS wall where they experience larger field.

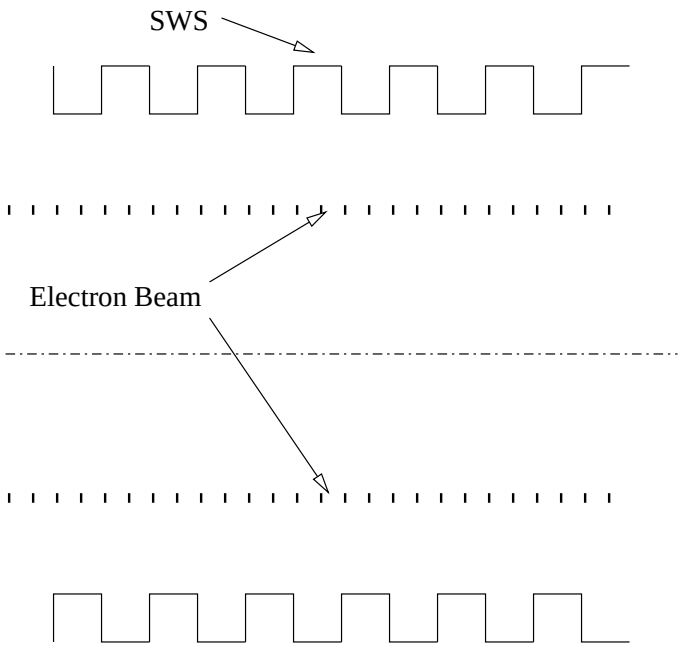

Figure 1.1: Schematic of a corrugated SWS loaded with annular electron beam.

Adding plasma inside the BWO modifies the properties of the RF radiation and the beam transportation through the device. The EM wave dispersion curves are frequency upshifted in the presence of plasma inside the SWS. This frequency upshift was shown theoretically [12], and experimentally [13] for plasma-loaded corrugated wall resonators. Plasma filled BWO sources have many advantages [14] over the conventional vacuum BWO. The maximum electron current that can propagate through the device is increased, due to charge neutralization by the plasma ions. Increase in power and efficiency could also be achieved in the presence of plasma [15, 16]. These increases are due to two reasons. First, the presence of plasma can reduce space charge effects on the electron beam bunches, since the plasma reduces the repulsive debunching forces between electrons by neutralizing some fraction of the bunch space charge. The second reason is the generation of hybrid modes, i.e. slow-wave plasma modes, [17, 18] with increased

on-axis field. Plasma filled BWOs can transport high current exceeding the maximum limiting current transported [19] in the vacuum BWO case. This increase in current carrying capability, enhances the output power of these devices. Reduction in the required guiding magnetic field can also be achieved by adding plasma [19].

In most BWOs, a strong axial magnetic field is applied to guide the electron beam. Correspondingly, only one dimensional interaction is allowed between the axially streaming electrons and the axial electric field of the wave. Applying such a strong magnetic field requires heavy and bulky solenoids.

1.2 PASOTRON (Plasma Assisted Slow-wave Oscillator)

Recently, new devices have been studied; they are called PASOTRONs (Plasma-Assisted Slow-wave Oscillators) [20, 21, 22]. These devices usually operate without guiding magnetic field. The beam transport is provided by the presence of ions which compensate for the space charge forces and thus cause the ion focusing known as the Bennett pinch [23]. The SWS used in PASOTRON BWOs can be either a rippled-wall waveguide (RWG) [20], or a helix [21]. Since helix SWS is known for its wide frequency band operation, very often it is preferred in applications. In recent experiments with the helix PASOTRON BWO [21], efficiencies of up to 30% were obtained by providing RF reflection with the proper phase at the downstream end of the electron beam. Schematic of the experiment setup is shown in Fig. 1.2. The system utilizes a plasma cathode E-gun and a helix SWS installed in an Ultra-High Vacuum (UHV) system. The electron

beam coming out of the plasma gun generates a plasma channel by ionizing a low pressure gas, usually coming out from the electron gun. This plasma channel provides compensation for the space-charge forces. The charge compensation also causes beam focusing (pinching) directly after the gun region due to the beam self magnetic field.

The absence of the strong guiding magnetic field in PASOTRON devices, gives electrons the freedom to move not only axially but also transversely under the action of the RF wave. For symmetrical SWS (e.g. RWG), the effect of this transverse motion on the device operation was studied theoretically in Ref. [24], and will be described in chapter 2. Later, it was shown by the present author and his colleagues [25] that adding a small axial magnetic field in such devices (less than 100 Gauss) could help to increase the efficiency from 20% to about 24% and could help prevent damage to the SWS. For a helix SWS PASOTRON, the obtained efficiency can be even higher. It is shown in chapter 4 and in Ref. [26], that efficiency up to 55% can be achieved.

1.3 Motivation and Dissertation Outline

Helix PASOTRON BWO is an active research topic in the area of High Power Microwave (HPM) sources. The absence of the heavy and bulky solenoid makes the device suitable for many applications. Also the device efficiency is higher than its peer devices of the O-type category which employ steady axial magnetic field to maintain the electrons against their repulsive space charge forces. Due to the absence of a strong guiding magnetic field in the PASOTRON, the beam electrons can experience transverse motion in addition to their usual axial mo-

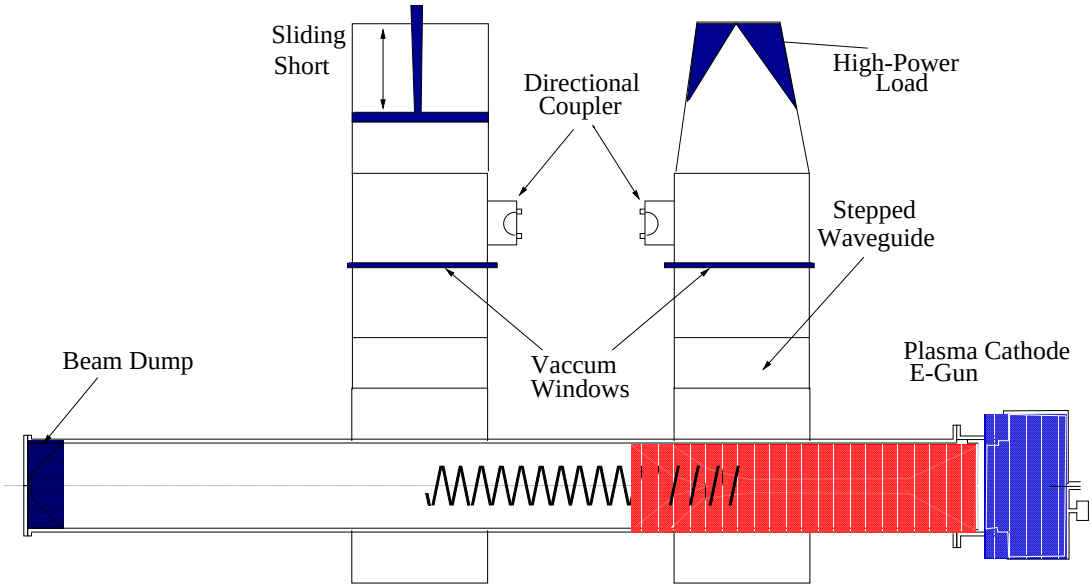

Figure 1.2: Schematic of the helix PASOTRON setup

tion. This transverse motion may cause interception of the beam by the outer tube. Experimental results for helix PASOTRON [27] indicate that the beam current was intercepted at about one third of the SWS length, which enabled a decrease in the device length making it more compact.

From all these considerations, it became clear that it was important to develop a 3-D theoretical model for the operation of the helix PASOTRON BWO. The previous models were one dimensional models, which only describe the axial electron motion. This newly developed theoretical model aims at achieving two goals. First, it should describe the operation of the device explaining its high efficiency compared with previous 1D devices. The other goal is to provide a tool for further optimization of the device performance, i.e. efficiency and temporal behavior.

The dissertation is organized as follows: In chapter 2, the effect of weak magnetic field on the operation of corrugated TWT and BWO tubes is studied,

showing the merit of electron transverse motion. In chapter 3, the properties of the cold helix structure used in the PASOTRON are discussed. In chapter 4, an "amplifier" model for the device is used to predict the device electronic efficiency. A time dependent model of the helix PASOTRON is presented in chapter 5 to study the effect of helix end boundary reflections on the axial mode excitation. Finally, chapter 6 summarizes contributions made in the dissertation.

Chapter 2

Traveling-Wave Tubes and Backward-Wave Oscillators with Weak External Magnetic Field

In this chapter, the operation of the corrugated waveguide PASOTRON in the presence of weak external magnetic field is studied. The beam current is assumed to be annular, with its electrons free to move transversely. In principle, in the absence of guiding magnetic fields, due to the space charge forces and the radial electric field of the wave, the electrons may propagate radially outward which increases electron coupling to the slow wave whose field is localized near the slow-wave structure (SWS). This increases the wave growth rate, and efficiency, and hence, allows one to shorten the interaction region. So the radial electron motion can be beneficial for operation if it does not lead to interception of electrons by the SWS. To avoid this interception a weak external magnetic field can be applied. The theory developed describes the effect of weak magnetic fields on the operation of traveling-wave tubes (TWT) and backward-wave oscillators (BWO) with electrons moving not only axially but also transversely. This theory

allows one to estimate the magnetic field required for protecting the SWS from electron bombardment at different power levels.

2.1 Introduction

Both, traveling wave tubes and backward-wave oscillators can be considered as sources of coherent Cherenkov radiation. The operation of these devices is based on the synchronous interaction between an electron beam and an EM wave. A slow wave structure is employed to reduce the phase velocity of the EM wave, v_{ph}, to the axial velocity of the electrons, v_z, thus providing the condition for Cherenkov interaction. In most of these devices a strong axial magnetic field is applied to guide the electron beam. Correspondingly, only one dimensional interaction is allowed between the axially streaming electrons and the axial electric field of the wave. Applying such a strong magnetic field requires heavy and bulky solenoids. Recently new devices called PASOTRONs (Plasma- Assisted Slow-wave Oscillators) [20, 21] have been developed. These devices usually operate without guiding magnetic field. The beam transport is provided by the presence of ions which compensate for the space charge forces and thus cause the ion focusing known as the Bennett pinch [23].

Even in the case of complete compensation of electron space charge fields, the absence of strong external magnetic field allows electrons to move radially under the action of the radial electric field of the wave. This can be the reason for two effects: a) radial motion outwards increases the coupling impedance, b) transverse interaction increases the growth rate. The linear theory of this interaction was considered in Ref. [28]. In the large-signal regime, however,

this transverse degree of freedom may cause electrons' interception by the SWS. It was shown both in theory [24] and experiments [20, 21] that at large wave intensities, a significant fraction of the electrons can be intercepted by the SWS, which may cause its damage. It seems possible to avoid this interception and, at the same time, to benefit from electron transverse motion by using a weak external magnetic field.

This theoretical study applies the model presented in [24] with the addition of a weak magnetic field. We will show that this magnetic field provides some tuning of the device, and enables the achievement of higher power without electron interception. This tuning can be accomplished by varying the magnetic field strength simultaneously with other parameters of the device in an attempt to attain higher power using an interception-free length of the SWS. It will be shown that a weak axial magnetic field can enhance the efficiency of both the TWT and the BWO.

The chapter is organized as follows. In section 2.2, the formulation of the problem is presented, where the equations describing the electron dynamic and wave evolution are derived. A simplified model is also presented. The dispersion relation for the TWT in the presence of a uniform axial magnetic field is presented in section 2.3. The results of the nonlinear theory for TWT and BWO are presented in section 2.4, where subsections 2.4.1 and 2.4.2 are for TWT and BWO, respectively. The final conclusion is presented in section 2.5.

2.2 Formulation

For symmetric periodic structures, the non-zero components of the symmetric transverse magnetic mode, TM_{0p}, in accordance with the Floquet theorem are

$$\begin{aligned} E_z &= Re\left\{e^{-i\omega t}\sum_n -a_n\frac{g_n}{\omega/c}I_0(g_n r)e^{ik_{zn}z}\right\}, \\ E_r &= Re\left\{e^{-i\omega t}\sum_n ia_n\frac{k_{zn}}{\omega/c}I_1(g_n r)e^{ik_{zn}z}\right\}, \\ B_\theta &= Re\left\{e^{-i\omega t}\sum_n ia_n I_1(g_n r)e^{ik_{zn}z}\right\}. \end{aligned} \tag{2.1}$$

Here $k_{zn} = k_{z0} + 2\pi n/d$ is the axial wavenumber of the nth space harmonic (d is the structure period), and $g_n = \sqrt{k_{zn}^2 - (\omega/c)^2}$ is the transverse wavenumber of a slow wave.

The equations of motion for a charge q moving in the electromagnetic field of a TM-mode and a DC axial magnetic field $B_0\mathbf{e}_z$ can be written in cylindrical coordinates as,

$$\frac{dp_r}{dt} - \gamma m r\dot{\theta}^2 = q\left(E_r + \frac{r\dot{\theta}}{c}B_0 - \frac{p_z}{\gamma mc}B_\theta\right), \tag{2.2a}$$

$$\frac{1}{r}\frac{d}{dt}(\gamma m r^2\dot{\theta}) = -\frac{q}{c}\dot{r}B_0, \tag{2.2b}$$

$$\frac{dp_z}{dt} = q\left(E_z + \frac{p_r}{\gamma mc}B_\theta\right), \tag{2.2c}$$

$$\gamma = \sqrt{1 + \frac{1}{m^2c^2}\left(p_r^2 + \gamma^2 m^2 r^2\dot{\theta}^2 + p_z^2\right)}, \tag{2.2d}$$

where p_r and p_z are the momentum in the radial and axial directions, respectively. From Eq.(2.2b), we can get a constant of motion (the azimuthal canonical momentum P_θ), which is

$$P_\theta = \gamma m r^2\dot{\theta} + \frac{q}{c}\frac{r^2}{2}B_z(z) = const.$$

If we assume that at the entrance the electron beam is annular and thin with an initial radius r_0, and all initial electrons velocities are axial ($\dot{\theta}_0 = 0$), then the constant of motion is $qr_0^2 B_0/2c$, where r_0 is the electron radial position at the entrance. So the equation for $\dot{\theta}$ becomes,

$$\dot{\theta} = \frac{qB_0}{2\gamma m r^2 c}\left(r_0^2 - r^2\right).$$

With this equation we can eliminate $\dot{\theta}$ from Eqs.(2.2). We will also take the independent variable z instead of t , and introduce the slowly variable phase $\psi = k_{z,synch} z - \omega t$, where $k_{z,synch}$ is the axial wavenumber corresponding to the synchronous space harmonic of the wave field in the expansion Eqs.(2.1). For simplicity we normalize the coordinates z and r by ω/c, and the momenta p_z, p_r by $1/mc$. Also, in the equations of motion (2.2), we keep only the synchronous harmonic in the field expansion (2.1), since we assume that the rest of the harmonics are asynchronous with the electron beam. So Eqs.(2.2) become,

$$\frac{dp_r}{dz} = \Omega^2 \frac{r_0^4 - r^4}{p_z r^3} + \left(h\frac{\gamma}{p_z} - 1\right)\hat{I}_1(\kappa r) Im\left\{Ae^{i\psi}\right\}, \tag{2.3a}$$

$$\frac{dp_z}{dz} = \frac{\gamma}{p_z}\kappa\hat{I}_0(\kappa r) Re\left\{Ae^{i\psi}\right\} + \frac{p_r}{p_z}\hat{I}_1(\kappa r) Im\left\{Ae^{i\psi}\right\}, \tag{2.3b}$$

$$\frac{dr}{dz} = \frac{p_r}{p_z}, \qquad \frac{d\psi}{dz} = \Delta + \frac{\gamma_0}{p_{z0}} - \frac{\gamma}{p_z}, \tag{2.3c}$$

$$\gamma = \sqrt{1 + p_r^2 + \Omega^2\left(r_0^2 - r^2 f(z)\right)^2/r^2 + p_z^2}. \tag{2.3d}$$

We have added the two Eqs.(2.3c) to complete the system of equations. In these equations Δ is the detuning factor $\Delta = 1/\beta_{ph} - 1/\beta_{z0}$, where β_{ph} and β_{z0} are, respectively, the wave phase velocity of the synchronous harmonic and the initial electron axial velocity normalized to the speed of light. In Eqs.(2.3), we introduced the normalized non-relativistic Larmor frequency $\Omega = \omega_L/\omega = eB_0/(2cm\omega)$, and the normalized field amplitude $A = eaI_0(gr_0)/(m\omega c)$, where

g is the transverse wavenumber corresponding to the synchronous harmonic $k_{z,synch}$ ($g = \sqrt{k_{z,synch}^2 - \omega^2/c^2}$). Here the modified Bessel function $I_0(gr_0)$ describes the coupling of the axial electric field of the wave to electrons initially located at r_0, which corresponds to consideration of an initially thin annular electron beam. Also we normalized the modified Bessel functions to $I_0(gr_0)$: $\hat{I}_0(gr) = I_0(gr)/I_0(gr_0)$, $\hat{I}_1(gr) = I_1(gr)/I_0(gr_o)$. In Eqs.(2.3a) and (2.3b) $h = k_{z,synch}/(\omega/c)$, and $\kappa = g/(\omega/c)$.

As known, the equation describing the wave excitation can be obtained from Maxwell equations. In the stationary regime, after some manipulations and considering only the synchronous harmonic, this yields the equation for the time independent wave amplitude, which for the TWT has the following form [24], see also Appendix A,

$$\frac{\partial A}{\partial z} = -I\frac{1}{2\pi}\int_{2\pi}\left[\kappa\hat{I}_0(\kappa r) + i\frac{p_r}{p_z}h\hat{I}_1(\kappa r)\right]e^{-i\psi}d\psi_0. \tag{2.4}$$

In Eq.(2.4), we introduced $I = e2I_bI_0^2(gr_{b0})/\left(m\omega^2|N|\right)$, where the norm of the wave N is proportional to the power of the propagating wave. The second term inside the square brackets represents the transverse interaction between the radial electron motion and the radial electric field of the EM wave. For the BWO the 'minus' sign in the RHS of Eq.(2.4) should be replaced by 'plus' because in the BWO the wave propagates in the opposite direction.

In principle, Eqs.(2.3) and (2.4) form a self consistent set of equations which can be integrated numerically. However, for the sake of simplicity, we can impose further assumptions. Let us assume $p_\perp \ll p_z$, where $p_\perp$ is the transverse

momentum. By using this assumption Eqs.(2.3) and (2.4) can be reduced to

$$\frac{d^2\psi}{d\zeta^2} = \hat{I}_0(\rho) Re\left\{\alpha e^{i\psi}\right\}, \tag{2.5a}$$

$$\frac{d^2\rho}{d\zeta^2} = \hat{I}_1(\rho) Im\left\{\alpha e^{i\psi}\right\} + M\frac{\rho_0^4 - \rho^4}{\rho^3}, \tag{2.5b}$$

$$\frac{\partial\alpha}{\partial\zeta} = -\frac{1}{2\pi}\int_{2\pi} \hat{I}_0(\rho) e^{-i\psi} d\psi_0. \tag{2.5c}$$

In Eqs.(2.5) we introduced the Pierce-like gain parameter C, given by $C^3 = I/(\gamma_0^2 - 1)^{5/2}$, and used the normalization $\zeta = Cz$, $\rho = \kappa r$ and $\alpha = A/[C^2(\gamma_0^2 - 1)^2]$. We also introduced the magnetic field parameter $M = \Omega^2/\left(C^2\gamma_0^2\beta_0^2\right)$ (For $M = 0$ this set of equations reduces to those given in Ref. [24].).

Equations (2.3) and (2.4) can be used to calculate the efficiency,

$$\eta = \left(\gamma_0 - \langle\gamma\rangle\right)/\left(\gamma_0 - 1\right).$$

Here, the angular brackets indicate the averaging over electron phases ψ at the entrance. These equations also allow one to derive the energy conservation law which describes the correspondence between the changes in the beam energy given by the efficiency η and the changes in the wave intensity $|A|^2$. For the TWT this relation is given by,

$$|A|^2 - |A_0|^2 = 2I(\gamma_0 - 1)\eta. \tag{2.6}$$

For the BWO with well matched ends, a similar relation is given by,

$$|A_0|^2 = 2I(\gamma_0 - 1)\eta. \tag{2.7}$$

Here $|A_0|^2$ is the wave intensity at the entrance, while at the well matched exit the backward wave intensity equals zero. Note that, when we use the simplified Eqs.(2.5) instead of Eqs.(2.3) and (2.4), the efficiency η can be given as,

$$\eta = (\gamma_0 + 1)\sqrt{\gamma_0^2 - 1}C\hat{\eta}, \tag{2.8}$$

where $\hat{\eta} = \Delta - \langle d\psi/d\zeta \rangle$. Correspondingly, Eqs.(2.6) and (2.7) can be reduced to $\hat{\eta} = \left(|\alpha|^2 - |\alpha_0|^2\right)/2$ for the TWT case and $\hat{\eta} = |\alpha_0|^2/2$ for the BWO case. These relations are the same whether we have a guiding DC magnetic field or not [24].

Finally, let us show the relation between our Pierce-like gain constant C and the well-known Pierce gain C_p given by

$$C_p = \frac{I_b Z_c}{4V_b}.$$

Here I_b is the beam current, Z_c is the interaction impedance between the electron beam and electromagnetic slow wave, and V_b is the beam voltage. The relation between C and C_b can be shown to be

$$C^3 = \frac{4\gamma_0^2\left(\gamma_0 - 1\right)}{\left(\gamma_0^2 - 1\right)^{5/2}} C_p^3.$$

2.3 Small Signal Analysis

By linearizing Eqs.(2.3) and (2.4), one can derive the dispersion equation describing the propagation of EM perturbations through the system. We assume the perturbations in EM wave and electron motion to have axial dependence $\exp i\Gamma z$. After some mathematical manipulations, this yields the following dispersion equation:

$$\left[\left(\Gamma - \Delta\right)\Gamma^2 + \frac{C^3}{2}\right]\left(\Gamma^2 - \frac{4\Omega^2}{\gamma_0^2\beta_{z0}^2}\right) - \frac{C^3}{2}q^2\Gamma^2\left(\Gamma\beta_{z0}\gamma_0^2 - 1\right) = 0, \qquad (2.9)$$

where $q = I_1^2(|g|\, r_{b0})/I_0^2(|g|\, r_{b0})$. In the case of zero magnetic field ($\Omega = 0$), Eq.(2.9) reduces to that derived in Ref. [24].

For small C's, we can introduce $\gamma = 2^{1/3}\Gamma/C$, $\delta = 2^{1/3}\Delta/C$, $\Omega_B = 2^{1/3}(2\Omega)/\left(\gamma_0\beta_{z0}C\right)$.

Then, ignoring the small term $\Gamma\beta_{z0}\gamma_0^2 \sim C\gamma$ reduces Eq.(2.9) to

$$\left[(\gamma-\delta)\,\gamma^2+1\right]\left(\gamma^2-\Omega_B^2\right)+q^2\gamma^2=0. \tag{2.10}$$

Note that, since this equation was extensively studied in Ref.[28], there is no reason to repeat this study. Equation (2.10) is essentially the same as Eq.(13.26) in Ref. [28]: our parameters γ, δ, Ω_0^2 and q^2 correspond to Pierce parameters $i\delta$, b, f^2 and α^2, respectively.

Recall that the study done in Ref. [28] showed that, as the magnetic field increases, the wave growth rate becomes smaller and it has its maximum at larger detuning δ than the case without magnetic field. For instance, when $\Omega_0^2=0$ $(\mathrm{Im}\gamma)_{\max}=\sqrt{3}/2$ and $\delta_{\mathrm{opt}}=0$, while when $\Omega_0^2=10$ $(\mathrm{Im}\gamma)_{\max}\simeq 0.39$ and $\delta_{\mathrm{opt}}\simeq 3.2$. Also note that in Eq.(2.9) which can be rewritten, in accordance with [28], as

$$\gamma-\delta=-\frac{1}{\gamma^2}-\frac{q^2}{\gamma^2-\Omega_B^2} \tag{2.11}$$

we ignored space charge effects. This assumption is quite reasonable for moderate magnetic fields which is the focus of our present study. However, at large magnetic fields the last term in Eq.(2.11) decreases, and correspondingly, the validity of the neglect of space charge effects should be evaluated.

2.4 Nonlinear Results

2.4.1 Traveling Wave Tubes (TWT)

Equations (2.5) can be integrated to obtain the wave amplitude evolution with axial distance. Figures 2.1 show the evolution of $|\alpha|$ versus ζ for different values of the magnetic field parameter M. In Figs. 2.1 the device parameters are: electron

beam initial radius $\rho_0 = 2.0$, wave initial amplitude $\alpha_0 = 0.03$, and SWS radius $\rho_{\mathrm{SWS}} = 4.0$. The saturation of the growth of $|\alpha|$ is mainly due to the electrons' interception by the SWS. The interception starts near the maximum of the $|\alpha|$. We are interested in achieving the maximum before electron interception with the SWS, because electron interception with the SWS may cause RF breakdown. So adding an axial magnetic field can increase the travel distance of electrons before hitting the SWS, and hence increases the maximum wave amplitude that can be achieved before interception.

Further illustration of the effect of the magnetic field is shown in Figs.2.2 and 2.3 for different initial values of $|\alpha|$, where the contours of $|\alpha_{max}|$ are shown in the plane the magnetic field parameter M versus the normalized detuning Δ. All the simulation results are obtained for $r_{sws} = 2r_0$, where r_{sws} and r_0 are the SWS interception radius (the radial distance to the SWS) and electron initial radius, respectively. The corresponding normalized parameters are $\rho_0 = 2$ and $\rho_{sws} = 4$. It is clear from Figs.2.2 and 2.3 that for fixed values of Δ, as we increase M, $|\alpha_{max}|$ initially increases till it reaches its peak. Then, if we further increase M, $|\alpha_{max}|$ decreases. This can be explained as follows. The initial increase of M keeps the electrons away from hitting the SWS for a longer length. So the EM power is enhanced for initial increase of M. Further increase in the magnetic field causes the electrons to be guided away from the SWS. This results in the reduction in the interaction impedance and, correspondingly the maximum power. Note that, as follows from Figs.2.2 and 2.3, even a rather weak magnetic field, which corresponds to $M \leq 0.1$, allows one to increase the maximum wave amplitude from less than 2.0 (for $M = 0$) to 2.6. Since the efficiency, as shown above, is proportional to $|\alpha|^2$, this indicates an efficiency

increase by a factor of 1.7 due to the presence of a weak magnetic field. (The estimates for the magnetic field for BWO case will be given in section 2.4.2.) In case of infinitely strong magnetic field, as follows from [29], the maximum amplitude is equal to 2.52, which yields the efficiency which is 1.6 times larger than in the absence of B_0, but a little smaller than at $M \leq 0.1$.

It is always preferable to avoid interception until the maximum power is achieved, because electron interception with the SWS may cause RF breakdown, which leads to pulse shortening. We denote the distance where the first interception occurs by Z_{int} and the length corresponding to the maximum power ($|\alpha_{max}|$) by Z_{max}. In Figs.2.2 and 2.3 the regions in the $M - \Delta$ plane where $Z_{int} > Z_{max}$ and $Z_{int} < Z_{max}$ are shown. For interception free operation of the device, the length of the device should be designed to be Z_{max}. So, to avoid RF breakdown due to interception, we should tune the device to operate in the region $Z_{int} > Z_{max}$. Note that, as shown in Figs.2.2 and 2.3, at very different levels of the input power, when $\rho_0 = \rho_{SWS}/2$, it is possible to reach the maximum power ($|\alpha_{max}|$) without interception. In all the calculated results, we took $\rho_{SWS} = 4.0$. Our calculations also showed that, when the beam is initially located closer to SWS (for instance $\rho_0 = 3\rho_{SWS}/4$), the interception occurs earlier and restricts the amplitude growth.

2.4.2 Backward Wave Oscillator (BWO)

The equations for the BWO are the same as Eqs.(2.5)for the TWT (see Appendix A for details), except for adding a negative in front of the integral corresponding to change of the group velocity direction. So, Eq.(2.5c) for the evolution of α

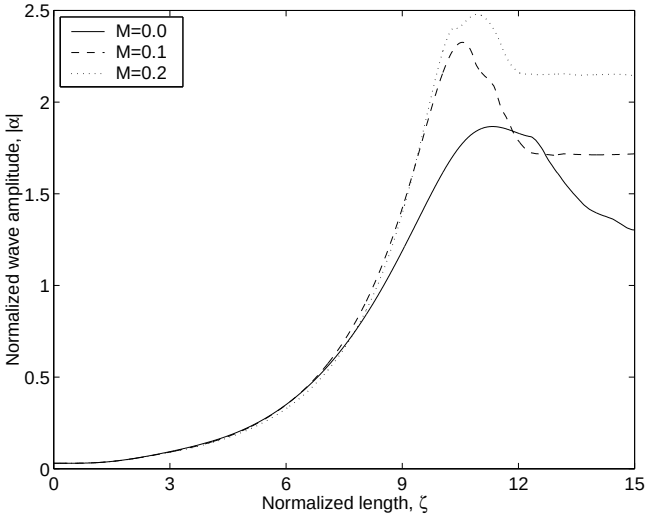

(a) For detuning $\Delta = 1.5$.

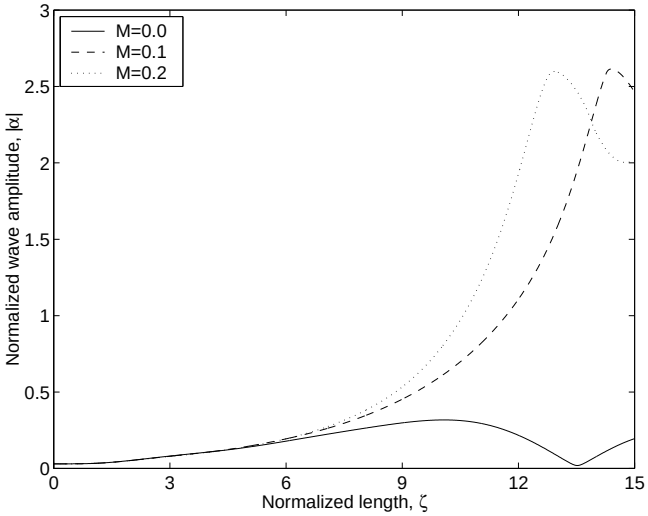

(b) For detuning $\Delta = 1.7$.

Figure 2.1: The normalized wave amplitude profile for the TWT with various values of the magnetic field parameter M. The parameters of the device: $\rho_0 = 2.0$ and $\alpha_0 = 0.03$.

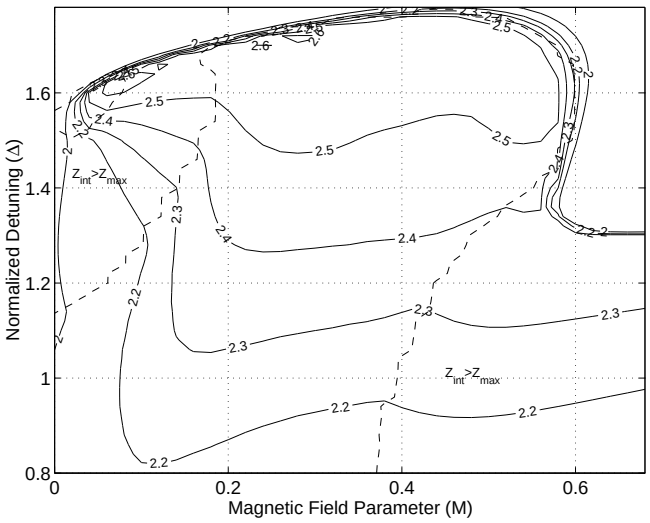

Figure 2.2: TWT contours of $|\alpha_{max}|$. The initial conditions are $\rho_0 = 2.0$, $\alpha_0 = 0.003$, and the device normalized length is 20.0. The dashed lines indicate the borders between the regions where the maximum amplitude can be reached without interception ($Z_{max} < Z_{int}$), and that where interception starts before reaching the maximum ($Z_{max} > Z_{int}$).

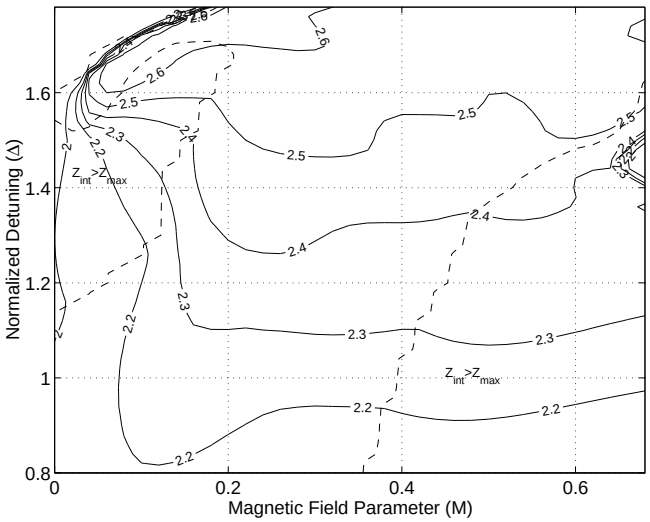

Figure 2.3: TWT contours of $|\alpha_{max}|$. The initial conditions are $\rho_0 = 2.0$, $\alpha_0 = 0.03$, and the device normalized length is 15.0.

becomes,

$$\frac{\partial \alpha}{\partial \zeta} = \frac{1}{2\pi} \int_{2\pi} \hat{I}_0(\rho) e^{-i\psi} d\psi_0.$$

To determine the axial profile of a backward wave envelope, we solved these equations for different initial values of α_0 and for different normalized detunings Δ. We only pick the values of α_0 and Δ that result in a decrease of $|\alpha|$ to zero at some value of ζ, as shown in Fig.2.4. The normalized distance at which $|\alpha| = 0$ is denoted in Fig.2.4 by ζ_0. If we choose our BWO with normalized length ζ_0 and assume its output to be matched, then the solution with that specific α_0 and Δ corresponds to a possible operating mode. Figure 2.5 shows the value of $|\alpha_0|^2$ versus the normalized length ζ_0, for different values of the magnetic parameter M. For each value of M, there is a minimum length $\zeta_{0,min}$ below which there is no oscillation of the BWO. This length is known as the starting length of the BWO [30]. As seen in Fig.2.5, this $\zeta_{0,min}$ slightly increases as we increase the magnetic field parameter M. The increase in $\zeta_{0,min}$ is due to the reduction in the coupling between the electrons and the RF wave with the increase in the magnetic field parameter $M \propto B_0^2$.

In the absence of the axial magnetic field ($M = 0$) Fig. 2.5 shows that for large $|\alpha_0|^2$ (roughly for $|\alpha_0|^2 > 1.8$), there is interception of electrons by the SWS. The maximum $|\alpha_0|^2$ achievable in this case is about 2.2. If we increase M to 0.2 the maximum $|\alpha_0|^2$ can reach 2.8, but this value is achievable for longer length of the device. Further increase of M does not help in enhancing the efficiency of the device. As shown in Fig. 2.5, at $M = 0.4$ the maximum $|\alpha_0|^2$ is smaller than at $M = 0.2$. This can be explained by the decrease in coupling between the electrons and the EM wave, with the increase in M. No interception occurs for values of $M \geq 0.2$.

So far, we considered the BWO with zero reflection at the output end. In real devices, there are some reflections which, as shown in Ref. [31], typically reduce starting current and slightly increase the efficiency. The first effect can be explained by the fact that reflections help to accumulate electromagnetic (EM) energy in the interaction space. The second effect becomes clear, if we recall that the axial structure of the wave envelope with the zero amplitude at the collector end is unfavorable for the efficiency, since electron bunches, being modulated by the strong EM field at the entrance, give up their energy to a weak EM field at the exit.

The value of the Pierce-like gain C used in the simulations is $C = 0.291$. Figure 2.6 shows the device efficiency versus its length for various values of the magnetic field parameter M. For the specific device length of 40 cm, one can see an increase in the efficiency from 20% ($B_z = 0$) to about 24% ($B_z = 45$ Gauss corresponds to $M = 0.2$).

2.5 Conclusion

The operation of plasma-assisted TWTs and BWOs without a strong guiding axial magnetic field has the feature that the electrons can move radially towards the SWS under the influence of the RF fields. Furthermore, the transverse motion is dominated by transverse forces due to RF fields. The proximity of electrons to the SWS increases the coupling between the electrons and the localized field near the SWS. Hence, the output power and the device efficiency increase, and the optimum interaction length shortens. However this radial motion may lead to electron interception by the SWS, which is a major cause of output power satura-

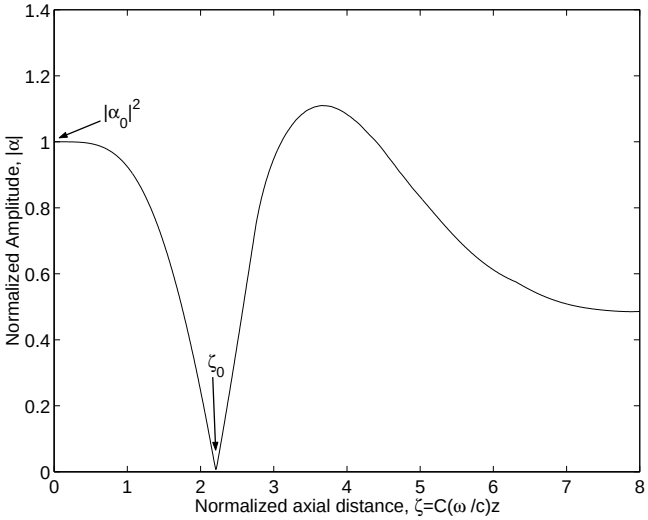

Figure 2.4: Sample output of the evolution of $|\alpha|$ with ζ for BWO. The parameters used are: initial normalized beam radius $\rho_0 = 2.0$, detuning factor $\Delta = 1.48$, and normalized interception radius $\rho_{SWS} = 4.0$.

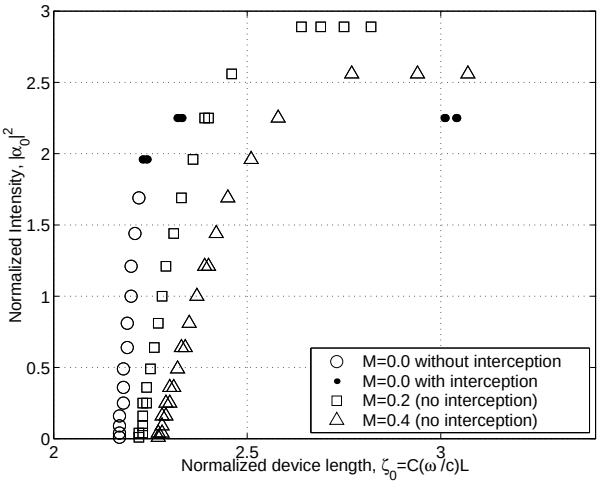

Figure 2.5: Normalized intensity $|\alpha_0|^2$ versus the normalized BWO length ζ_0 for different values of the magnetic field parameter M. The BWO parameters used are: initial normalized beam radius $\rho_0 = 2.0$, and normalized interception radius $\rho_{SWS} = 4.0$.

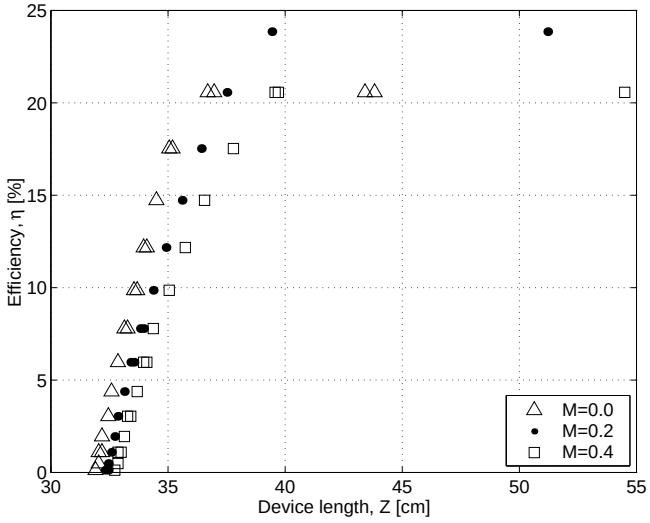

Figure 2.6: The PASOTRON-BWO efficiency η versus its length Z for various values of the magnetic field parameter M. The interception radius of the SWS is $r_{SWS} = 5$ cm. The assumed beam parameters are: beam voltage $V_b = 40$ kV, and initial radius $r_0 = 1.0$ cm. The device operates about 1.2 GHz frequency with the Pierce gain parameter $C = 0.291$.

tion. We showed that adding a weak external magnetic field helps in optimizing their operation in the regimes where we can increase the energy extraction from the beam before electron interception with the SWS occurs. We also showed that magnetic field tapering can reduce the optimum interaction length, which allows one to shorten the device.

For the BWO case, we showed that additional external magnetic field is not always beneficial in enhancing the device efficiency, since the starting (and optimum) length increases with the magnetic field. Therefore, when the interaction length exceeds the starting length only slightly (for $M = 0$), the additional external magnetic field lowers the output power (It can even shut down the device operation). However, for relatively long devices, adding this weak external magnetic field (< 100 Gauss) can enhance the device output power and efficiency.

Chapter 3

PASOTRON Helix Slow Wave Structure

3.1 Introduction

In this chapter we present survey and analysis of the helix used as a slow wave structure, which is usually employed in the PASOTRON BWO. In section 3.2, dispersion curves for the sheath helix are presented. Section 3.3 describes the field structure for a tape helix, where dispersion curves obtained by CHRISTINE [32, 33] for the helix PASOTRON tube are presented. The fields of the first harmonic PASOTRON BWO is presented in section 3.4. These fields are used in the models discussed in subsequent chapters.

3.2 Sheath Helix

The sheath helix is a simplified model to aid in understanding the operation of an actual helix. An actual helix has a certain radius R_h and pitch period λ_h, see Fig. 3.1. Sheath helix can be formed by gathering many helices, having

a common axis and slightly displaced such that the pitch period is filled up. Thus the structure we have would have anisotropic conductivity, infinite along the pitch direction, and zero normal to that direction. The pitch direction is $\hat{\mathbf{e}}_{\phi_p} = \cos\phi_p \mathbf{e}_\theta + \sin\phi_p \mathbf{e}_z$, where $\cot\phi_p = 2\pi R_h/\lambda_h$. The analysis of this helix type was presented by Sensiper [1]. Due to the skew boundary conditions it is necessary to have a hybrid mode (both TE and TM) guided by the structure. The axial electric and magnetic can be written in cylindrical coordinates (r, θ, z) as,

$$E_z(r,\theta,z) = e^{i(kz-n\theta)} \begin{cases} A_n^i I_n(\kappa r), & r < R_h \\ A_n^o K_n(\kappa r), & r > R_h \end{cases}$$

$$B_z(r,\theta,z) = e^{i(kz-n\theta)} \begin{cases} B_n^i I_n(\kappa r), & r < R_h \\ B_n^o K_n(\kappa r), & r > R_h \end{cases},$$

where I_n and K_n are the n^{th} order modified Bessel function of first and second kind, respectively. The variables k and κ are the axial and transverse wavenumbers, respectively, related through $\kappa = \sqrt{k^2 - \omega^2/c^2}$. Applying the skew boundary conditions, (1) the electric field tangential to the helix is continuous with zero component along $\hat{\mathbf{e}}_{\phi_p}$, (2) the magnetic field along $\hat{\mathbf{e}}_{\phi_p}$ is continuous, we get the dispersion relation [1, 34]:

$$\frac{I_n'(\kappa R_h) K_n'(\kappa R_h)}{I_n(\kappa R_h) K_n(\kappa R_h)} = -\frac{(\kappa^2 R_h^2 - nkR_h \cot\phi_p)^2}{(\omega/c)^2 R_h^2 \kappa^2 R_h^2 \cot^2\phi_p}$$

The dispersion relation is plotted in Fig. 3.2 for different modes n. From that figure only waves with phase velocity less than the speed of light $v_{ph} \ll c$ are guided by the helix. Loading a circular waveguide by a sheath helix enables fast modes to propagate besides the slow ones. Analysis of a circular waveguide loaded by a sheath was carried out by Uhm et al. [35].

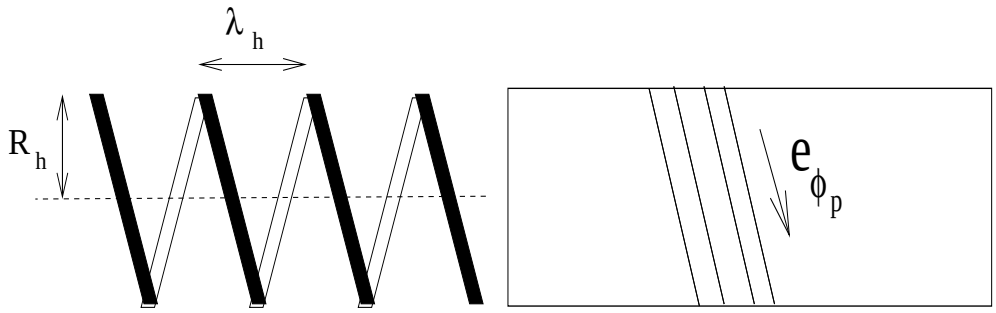

Figure 3.1: The figure on the left is the shape of an actual helix with radius R_h and pitch period λ_h. The sheath helix is shown on the right where the lines show the direction of infinite conductivity along the pitch direction $\hat{\mathbf{e}}_{\phi_p}$.

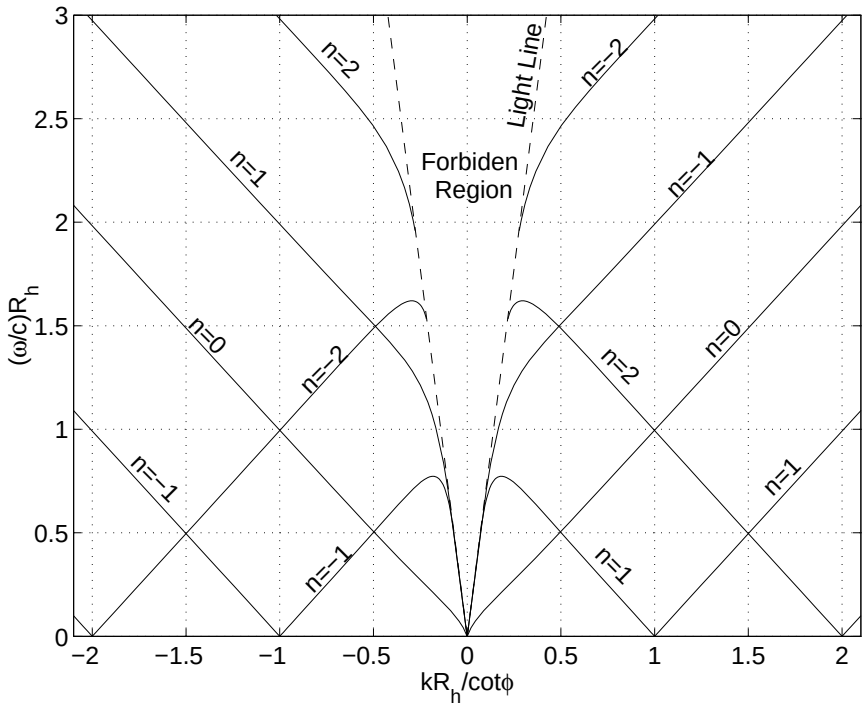

Figure 3.2: Dispersion curves for a sheath helix for different modes n. The helix, for which the dispersion curves are plotted, has $\cot\phi_p = 7.0439$.

3.3 Tape Helix

The sheath helix model gives much information about propagation along the actual helix SWS. Yet, it doesn't manifest the periodicity of the actual helix configuration. To analyze this property the tape helix model is usually used. This model consider a tape helix of small width δ compared to the helix pitch period λ_h ($\delta \ll \lambda_h$). The fields in this periodic structure can be expanded in Floquet spatial harmonics [34]. We use the skew symmetry, i.e. that moving an axial distance z' and rotating along with the helix with an angle $2\pi z'/\lambda_h$, the fields should be the same except of a phase factor $\exp(ikz')$. Thus, when we apply the Floquet theorem, the fields can be represented as,

$$\left\{ \begin{array}{c} \mathbf{E}(r,\theta,z) \\ \mathbf{B}(r,\theta,z) \end{array} \right\} = e^{ikz} \sum_n \left\{ \begin{array}{c} \hat{\mathbf{E}}_n(r) \\ \hat{\mathbf{B}}_n(r) \end{array} \right\} e^{i(2\pi z n/\lambda_h - n\theta)},$$

The dispersion characteristic for the tape helix was also obtained by Sensiper [1], and shown in Fig. 3.3. As in all open periodic structures the dispersion curves for the guided mode is bounded below the light line, such that phase velocity for any space harmonic with axial wavenumber $k_n = k + 2\pi n/\lambda_h$, is less than the speed of light. The $\omega - k_n$ relation for the n^{th} harmonic can be obtained by shifting the origin by n units along the $ka/\cot\phi_p$ axis. The resultant figure will be similar to Fig. 3.2 except for being sliced periodically with forbidden region. So in principle, Fig. 3.2 carries most of the dispersion properties for the different spatial harmonics in the tape helix.

It worth mentioning that although the dispersion characteristic is symmetric for positive and negative wavenumbers, the field structure for k and $-k$ are not the same. In fact we could get the field with $-k$ axial wavenumber from the k

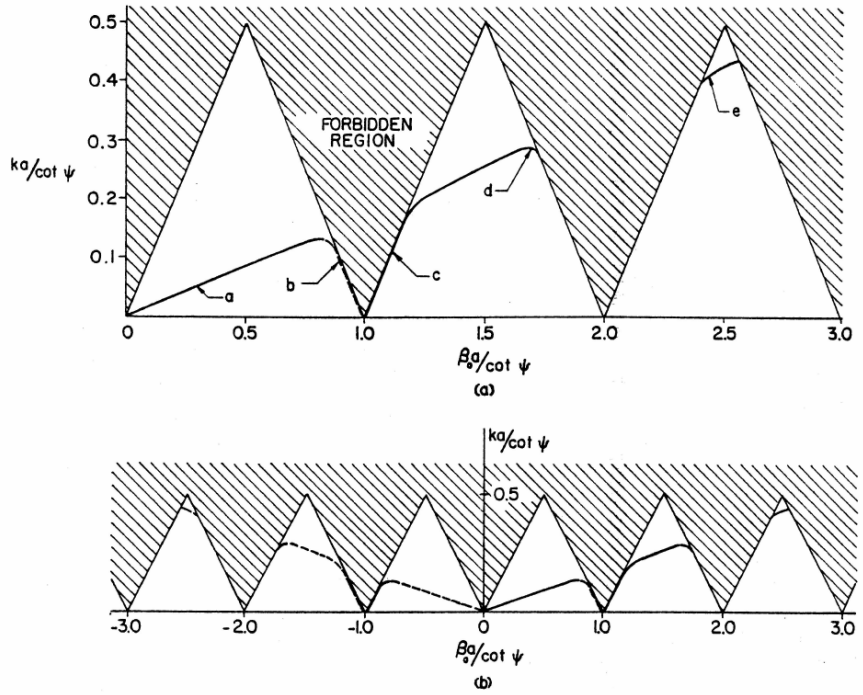

Figure 3.3: (a) and (b)–Solutions of the tape helix determinantal equation, $ka/\cot\phi_p$ for $\phi_p = 10$ degrees, $\pi\delta/\lambda_p = 0.1$, where δ is the tap helix width. (From Ref. [1]: Electromagnetic Wave Propagation on Helix Structures, vol. 43, pp. 155, Proceedings of the IRE 1955)

one, simply by replacing every z, and θ by $-z$, $-\theta$, respectively. From another prospective, the n^{th} harmonic with axial wavenumber k_n, when reflected becomes the $-n^{th}$ harmonic with $-k_n$ wavenumber; see Fig. 3.2.

The circular waveguide loaded by a thin tape helix was studied in Ref. [36]. In that case it was shown that fast waves exist in place of the forbidden regions, which are completely eliminated [36]. Exact treatment of a circular waveguide thin tape helix of arbitrary width in the presence of radially stratified dielectric layer was made by Chernin et al. [32]. Their model was incorporated in the large signal TWT simulation code CHRISTINE [33]. The result of using this code in

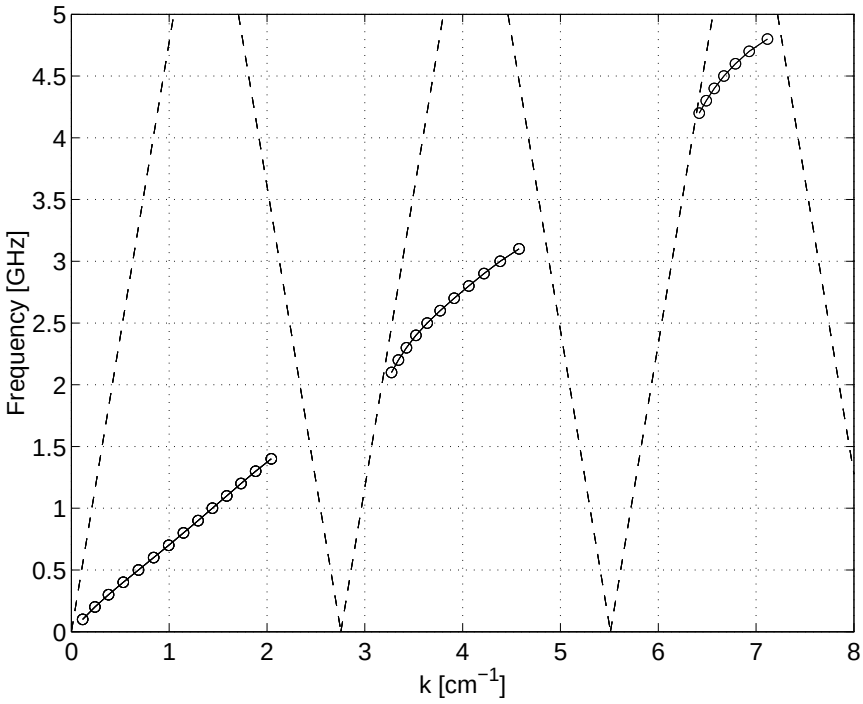

Figure 3.4: Dispersion curve obtained by the code CHRISTINE for the helix PASOTRON with parameters: circular waveguide radius $R_c = 5$ cm, helix radius $R_h = 2.5$ cm, helix pitch period $\lambda_h = 2.28$ cm, and helix tape width $\delta = 0.6$ cm. Only the slow wave solution is obtained by CHRISTINE. The dashed lines are the light lines which separate the slow and fast wave regions.

determining the the exact dispersion curve for PASOTRON helix SWS which has the parameters: circular waveguide radius $R_c = 5$ cm, helix radius $R_h = 2.5$ cm, helix pitch period $\lambda_h = 2.28$ cm, and helix tape width $\delta = 0.6$ cm, is shown in Fig. 3.4. In that figure only the dispersion for the slow wave is computed by CHRISTINE, where it shows that the linear approximation is valid for the helix PASOTRON slow wave dispersion.

In the presence of an electron beam, the beam interacts with the different harmonics, depending on the type of operation of the tube. For TWT amplifier

tubes employing helix SWS, the beam interacts with the zero harmonic, which has positive group velocity close to the velocity of beam electrons, see Fig. 3.2. For BWO oscillator operation, the interaction could be with any of the n=1, n=2,...etc. harmonics, which has negative group velocity. For the PASOTRON helix BWO tube with the parameters described above, only interaction with the first harmonic n=1 was observed in the experiment [37, 27], where RF frequency was approximately 1.2 GHz. So a model that describes the operation of this tube could be built on considering only the interaction of the electron beam with fields of the first harmonic. The radial dependence of the field of that harmonic is obtained in the next section.

3.4 First Harmonic Fields for Helix PASOTRON Tube

The purpose of this section is to describe the fields for the first harmonic in a system shown in Fig. 3.5, i.e. the helix located inside a circular waveguide. To simplify the analysis, the helix is assumed to be a filament or a small tape width helix such that the current flow on the helix is only along the pitch angle direction. As shown in Fig. 3.5, we denote the helix radius, period, and the outer cylinder radius by R_h, λ_h and R_c, respectively. In the absence of an electron beam, the RF fields guided by a helix loaded waveguide can be described by a Floquet series. With the use of the helical symmetry [34], the axial electric and magnetic fields can be written as,

$$E_z(\mathbf{x},t) = \sum_n E_{zn}(r)e^{i(k_n z-\omega t-n\theta)}, \quad B_z(\mathbf{x},t) = \sum_n B_{zn}(r)e^{i(k_n z-\omega t-n\theta)}, \quad (3.1)$$

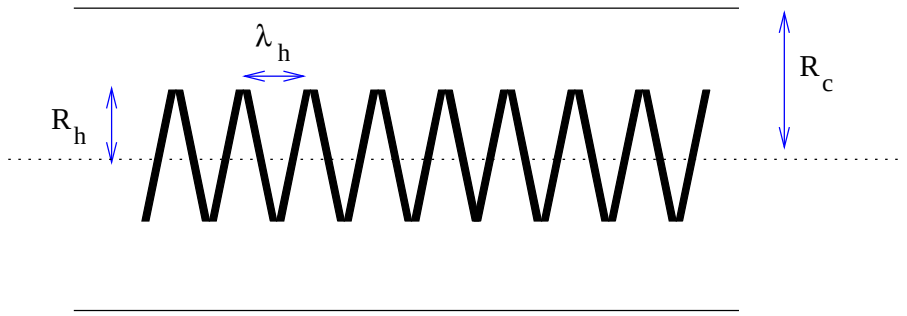

Figure 3.5: Helix inside a circular waveguide.

where $\mathbf{x}$ represents the three coordinates, r, θ and z. For the n^{th} harmonic, the axial wavenumber k_n is equal to $k + 2\pi n/\lambda_h$, where the propagation constant k is determined by the SWS dispersion relation [36, 32], see Figs. 3.4.

As follows from Maxwell equations, the space harmonics of the axial electric and magnetic fields should satisfy the following equation,

$$\left(\frac{1}{r}\frac{\partial}{\partial r}r\frac{\partial}{\partial r} - \frac{n^2}{r^2} - \kappa_n^2\right)\left\{\begin{array}{c} E_{zn} \\ B_{zn} \end{array}\right\} = 0, \tag{3.2}$$

where κ_n is the absolute value of the radial wavenumber defined for the case of slow waves by $\kappa_n^2 = k_n^2 - \omega^2/c^2$. So the solutions for $E_{zn}(r)$ and $B_{zn}(r)$ are given by,

$$E_{zn}(r) = a_n \begin{cases} I_n(\kappa_n r) & 0 \le r \le R_h, \\ I_n(\eta_n)\frac{K_n(\zeta_n)I_n(\kappa_n r) - I_n(\zeta_n)K_n(\kappa_n r)}{K_n(\zeta_n)I_n(\eta_n) - I_n(\zeta_n)K_n(\eta_n)} & R_h \le r \le R_c, \end{cases} \tag{3.3}$$

$$B_{zn}(r) = b_n \begin{cases} I_n(\kappa_n r) & 0 \le r \le R_h, \\ I'_n(\eta_n)\frac{K'_n(\zeta_n)I_n(\kappa_n r) - I'_n(\zeta_n)K_n(\kappa_n r)}{K'_n(\zeta_n)I'_n(\eta_n) - I'_n(\zeta_n)'K'_n(\eta_n)} & R_h \le r \le R_c, \end{cases} \tag{3.4}$$

where $\eta_n^2 = \zeta_n^2 R_h^2/R_c^2 = \kappa_n^2 R_h^2 = (k_n^2 - \omega^2/c^2)R_h^2$, and I_n, K_n are the n^{th} order modified Bessel functions of the first and second kind, respectively. The derivatives of these functions with respect to their arguments, are represented by

I'_n and K'_n. The functional dependence inside and outside the helix are chosen such that $E_{zn}(\kappa_n r)$ and $\partial B_{zn}(\kappa_n r)/\partial r$ are continuous at $r = R_h$ and vanish at $r = R_c$.

Using Maxwell equations, we can represent the transverse field components in terms of of the axial field components,

$$E_{rn}(r) = \frac{1}{\kappa_n^2}\left(-ik_n\frac{\partial}{\partial r}E_{zn}(r) - \frac{\omega}{c}\frac{n}{r}B_{zn}(r)\right), \tag{3.5a}$$

$$E_{\theta n}(r) = \frac{1}{\kappa_n^2}\left(-\frac{nk_n}{r}E_{zn}(r) + i\frac{\omega}{c}\frac{\partial}{\partial r}B_{zn}(r)\right), \tag{3.5b}$$

$$B_{rn}(r) = \frac{1}{\kappa_n^2}\left(-ik_n\frac{\partial}{\partial r}B_{zn}(r) + \frac{\omega}{c}\frac{n}{r}E_{zn}(r)\right), \tag{3.5c}$$

$$B_{\theta n}(r) = \frac{1}{\kappa_n^2}\left(-\frac{nk_n}{r}B_{zn}(r) - i\frac{\omega}{c}\frac{\partial}{\partial r}E_{zn}(r)\right). \tag{3.5d}$$

The relation between the coefficients a_n and b_n in Eqs. (3.3, 3.4) can be obtained by applying the boundary conditions on the tangential magnetic field at $r = R_h$. We assume that the current on the helix is oriented along the helix pitch direction. The helix pitch direction can be represented by a unit vector $\mathbf{e}_{\phi_p}$ given as, $\mathbf{e}_{\phi_p} = \cos\phi_p \mathbf{e}_\theta + \sin\phi_p \mathbf{e}_r$, where ϕ_p is the helix angle given by $\cot\phi_p = 2\pi R_h/\lambda_h$, $\mathbf{e}_r$, and $\mathbf{e}_\theta$ are unit vectors along the radial and azimuthal directions, respectively. So the surface current on the helix is assumed to have the form,

$$\mathbf{J} = J\mathbf{e}_{\phi_p}. \tag{3.6}$$

In accordance with these assumptions, the discontinuity of the tangential magnetic field at $r = R_h$ is given through,

$$B_z^i - B_z^o = \frac{4\pi}{c}J\cos\phi_p, \qquad\qquad B_\theta^i - B_\theta^o = -\frac{4\pi}{c}J\sin\phi_p, \tag{3.7}$$

where the superscript i and o denote the field components at $r = R_h^-$ and $r = R_h^+$, respectively. We can eliminate the current J from the above two equations which

results in,

$$B_\theta^i - B_\theta^o = -\left(B_z^i - B_z^o\right)\tan\phi_p. \tag{3.8}$$

In terms of the Floquet harmonics expansion, this condition is equivalent to

$$B_{\theta n}^i - B_{\theta n}^o = -\left(B_{zn}^i - B_{zn}^o\right)\tan\phi_p \tag{3.9}$$

Substituting with $B_{\theta n}$ from Eq. (3.5d), and after some mathematical manipulations, we obtain the relation between the constants b_n and a_n,

$$b_n = a_n \frac{K_n'(\zeta_n)I_n'(\eta_n) - I_n'(\zeta_n)K_n'(\eta_n)}{K_n(\zeta_n)I_n(\eta_n) - I_n(\zeta_n)K_n(\eta_n)} \frac{I_n(\zeta_n)}{I_n'(\zeta_n)} \frac{i\eta_n\omega/c}{nk_n - \eta_n\kappa_n tan\phi_p} \tag{3.10}$$

All the field components of the n^{th} harmonic can be scaled with the constant a_n. In our study, we are interested in the interaction with the first space harmonic. So we can write the fields of that harmonic as, $\mathbf{E}_1 = a\hat{\mathbf{E}}(r)e^{i(k_1 z - \omega t - \theta)}$, and $\mathbf{B}_1 = a\hat{\mathbf{B}}(r)e^{i(k_1 z - \omega t - \theta)}$. The envelope a has the dimension of the field $\mathbf{E}$ or $\mathbf{B}$, where $\hat{\mathbf{E}}$ and $\hat{\mathbf{B}}$ represent the normalized first space harmonic electric, and magnetic field respectively. These normalized fields can be written as,

$$\begin{aligned} \hat{\mathbf{E}}(\rho) &= -i\hat{E}_r^f(\rho)\hat{\mathbf{e}}_r + \hat{E}_\theta^f(\rho)\hat{\mathbf{e}}_\theta + \hat{E}_z^f(\rho)\hat{\mathbf{e}}_z, \\ \hat{\mathbf{B}}(\rho) &= \hat{B}_r^f(\rho)\hat{\mathbf{e}}_r - i\hat{B}_\theta^f(\rho)\hat{\mathbf{e}}_\theta - i\hat{B}_z^f(\rho)\hat{\mathbf{e}}_z, \end{aligned} \tag{3.11}$$

where k_1 is the axial wavenumber for the first harmonic ($k_1 = k + 2\pi/\lambda_h$), the radial dimension r is normalized to $\rho = \kappa r$, and κ is the absolute value of the transverse wavenumber for the first harmonic ($\kappa^2 = k_1^2 - \omega^2/c^2$). The full expressions for the functions $\hat{E}_r^f(\rho)$, $\hat{E}_\theta^f(\rho)$, $\hat{E}_z^f(\rho)$, $\hat{B}_r^f(\rho)$, $\hat{B}_\theta^f(\rho)$, and $\hat{B}_z^f(\rho)$ are given in Appendix B.

The radial dependence of the electric and magnetic fields for the first spatial harmonic is plotted in Figs. 3.4. In Figs. 3.4, the major field components are along the radial and axial directions, with small components along the azimuthal

direction. These radial and axial fields are maximized at the position of the helix. Concentration of the EM energy close to the slow wave circuit is common to all the SWSs. So to enhance the efficiency of a device employing the SWS, the electron beam has to be close to the slow wave circuit for maximum interaction. This introduces a major problem of beam interception by the slow wave circuit, especially in devices with radial motion like the PASOTRON. Nevertheless, the helix has the advantage of being transparent to most electrons passing through it (a small percentage of electrons is intercepted by the helix conductor), allowing most electrons to experience this large field while passing through the helix.

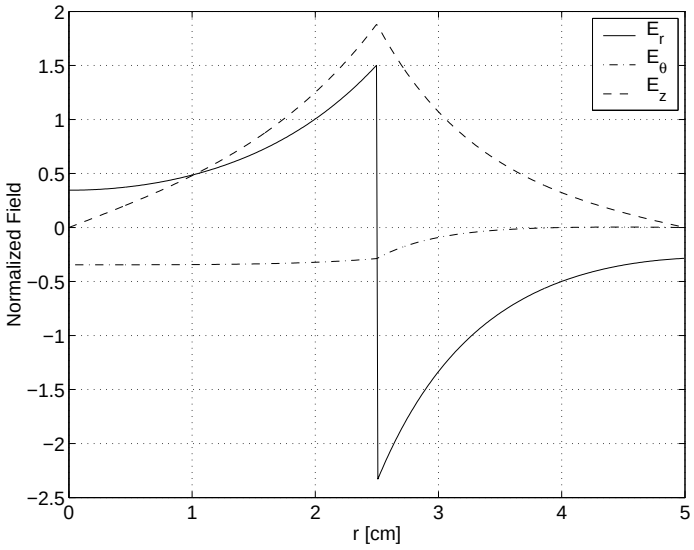

(a) Electric Field Components.

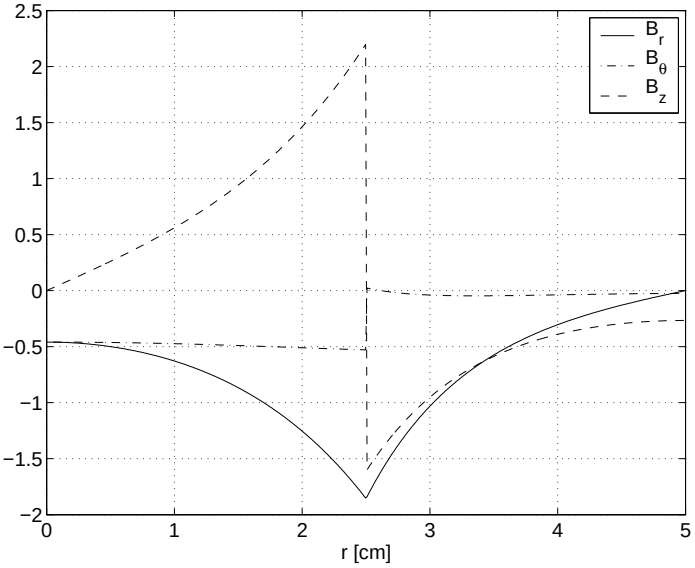

(b) Magnetic Field Components.

Figure 3.6: Normalized electric and magnetic field components for the first harmonic for the helix PASOTRON tube with parameters as in Fig. 3.4, for frequency about 1.2 GHz.

Chapter 4

Efficiency of the Helix PASOTRON Backward Wave Oscillator

4.1 Introduction

In chapter 2, the solution of the electrodynamic system requires solving both the equations of motion and the envelope evolution equation. Under steady state conditions, the beam particles positions and momenta at the entrance to the tube act as the initial conditions for the equations of motion. For the TWT amplifier case, the entrance amplitude of the input RF wave with a given frequency, acts as the initial condition for envelope equation. So the equations of motion and the envelope equation are solved as an initial value problem. When the tube operates as a BWO, the situation becomes complicated. We have to solve for the wave amplitude at the entrance and the RF frequency, given the boundary reflections at both ends of the tube (In chapter 2, for matched end devices, we seek $|\alpha_0|$ and Δ such that the amplitude goes to zero at a certain length). Usually the boundary reflections at both ends are not accurately known from the experiment, and even if an estimate to the boundary reflection can be measured,

its value changes with the adjustable slide at one end of the device (see Fig. 1.2). So, in order to understand the operation of the PASOTRON helix BWO, one takes the approach of solving the initial value problem using an estimate of the amplitude of the backward wave at the entrance and the its frequency. We call this model an "amplifier model", indicating the similarity of solution with the TWT case. The effect of boundary reflection on frequency of operation and different axial mode excitation is the subject of the next chapter.

A 3D "amplifier model" describing the steady state operation of the helix PASOTRON (Plasma-assisted slow-wave oscillator) Backward Wave Oscillator (BWO) is presented. This model contains an equation for the envelope of the wave, whose first space harmonic is synchronous with the electron beam for the case of interaction with the backward wave, and equations for the electron 3D motion under the action of all the field components. In the latter equations, Hamiltonian formulation is used to reduce the number of coordinates to be integrated. The results showed that electrons injected inside the helix are those that contribute most to the device electronic efficiency compared with those electrons injected outside the helix. It is also shown that by reducing the beam size, high efficiencies up to 55% can be achieved. Such high electronic efficiency, which is unachievable in conventional BWOs driven by magnetized electron beams with one-dimensional motion, can be explained by a favorable effect of the transverse motion of electrons.

The absence of the strong guiding magnetic field in PASOTRON BWO tubes, gives electrons the freedom to move not only axially but also transversely under the action of the RF wave. For symmetrical SWS (e.g. RWG), the effect of this transverse motion on the device operation was studied in Ref. [24]. Later, it was

shown in Ref. [25] and in chapter 2 of the present thesis, that adding a small axial magnetic field in such devices (less 100 Gauss) could help to increase the electronic efficiency by about 5%.

In this chapter, we develop the theory describing the operation of the helix PASOTRON BWO. The chapter is organized as follows. In section 4.2 we formulate the problem. First, in subsection 4.2.1, we present the equation describing the field envelope evolution. Then, in subsection 4.2.2, the equations of motion are deduced using the Hamiltonian formalism. The numerical results are presented and discussed in section 4.3. Finally, the conclusion is given in section 4.4.

4.2 Formulation

Below we develop the stationary model of the helix PASOTRON BWO. In our treatment we assume that the helix wires are thin enough, so we can ignore the beam interception by the helix. We also neglect ohmic losses in the device, as the device oscillation frequency is rather low; viz. 1.2 GHz. At so low a frequency the attenuation due to ohmic losses is negligible.

In this model, we assume that the plasma ions provides neutralization for the DC space charge forces of the electron beam (the plasma electrons move faster to the device outer tube). The typical electron beam density at the helix entrance is about $1.6 \times 10^9 \mathrm{cm}^{-3}$ and for a 40 kV beam this corresponds to about a 35 cm plasma oscillation length (Geometrical factor makes that length even larger). Due to beam spread by the RF field, the beam density is very small away from the helix entrance and the effective beam plasma oscillation length is

much larger than helix length which is about 40 cm. Thus the beam AC space charge effect is neglected.

The RF slow wave is guided by the SWS shown in Fig. 3.5, where R_h, λ_h and R_c denote the helix radius, helix period, and the outer cylinder radius, respectively. According to the output frequency range of the helix PASOTRON BWO, we can assume the first spatial harmonic is the only synchronous harmonic with the electron beam. So the envelope evolution equation and equations of motion encounters only this harmonic whose field components are given in appendix B.

4.2.1 Envelope Evolution Equation

The total field inside the periodic structure is represented as a Floquet sum of spatial harmonics ($\boldsymbol{\mathcal{E}}_{\text{tot}} = \sum_n \boldsymbol{\mathcal{E}}_n = \sum_n Re\{\epsilon(z,t)\hat{\mathbf{E}}_n(r)e^{i(k_n z-\omega t-n\theta)}\}$, see appendix B). The stationary envelope evolution equation for $\epsilon(z)$ obtained in appendix A is

$$\frac{\partial\epsilon(z)}{\partial z} = -\frac{k_1^2 Z_{int} I}{\left|\hat{E}_z\right|^2}\left\langle \frac{\mathbf{v}}{v_z}\cdot\hat{\mathbf{E}}^*(r)e^{-i\psi}\right\rangle_{\text{beam},\,\psi_0} \tag{4.1}$$

where

ψ is the electron phase with respect to the RF wave, $\psi = k_1 z-\omega t-\theta$;

$\langle\ldots\rangle_{\text{beam},\,\psi_0}$ indicates averaging over the distribution in the initial radius r_0 and the initial phase ψ_0, $\langle\ldots\rangle_{\text{beam},\,\psi_0} = \int\int\ldots r_0 dr_0 d\psi_0/(\pi R_b^2)$

R_b is the initial beam radius;

I is the total input current;

$|\hat{E}_z|$ is the normalized axial electric field amplitude of the first harmonic (see Fig. 3.4) evaluated at $r = R_b$;

Z_{int} is the interaction impedance defined as, $Z_{int} = |E_{z1}(R_b)|^2 / (2k_1^2 P_r)$, where P_r is the total power flow, and $|E_{z1}(R_b)|$ is magnitude of the axial electric field for the first harmonic evaluated at R_b corresponding to that power flow P_r (Note that the ratio of $Z_{int}/|\hat{E}_{z1}|^2$ doesn't depend on R_b). The actual helix in the PASOTRON is made of a tube with circular cross section, but for simplicity the interaction impedance Z_{int} was calculated by using the code CHRISTINE [32], which uses a tape helix model. The geometrical parameters used with CHRISTINE are $R_h = 2.5$ cm, $R_c = 5$ cm, $\lambda_h = 2.28$ cm and 6 mm helix tape width.

In general, the product $\mathbf{v} \cdot \hat{\mathbf{E}}_1^*$ contains contributions from both axial $v_z \hat{E}_{z1}^*$ and radial $v_r \hat{E}_{r1}^*$ interactions. The radial dependence of the field components is illustrated in Fig. 3.4. The helix parameters used in Fig. 3.4 are $R_h = 2.5$ cm, $R_c = 5$ cm, $\lambda_h = 2.28$ cm, and the operating frequency is 1.26 GHz, which correspond to the PASOTRON experiment at the University of Maryland [37, 27].

4.2.2 Equations of Motion

The Hamiltonian formulation is used to reduce the number of differential equations required to describe the electron motion, by introducing a transformation which makes one of the coordinates cyclic and its corresponding momentum to be a constant of the motion. For fields under consideration, the instantaneous magnetic potential vector is given by,

$$\mathcal{A} = Re\{a(z)\hat{\mathbf{E}}\}, \tag{4.2}$$

where $a(z)$ is related to $\epsilon(z)$ in Eq. (4.1) by $a(z) = (c/i\omega)\epsilon(z)$. Thus, the Hamiltonian in cylindrical coordinates is given by,

$$H = c\left[m^2c^2 + \left(p_r - q\hat{E}_r^f(\kappa r)Im\{a(z)e^{i\psi}\}/c\right)^2 + \left(\frac{p_\theta - qr\hat{E}_\theta^f(\kappa r)Re\{a(z)e^{i\psi}\}/c}{r}\right)^2 + \left(p_z - q\hat{E}_z^f(\kappa r)Re\{a(z)e^{i\psi}\}/c\right)^2\right]^{1/2}, \quad (4.3)$$

where q is the particle charge, which is $q = -e$ for electron with absolute charge e; m is its mass; and c is the speed of light. The functions $\hat{E}_r^f(\kappa r)$, $\hat{E}_\theta^f(\kappa r)$, and $\hat{E}_z^f(\kappa r)$ are defined in the Appendix B. This Hamiltonian description can be obtained after substituting the magnetic potential vector, and $\hat{\mathbf{E}}$ from Eqs. (3.11) in the Hamiltonian formula for cylindrical coordinates (see for example Ref. [38]). As we are dealing with a steady state field profile, without any temporal variation, it is appropriate to take the axial distance z as an independent parameter instead of the time t. This is done through the variational principle,

$$\delta \int \left(p_r\dot{r} + p_\theta\dot{\theta} + p_z\dot{z} - H\right)dt = 0, \quad (4.4)$$

$$\delta \int (p_r dr + p_\theta d\theta + p_z dz + p_t dt) = 0, \quad (4.5)$$

In Eq. (4.5), $p_t = -H$ becomes the canonical momentum to the time variable t. Equation (4.5) keeps its form, if we make the following normalizations: $\hat{t} = \omega t$, $\hat{z} = (\omega/c)z$, $\rho = \kappa r$, $\hat{p}_t = -H/mc^2$, $\hat{p}_z = p_z/mc$, $\hat{p}_\rho = p_r/(gmc)$, $\hat{p}_\theta = \omega p_\theta/(mc^2)$, and $\hat{a}(z) = ea(z)/mc^2$, where κ is the first harmonic transverse wavenumber and $g = \kappa/(\omega/c)$ is its normalization. So Eq. (4.5) can be written in the form,

$$\delta \int \left(\hat{p}_\rho\rho' + \hat{p}_\theta\theta' + \hat{p}_t\hat{t}' - (-\hat{p}_z)\right)d\hat{z} = 0, \quad (4.6)$$

where prime superscript indicates total derivative with respect to $\hat{z}$. The form of Eq. (4.6) indicates that $-\hat{p}_z$ can be used as the new Hamiltonian with $\hat{z}$ as an

independent variable instead of $\hat{t}$ which becomes one of the canonical variable with the conjugate momentum $\hat{p}_t$. The new Hamiltonian in this description is H_1, which is given by,

$$\begin{aligned} H_1(\theta, \hat{p}_\theta; \rho, \hat{p}_r; \hat{t}, \hat{p}_t; \hat{z}) &= -\hat{p}_z, \\ &= -\left[\hat{p}_t^2 - \left(g\hat{p}_\rho + \hat{E}_r^f(\rho) Im\{\hat{a}(z)e^{i\psi}\}\right)^2 - \right. \\ &\left. \left(\frac{g\hat{p}_\theta + \rho\hat{E}_\theta^f(\rho) Re\{\hat{a}(z)e^{i\psi}\}}{\rho}\right)^2 - 1\right]^{1/2} + \hat{E}_z^f(\rho) Re\{\hat{a}(z)e^{i\psi}\}, \end{aligned} \tag{4.7}$$

where $\psi = h\hat{z} - \hat{t} - \theta$ and $h = k/(\omega/c)$ is the normalized longitudinal wavenumber. We make the transformation $\hat{t}$, $\hat{p}_t$, θ, $\hat{p}_\theta \rightarrow \psi$, P_ψ, θ, P_θ, through the generating function $F = (h\hat{z} - \hat{t} - \theta)P_\psi + \theta P_\theta$; see Ref. [39]. This yields: $P_\psi = \gamma$, $P_\theta = \hat{p}_\theta + \gamma$, where γ is the ratio of electron total energy to the electron rest energy.

So the canonical variables are $\rho, \hat{p}_\rho$; θ, P_θ; ψ, γ, and the new Hamiltonian is given by,

$$\begin{aligned} H_2(\rho, \hat{p}_\rho; \theta, P_\theta; \psi, \gamma) = h\gamma + \hat{E}_z^f(\rho) Re\{\hat{a}(z)e^{i\psi}\} - \left[\gamma^2 - \left(g\hat{p}_\rho + \hat{E}_r^f(\rho) Im\{\hat{a}(z)e^{i\psi}\}\right)^2 - \right. \\ \left. \left(\frac{g(P_\theta - \gamma) + \rho\hat{E}_\theta^f(\rho) Re\{\hat{a}(z)e^{i\psi}\}}{\rho}\right)^2 - 1\right]^{1/2}, \end{aligned} \tag{4.8}$$

Notice that new coordinates are ρ, θ, ψ, and their corresponding canonical momenta are $\hat{p}_\rho$, P_θ, γ, respectively. The new Hamiltonian is independent of θ, which makes P_θ a constant of motion. Thus, the Hamiltonian equations for the

rest of coordinates are:

$$\frac{d\psi}{d\hat{z}} = h - \frac{\gamma}{S_z} - \frac{S_\theta g}{S_z \rho}, \tag{4.9}$$

$$\frac{d\gamma}{d\hat{z}} = \hat{E}_z^f(\rho) Im\{\hat{a}(z)e^{i\psi}\} - \frac{S_\rho}{S_z}\hat{E}_r^f(\rho) Re\{\hat{a}(z)e^{i\psi}\} + \frac{S_\theta}{S_z}\hat{E}_\theta^f(\rho) Im\{\hat{a}(z)e^{i\psi}\}, \tag{4.10}$$

$$\frac{d\rho}{d\hat{z}} = \frac{S_\rho g}{S_z}, \tag{4.11}$$

$$\begin{aligned}\frac{d\hat{p}_\rho}{d\hat{z}} = &-\frac{\partial \hat{E}_z^f(\rho)}{\partial \rho} Re\{\hat{a}(z)e^{i\psi}\} - \frac{S_\rho}{S_z}\frac{\partial \hat{E}_r^f(\rho)}{\partial \rho} Im\{\hat{a}(z)e^{i\psi}\} \\ &+ \frac{S_\theta}{S_z}\left(\frac{g(P_\theta - \gamma)}{\rho^2} - \frac{\partial \hat{E}_\theta^f(\rho)}{\partial \rho} Re\{\hat{a}(z)e^{i\psi}\}\right)\end{aligned} \tag{4.12}$$

where S_ρ, S_θ and S_z are given by, $S_\theta = \left(g(P_\theta - \gamma) + \rho \hat{E}_\theta^f(\rho) Re\{\hat{a}(z)e^{i\psi}\}\right)/\rho$, $S_\rho = g\hat{p}_\rho + \hat{E}_r^f(\rho) Im\{\hat{a}(z)e^{i\psi}\}$, and $S_z = \sqrt{\gamma^2 - S_\rho^2 - S_\theta^2 - 1}$, respectively. The vector $\mathbf{S}$ is given by, $\mathbf{S} = S_\rho \hat{\mathbf{e}}_r + S_\theta \hat{\mathbf{e}}_\theta + S_z \hat{\mathbf{e}}_z = \gamma \mathbf{v}/c$.

Due to the discontinuity in the radial field shown in Fig. 3.4, the canonical momentum $\hat{p}_\rho$ is also discontinuous at the helix position. For the purpose of numerical integration, it is convenient to use the continuous quantity $S_\rho = \gamma \dot{r}/c$, instead of $\hat{p}_r$. So we replace Eq. (4.12) by,

$$\begin{aligned}\frac{dS_\rho}{d\hat{z}} = &-g\frac{\partial \hat{E}_z^f(\rho)}{\partial \rho} Re\{\hat{a}(z)e^{i\psi}\} + \frac{gS_\theta}{S_z}\left(\frac{g(P_\theta - \gamma)}{\rho^2} - \frac{\partial \hat{E}_\theta^f(\rho)}{\partial \rho} Re\{\hat{a}(z)e^{i\psi}\}\right) \\ &+ \frac{d\psi}{d\hat{z}}\hat{E}_r^f(\rho) Re\{\hat{a}(z)e^{i\psi}\}.\end{aligned} \tag{4.13}$$

In deriving Eq. (4.13) from Eq. (4.12), we neglected the term containing $d\hat{a}(z)/d\hat{z}$. We assume that the transverse variation of the axial field dominates the axial variation ($\frac{d}{d\hat{z}} Log\,|\hat{a}(\hat{z})| \ll g|\partial \hat{E}_z^f(\rho)/\partial\rho|/|\hat{E}_r^f(\rho)|$), which is satisfied for the device under consideration. So the system of equations to be solved are Eqs. (4.9), (4.10), (4.11) and (4.13), together with the field evolution Eq. (4.1), which

in dimensionless form can be written as,

$$\frac{\partial \hat{a}(\hat{z})}{\partial \hat{z}} = C \left\langle i \frac{\mathbf{S}}{S_z} \cdot \hat{\mathbf{E}}^*(r) e^{-i\psi} \right\rangle_{\text{beam},\, \psi_0} . \tag{4.14}$$

Here C is a dimensionless constant given by,

$$C = \frac{h^2}{\left|\hat{E}_{z1}(R_b)\right|^2} \frac{Z_{int} I}{mc^2/e}. \tag{4.15}$$

Note that the constant C depends only on the beam current, frequency, and the geometry of the slow wave structure (the helix loaded tube).

For the case of one dimensional motion of the annular beam where only axial interaction is taken into consideration, Eq. (4.14) can be simplified to,

$$\frac{\partial \hat{a}(\hat{z})}{\partial \hat{z}} \hat{E}_{z1}(R_b) = i \frac{h^2}{mc^2/e} Z_{int} I \left\langle e^{-i\psi} \right\rangle_{\psi_0} , \tag{4.16}$$

where $i(\omega/c)\hat{a}(\hat{z})\hat{E}_{z1}(R_b)$ is the axial electric field at the radius of the annular beam. Equation (4.16) multiplied by $i\omega/c$ gives the conventional one-dimensional interaction equation with $dE_z(z)/dz \propto Z_{int} I \left\langle e^{-i\psi} \right\rangle_{\psi_0}$.

4.3 Numerical Results and Discussion

Equations (4.9), (4.10), (4.11), (4.13) and (4.14) can be integrated for a certain initial amplitude $a(0)$, which corresponds to a certain power flow in the opposite direction at the beam entrance. Trajectories of electrons uniformly distributed over their entrance phase and the beam cross-section are computed. The electronic efficiency $\eta = (\gamma_0 - \langle\gamma\rangle)/(\gamma_0 - 1)$ as a function of the axial distance is calculated for the electrons, whose trajectories depend on their initial phases and their initial radial positions, where γ_0 is the electron initial relativistic factor and $\langle ... \rangle$ corresponds to averaging over initial entrance phase and beam cross-section.

The electronic efficiency is simply referred to as efficiency as it is the only efficiency considered in this study. The helix SWS parameters used are: helix radius $R_h = 2.5$ cm, tube radius $R_c = 5.0$ cm, pitch period $\lambda_h = 2.28$ cm. The electron beam is assumed to be a mono-energetic solid beam with radius R_b. The device is assumed to operate with a nominal beam voltage about 40 kV beam at frequency 1.26 GHz.

The calculated device electronic efficiency is shown in Fig. 4.1 as a function of the backward power, assumed a given value at the beam entrance, for different beam parameters[1]. The results show that the maximum electronic efficiency for the beam radius $R_b = 1.5$ cm is almost doubled compared to its value for $R_b = 2.8$ cm case, even though the beam current I_b is significantly reduced in the small radius case. This was verified in the University of Maryland experiment [37, 27, 26], where for a small beam radius of 1.5 cm and 40 kV electron beam, electronic efficiency over 50% was achieved. In each of the groups (a) or (b) in Fig. 4.1, it is assumed that the operating frequency remains constant with slight change of beam voltage V_b. This corresponds to experimental conditions, where due to the end reflections, the operating frequency was discretized instead of continuously varying with the beam voltage as in devices with well matched output [21].

The typical output power of this device is about 500 kW [21], and the experimentally measured Q-factor is about 400 [26]. Let us assume that the diffraction

[1]Only the power associated with the backward wave, which is the interacting wave, is considered. There is another amount of power associated with the no-interacting forward wave, where the net power flow is the difference between the two.

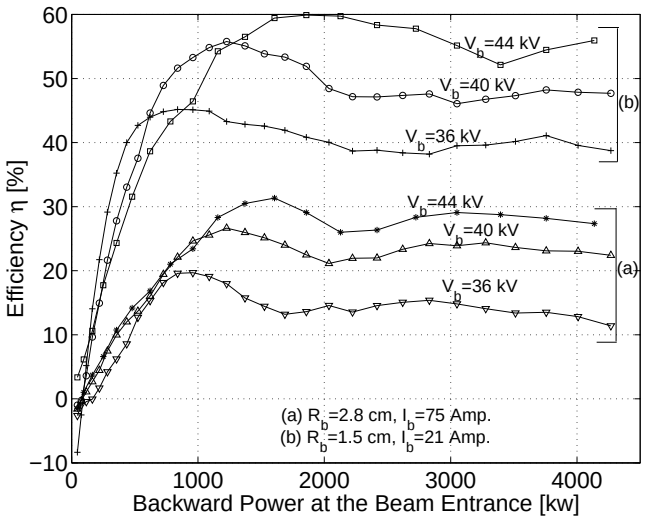

Figure 4.1: Efficiency versus RF backward power at the beam entrance for different beam parameters (Only the power associated with the backward wave, which is the interacting wave, is considered. There is another amount of power associated with the non-interacting forward wave, where the net power flow is the difference between the two). The SWS is a helix of radius $R_h = 2.5$ cm, loaded inside a circular waveguide of radius $R_c = 5$ cm. The helix period $\lambda_h = 2.28$ cm. The operating frequency is $f = 1.26$ GHz.

Q-factor can be estimated by a simple formula,

$$Q \approx \frac{\omega L}{v_{gr}(1-|R|)}, \tag{4.17}$$

where $|R|$ is the reflection coefficient (usually at one end all the power is reflected, with the other end reflection coefficient designated by $|R|$), v_{gr} is the group velocity for the given helix parameters, and L is the cavity total length. Then, using the measured value of Q (400), the known cavity length ($L \approx 40$ cm), and the calculated group velocity ($v_{gr} = 0.145c$), one estimates the reflection coefficient as $|R| \sim 0.818$. As the output power from the device P_{out} is related to the backward power inside the device P_{bp} through, $P_{out} = (1-|R|^2)P_{bp}$. So for 500 kW output power, the backward power level is about 1.5 MW. From Fig. 4.1, this backward power level corresponds to efficiency of 25% for the beam with 40 kV, 75 Amp., and initial radius $R_b = 2.8$ cm. The efficiency rises up to 55% for the beam with 40 kV, 21 Amp., and initial radius $R_b = 1.5$ cm. This increase in efficiency by reducing the initial beam radius was further explored. The radial trajectories, efficiency variation with the axial direction, and the polar plot of the radial distance with the particle phase were analyzed.

The radial trajectories for a large initial beam radius ($R_b = 2.8$ cm) are shown in Fig. 4.2. This figure shows the particle trajectories for different initial radial positions and different initial phases. Most of the particles are intercepted by the outer tube at about 22 cm, and the majority of remaining particles becomes trapped by the potential well formed around the helix by the radial electric field E_r (see Fig. 3.4). To see how the initial radial position inside and outside the helix affects the device efficiency, the efficiency variation with axial position Z is shown in Fig. 4.3 for electrons initially entering either inside or outside the helix. In Fig. 4.3, it is evident that particles which initially entered inside the

helix are those that contribute most to the total efficiency. This indicates that enhancement of the total efficiency can be accomplished if we inject an electron beam of a small radius inside the helix. The case of small radius electron beam ($R_b = 1.5$ cm) is shown in Figs. 4.4, 4.5. The trajectories of selected beamlets are shown in Fig. 4.4, one beamlet near the axis and another far away from the axis. Different rays within the beamlet correspond to different electron entrance phases. From that figure, we see that electrons immersed near the axis experience much smaller radial spread than those located far away from the axis. This corresponds to the small deviation of phases for electrons near the axis, which means that electrons immersed near the axis are much more coherently bunched than those far away from the axis.

To understand the bunching mechanism, a polar plot is shown in Fig. 4.6. Here, the radial coordinate corresponds to electron radial location in cm and the particle phase with respect to the wave is used as the polar angle. In this figure, it is shown that the bunching occurs between 1 and 2 cm of radial position (recall that at the entrance $R_b = 1.5$ cm) and at a phase $\psi \approx 3\pi/2$. This phase corresponds to maximum interaction with the axial electric field, and minimum interaction with the radial field [see Eq. (4.10)]. The formation of the bunch between 1 and 2 cm enables the electrons to be exposed to a significant field near the helix, which is at 2.5 cm. This explains the high efficiency of the device. A few particles experiencing radial oscillations are shown in Fig. 4.6 with banana trajectories around the π phase and the helix 2.5 cm radial position. These radial oscillations are due to potential well formed by the radial electric field.

The effective field amplitude seen in the PASOTRON by radially moving particles is very different from that of the conventional BWO where electrons

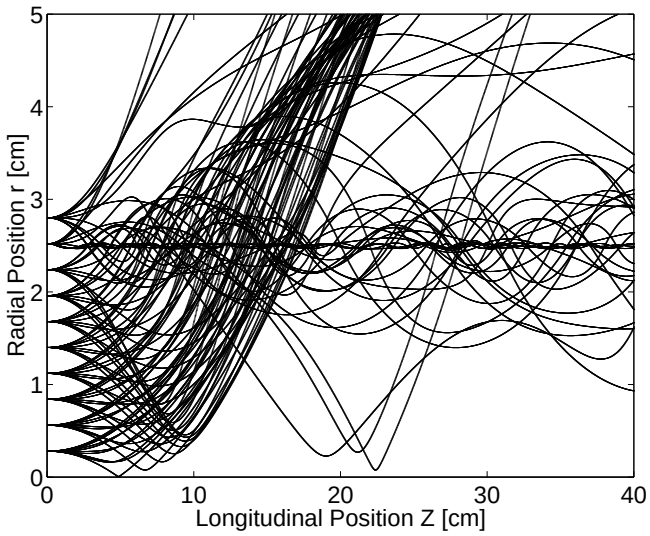

Figure 4.2: The radial trajectories for electrons with different entrance phases. The operating frequency is $f = 1.26$ GHz, beam current $I_b = 75$ Amp., beam voltage is 40 kV, and initial beam radius is 2.8 cm. The helix radius is $R_h = 2.5$ cm, and is loaded inside a circular waveguide of radius $R_c = 5$ cm. The helix period $\lambda_h = 2.28$ cm. The power in the backward direction at the electron beam entrance is assumed to be 1.5 MW.

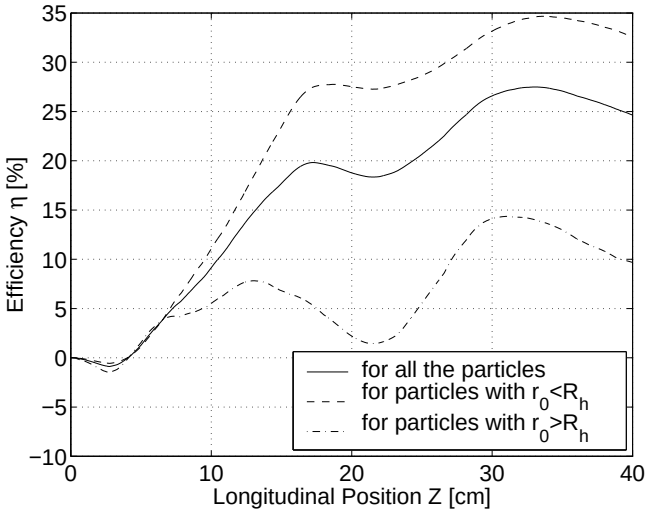

Figure 4.3: Electronic efficiency depends on electrons initial radial positions in the beam. Electrons inside the helix have higher efficiency than those outside the helix. Parameters are the same as Fig. 4.2.

propagate only axially. The normalized effective amplitude of the axial field seen by electrons injected very close to the axis is shown in Fig. 4.7. Here, different curves correspond to the field seen by electrons with different initial phases. So, in this case electrons are modulated near the entrance by a small amplitude field, while the stronger field near the helix provides energy extraction from these electron bunches. This is very different from the conventional BWO with only axial motion, where at the entrance the electrons are modulated by a large amplitude field while the energy is extracted from the bunches by a weak field which is, apparently, unfavorable for the interaction efficiency. (Note that a method of enhancing the efficiency of the conventional BWO, by increasing the beam coupling impedance to the wave near the output was analyzed in Ref. [40].)

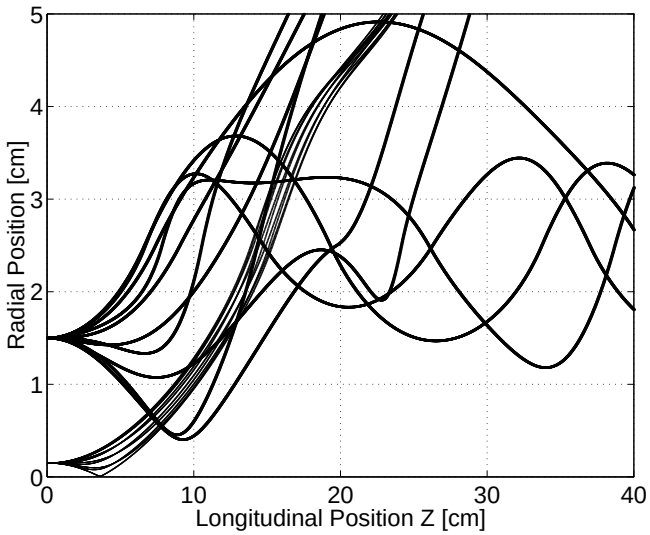

Figure 4.4: The radial trajectories of electrons with the different rays corresponding to different entrance phases for some selected beamlets. The operating frequency is $f = 1.26$ GHz, beam current $I_b = 21$ Amp., beam voltage is 40 kV, and initial beam radius is 1.5 cm. The power in the backward direction at the beam entrance is about 1.5 MW. An electron beamlet entering close to the axis experiences smaller radial spread than a beamlet entering away from the axis.

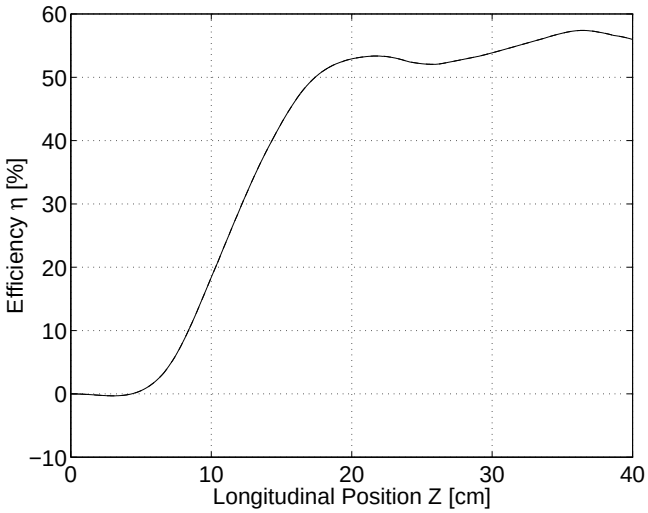

Figure 4.5: Electronic efficiency for a beam with a small initial radius ($R_b = 1.5$ cm). Parameters are the same as in Fig. 4.4.

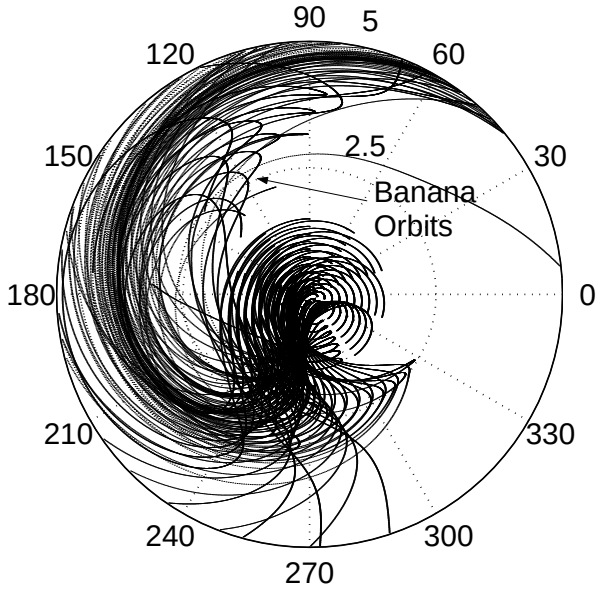

Figure 4.6: Polar drawing of the particle radial distance as the radius in cm, and the particle phase ψ as the polar angle. Parameters are the same as in Fig. 4.4.

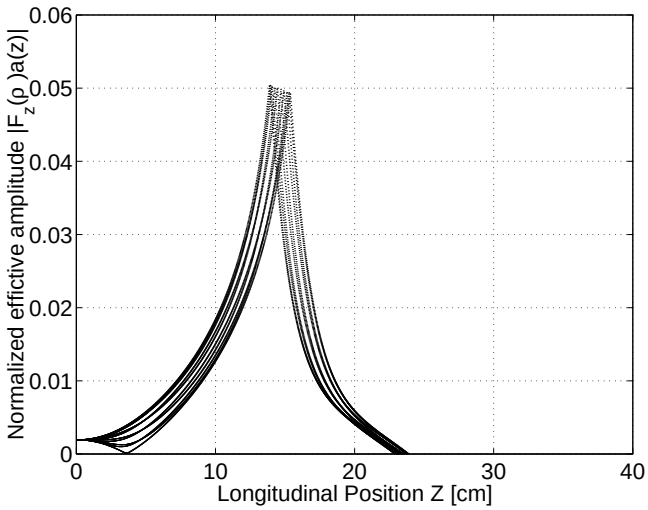

Figure 4.7: Normalized effective amplitude seen by particles initially injected close to the helix axis. Parameters are the same as in Fig. 4.4.

4.4 Conclusion

We developed a 3D model which describes the operation of the helix PASOTRON BWO. Using this model enabled us to understand the operation of the device, in which the transverse motion plays a major role in the efficiency enhancement. This transverse motion allows electrons to move from initial near-axis location, where the RF field is small, to the large field around the helix. Bunched at the proper phase, these electrons interact strongly with a large amplitude field and give up most of their kinetic energy to the field. This explains the higher efficiency of this device, compared with its linear beam counterparts.

The efficiency of the electrons initially injected inside the helix was compared to those initially injected outside. Electrons injected inside the helix were shown to be more efficient in exciting electromagnetic waves than those injected outside. It was shown that the reduction of the beam radius from its original value of

2.8 cm at 75 Amp to 1.5 cm at 21 Amp with a 40 kV electron beam allows one to increase the electronics efficiency from 25% to be more than 55%. These result was recently verified experimentally [41, 37, 27, 26], with the same typical parameters.

Chapter 5

Time Dependent Model for the Helix PASOTRON BWO

5.1 Introduction

In chapter 4, the steady state operation of the helix PASOTRON BWO was studied in details. In that study, single frequency stationary operation of the device was assumed. However, that assumption is not always satisfied. Very often, at high currents and/or strong end reflections the device exhibits auto-modulation, where two or more modes are excited simultaneously. The conditions for the existence of auto-modulation and the regions of stable (single mode) operation are studied in this chapter through a time dependent model of the device. Throughout the discussion, we always compare the results of the one dimensional (1D) case with the three dimensional (3D) case. The 1D case refers to the model when a longitudinal motion is the only degree of freedom allowed like in the conventional BWO, where electrons propagate in a strong focusing magnetic field. In the 3D case electron transverse motion is considered as well. This is the case of the actual helix PASOTRON BWO device, where focusing magnetic field is

absent. In this way, we can explore how the 3D motion can affect the temporal behavior of the helix PASOTRON BWO.

This chapter is organized as follows: The equations of motion, and the envelope equation are presented in sections 5.2 and 5.3, respectively. The starting oscillations parameters are discussed in section 5.5. The results and their discussion are presented in section 5.6 in two subsections; one for the zero reflection boundary conditions, and the other for the non-zero reflection case. Finally, the conclusions are presented in section 5.7.

5.2 Equations of Motion

In the previous chapter, we used cylindrical coordinates to formulate the model of the BWO tube, because of the cylindrical geometry of the problem. However, for that coordinate system, Lorentz equations of motion exhibit singularity for particles passing close to the axis. To treat this problem when using this coordinate system, the integration step was made very small, and the number of beamlets in the radial distribution was changed to avoid those particles approaching the axis. This technique was employed for the steady operation for a specific field at the entrance. However, for the time varying case, it is hard to avoid particles hitting or approaching the axis, and we have to eliminate those "bad" particles from the simulation, which introduces a small error in the results. A good solution to this problem is to use new transverse coordinates, which can be called complex coordinates $(x+iy)$. This allows us to preserve the cylindrical nature of the problem while avoiding the axis singularity at the same time. The equations of motion in these coordinates are formulated below.

The Lorentz equations of motion in cartesian coordinates are given as,

$$\frac{d}{dt}(\gamma m\dot{x}) = q\left(\mathcal{E}_x + \dot{y}\mathcal{B}_z/c - \dot{z}\mathcal{B}_y/c\right), \tag{5.1a}$$

$$\frac{d}{dt}(\gamma m\dot{y}) = q\left(\mathcal{E}_y + \dot{z}\mathcal{B}_x/c - \dot{x}\mathcal{B}_z/c\right), \tag{5.1b}$$

$$\frac{d}{dt}(\gamma m\dot{z}) = q\left(\mathcal{E}_z + \dot{x}\mathcal{B}_y/c - \dot{y}\mathcal{B}_x/c\right), \tag{5.1c}$$

where $\mathcal{E}_x$, $\mathcal{E}_y$, $\mathcal{E}_z$ and $\mathcal{B}_x$, $\mathcal{B}_y$, $\mathcal{B}_z$ are the components of the instantaneous electric and magnetic fields, respectively. The energy evolution equation in rectangular coordinates can also be written as,

$$\frac{d}{dt}\gamma = \frac{q}{mc^2}\left(\dot{x}\mathcal{E}_x + \dot{y}\mathcal{E}_y + \dot{z}\mathcal{E}_z\right). \tag{5.2}$$

The transformation of vector components from cartesian coordinates to cylindrical ones depends on vector position in the $x-y$ plane. For a vector $\mathbf{A}$ with polar position (r,θ), this transformation is given by,

$$A_x = A_r\cos\theta - A_\theta\sin\theta,$$

$$A_y = A_r\sin\theta + A_\theta\cos\theta,$$

Correspondingly, one can introduce complex combinations,

$$A_x + iA_y = (A_r + iA_\theta)\,e^{i\theta}, \qquad A_x - iA_y = (A_r - iA_\theta)\,e^{-i\theta}, \tag{5.3}$$

which will be used later on. Introducing the new variable $\xi_1 = x + iy$, we can combine Eqs. (5.1a, 5.1b) in terms of this new complex variable, by adding Eq. (5.1a) and Eq. (5.1b) multiplied by i. Equations (5.1c) and (5.2) can also be written in terms of the complex variable ξ_1;

$$\frac{d}{dt}(\gamma m\dot{\xi}_1) = q\left[(\mathcal{E}_r + i\mathcal{E}_\theta)\,e^{i\theta} - i(\dot{\xi}_1/c)\mathcal{B}_z + i(\dot{z}/c)\,(\mathcal{B}_r + i\mathcal{B}_\theta)\,e^{i\theta}\right], \tag{5.4}$$

$$\frac{d}{dt}(\gamma m\dot{z}) = q\left(\mathcal{E}_z - Im\{(\dot{\xi}_1/c)\,(\mathcal{B}_r - i\mathcal{B}_\theta)\,e^{-i\theta}\}\right), \tag{5.5}$$

$$\frac{d}{dt}\gamma = \frac{q}{mc^2}\left[Re\left\{\dot{\xi}_1\,(\mathcal{E}_r - i\mathcal{E}_\theta)\,e^{-i\theta}\right\} + \dot{z}\mathcal{E}_z\right], \tag{5.6}$$

where in obtaining Eqs. (5.4), (5.5) and (5.6), we used Eqs. (5.3).

Now we represent the above equations as derivatives of z instead of t, since the boundary conditions are given in terms of z (i.e. at $z = 0$ and $z = L$, where L is the device length). The variable ξ_1 can be represented as $\xi_1 = re^{i\theta}$. For particle angular position θ_0 at the entrance (at $z = 0$), we define $\xi = \xi_1 e^{-i\theta_0} = re^{i\Delta\theta}$, where $\Delta\theta = \theta - \theta_0$. Thus, all particles have the same initial condition $\Delta\theta = 0$ at $z = 0$, independent of their initial azimuthal positions θ_0. (Later on, the initial particle azimuthal angular position will be shown to be absorbed in the particle phase definition.) So in terms of ξ the above equations can be written as,

$$\frac{d}{dz}(\gamma m\dot{\xi}) = \frac{q}{\dot{z}}\left[(\mathcal{E}_r + i\mathcal{E}_\theta)\, e^{i\Delta\theta} - i\frac{\dot{\xi}}{c}\mathcal{B}_z + i\frac{\dot{z}}{c}\,(\mathcal{B}_r + i\mathcal{B}_\theta)\, e^{i\Delta\theta}\right], \tag{5.7}$$

$$\frac{d}{dz}(\gamma m\dot{z}) = \frac{q}{\dot{z}}\left[\mathcal{E}_z - Im\{\frac{\dot{\xi}}{c}\,(\mathcal{B}_r - i\mathcal{B}_\theta)\, e^{-i\Delta\theta}\}\right], \tag{5.8}$$

$$\frac{d}{dz}\gamma = \frac{q}{mc^2\dot{z}}\left[Re\left\{\dot{\xi}\,(\mathcal{E}_r - i\mathcal{E}_\theta)\, e^{-i\Delta\theta}\right\} + \dot{z}\mathcal{E}_z\right]. \tag{5.9}$$

The above equations are solved for transverse initial conditions, $\xi|_{z=0} = r_0,\ \Delta\theta|_{z=0} = \arg\xi|_{z=0} = 0,\ \dot{\xi}|_{z=0} = 0$. The complex variable ξ has a magnitude equal to the particle radial position r, and phase equal to the particle rotation angle relative to its initial polar angle at the entrance. The last boundary condition ($\dot{\xi}|_{z=0} = 0$) implies an initially linear electron beam.

The fields of the harmonic interacting with the electron beam have the phasor representation given in section 3.4 and Appendix B. For convenience we write this representation again,

$$\hat{\mathbf{E}} = -i\hat{E}_r^f\mathbf{e}_r + \hat{E}_\theta^f\mathbf{e}_\theta + \hat{E}_z^f\mathbf{e}_z,$$

$$\hat{\mathbf{B}} = \hat{B}_r^f\mathbf{e}_r - i\hat{B}_\theta^f\mathbf{e}_\theta - i\hat{B}_z^f\mathbf{e}_z,$$

The instantaneous fields of this synchronous harmonic are given as,

$$\boldsymbol{\mathcal{E}} = Re\{\epsilon(z,t)\hat{\mathbf{E}}(r)e^{i(kz-\omega t-\theta)}\}, \text{ and } \boldsymbol{\mathcal{B}} = Re\{\epsilon(z,t)\hat{\mathbf{B}}(r)e^{i(kz-\omega t-\theta)}\},$$

where the function $\epsilon(z,t)$ describes the wave envelope as a function of longitudinal distance z and time t. Defining $\psi = kz - \omega t - \theta_0$, the fields can be written as $\boldsymbol{\mathcal{E}} = Re\{\epsilon(z,t)\hat{\mathbf{E}}(r)e^{i(\psi-\Delta\theta)}\}$ and $\boldsymbol{\mathcal{B}} = Re\{\epsilon(z,t)\hat{\mathbf{B}}(r)e^{i(\psi-\Delta\theta)}\}$. When we use the following normalizations: $\hat{\xi} = \kappa\xi$, $\hat{z} = z/L$, $\hat{p}_\xi = \gamma\dot{\xi}/c$, $\hat{\epsilon} = eL\epsilon/mc^2$, $\bar{k} = kL$, $\bar{\kappa} = \kappa L$, $\bar{\omega} = \omega L/c$ (where L is the device length), the equations of motion become,

$$\begin{aligned}\frac{d}{d\hat{z}}\hat{p}_\xi = -\Big[&\left(E_r^f/\beta_z - B_\theta^f\right) Im\{\hat{\epsilon}(z,t)e^{i(\psi-\Delta\theta)}\}e^{i\Delta\theta} \\ &+i\left(E_\theta^f/\beta_z + B_r^f\right) Re\{\epsilon(z,t)e^{i(\psi-\Delta\theta)}\}e^{i\Delta\theta} - i\frac{\hat{p}_\xi}{\gamma\beta_z}B_z^f Im\{\hat{\epsilon}(z,t)e^{i(\psi-\Delta\theta)}\Big],\end{aligned} \tag{5.10}$$

$$\begin{aligned}\frac{d}{d\hat{z}}\gamma = -Re\left\{\hat{p}_\xi\left(E_r^f Im\left\{\hat{\epsilon}(z,t)e^{i(\psi-\Delta\theta)}\right\} - iE_\theta^f Re\left\{\hat{\epsilon}(z,t)e^{i(\psi-\Delta\theta)}\right\}\right)e^{-i\Delta\theta}\right\} \\ /\gamma\beta_z - E_z^f Re\left\{\hat{\epsilon}(z,t)e^{i(\psi-\Delta\theta)}\right\},\end{aligned} \tag{5.11}$$

$$\frac{d}{d\hat{z}}\hat{\xi} = \frac{\bar{\kappa}\hat{p}_\xi}{\gamma\beta_z}, \tag{5.12}$$

$$\frac{d}{d\bar{z}}\psi = \bar{k} - \bar{\omega}/\beta_z, \tag{5.13}$$

$$\beta_z = \sqrt{1-\left(1+|\hat{p}_\xi|^2\right)/\gamma^2},$$

where E_r^f, E_θ^f, E_z^f, B_r^f, B_θ^f, and B_z^f are real functions of the normalized radial positions $\rho = \kappa r = |\hat{\xi}|$; see section 3.4 and Appendix B. In this model, we consider particles to be initially distributed over $\rho_0 = \xi_0$, and ψ_0, such that we have constant current density across the beam and uniform phase distribution over ψ_0. We absorbed the particle angular position at the entrance in the ψ definition.

This way, we consider only radial and ψ-phase distribution of particles without considering their angular distribution (distribution with θ_0), which significantly reduces the number of particles encountered in the simulation.

5.3 Wave Envelope Equation

Similar to the equations of motion, the wave envelope equation for the BWO can be written in terms of the new complex coordinates as,

$$\frac{\partial\hat{\epsilon}(\bar{z},\tau)}{\partial\tau} - \frac{\partial\hat{\epsilon}(\bar{z},\tau)}{\partial\bar{z}} = C\left\langle\left[i\left(\hat{p}_\xi(\hat{E}_r^f - \hat{E}_\theta^f) + \hat{p}_\xi^*(\hat{E}_r^f + \hat{E}_\theta^f)e^{i2\Delta\theta}\right)/2\gamma\beta_z + E_z^f e^{i\Delta\theta}\right]e^{-i\psi}\right\rangle. \quad (5.14)$$

where τ is the normalized time ($\tau = tv_g/L$), and the constant C is given by

$$C = \frac{\bar{k}^2 Z_{int} I_b/(mc^2/e)}{|\hat{E}_z(R_b)|^2}.$$

The variable Z_{int} is the interaction impedance calculated by using the code CHRISTINE [32], I_b is the beam current injected, and $|\hat{E}_z(R_b)|$ is the normalized axial electric field amplitude of the first spatial harmonic evaluated at $r = R_b$.

The forward wave is assumed to be non interacting with the electron beam synchronously, so the forward wave envelope equation is,

$$\frac{\partial\hat{\epsilon}_f(\bar{z},\tau)}{\partial\tau} + \frac{\partial\hat{\epsilon}_f(\bar{z},\tau)}{\partial\bar{z}} = 0. \quad (5.15)$$

The reflection of the backward wave occurs at $z = 0$ to give the forward wave, which in turn reflects at the device end $z = L$. The boundary conditions at these both ends can be combined [31] as,

$$\hat{\epsilon}_f|_{z=0} = -\hat{\epsilon}|_{z=0}, \qquad \hat{\epsilon}_{z=L} = -Re^{-2ikL}\hat{\epsilon}_f|_{z=L},$$

where $R = R_1 R_2$, R_1 and R_2 are the reflection coefficient at $z = 0$ and $z = L$, respectively. Thus, we reduce the number of parameters to characterize the device to one R, instead of two.

5.4 PASOTRON BWO Model

The time dependent model of the PASOTRON BWO is based on integration of the equations of motions Eqs. (5.10), (5.11), (5.12), and (5.13); and the wave equations Eqs. (5.14), and (5.15) over a grid in $\tau - \hat{z}$ plane. In solving these equations we assume that a particle experiences a stationary field during its lifetime inside the device. Thus, the time variation of $\hat{\epsilon}(\hat{z}, \tau)$ is neglected during the particle motion inside the tube. This assumption can be formulated as,

$$\left| \frac{\partial \epsilon(z,t)}{\partial t} / \epsilon(z,t) \right| \ll T^{-1},$$

where $T \approx L/v_{z0}$ is the time a particle, which entered with initial velocity v_{z0}, spends inside the device before exiting at $z = L$ (For 3D motion, particles may be intercepted by the helix outer tube. This makes the travel distance of the particle smaller than L.). Using this assumption, the wave envelop profile $\epsilon(\hat{z}, \tau)$ at time instant τ is used in integrating the equations of motion, where particles' positions and momenta are obtained over the grid axial points, all at the same time τ. These particles' positions and momenta in their turn are used to get the source term in the envelope equation, where this equation together with the equation for the forward wave and the boundary conditions are used to calculate the fields at the next time step $\tau + \Delta\tau$. This assumption imposes limitations on the validity of the results. Only results with single frequency output or non stationary shallow level modulation can be considered as valid.

The model should have some means to calculate the frequency of operation. The device frequency is made dynamically changing, with the initial frequency corresponding to the resonance intersection of the beam line, $\omega = kv_{z0}$, with the backward wave dispersion line. (Of course, this dynamic has a temporal scale much larger than the wave period $2\pi/\omega$.) The model given by the equations of motion together with the envelope equation is invariant to the shift of frequency [31], by $\Delta\omega$, which corresponds to shift of axial wavenumber by $\Delta k = \Delta\omega/v_g = -\Delta\omega/|v_g|$. So, we define the new phase variable as $\psi' = \psi + \Delta kz - \Delta\omega t$, where the new frequency and axial wavenumbers are, respectively, given by $\omega' = \omega + \Delta\omega$ and $k' = k + \Delta k$. Also, the new envelopes become $\hat{\epsilon}' = \hat{\epsilon}e^{i(\Delta\omega t - \Delta kz)}$ and $\hat{\epsilon}'_f = \hat{\epsilon}_f e^{i(\Delta\omega t + \Delta kz)}$. Thus, new equations are the same after replacing ω, k, ψ, $\hat{\epsilon}$, and $\hat{\epsilon}_f$ by ω', k', ψ', $\hat{\epsilon}'$, and $\hat{\epsilon}'_f$, respectively. The frequency shift at each time step is obtained from the time variation of the forward wave envelop $\epsilon_f(z,t)$, assuming $\epsilon_f(z,t) = |\epsilon_f(z,t)|\, e^{i\phi(z,t)}$. Then, the frequency shift $\Delta\omega$ can be determined as [31],

$$\Delta\omega = -\int |\epsilon_f(z,t)|^2 \, Re\{\frac{\partial\phi}{\partial t}\}dz / \int |\epsilon_f(z,t)|^2 \, dz.$$

Here, accounting for the forward envelope Eq. (5.15), one can write,

$$\begin{aligned}\int |\epsilon_f(z,t)|^2 \, Re\{\frac{\partial\phi}{\partial t}\}dz &= \int Im\{\epsilon_f^*(z,t)\frac{\partial\epsilon_f(z,t)}{\partial t}\}dz \\ &= -|v_g| \int Im\{\epsilon_f^*(z,t)\frac{\partial\epsilon_f(z,t)}{\partial z}\}dz\end{aligned}$$

where we used Eq. (5.15). So the frequency shift can be given by,

$$\Delta\omega = |v_g| \int Im\{\epsilon_f^*(z,t)\frac{\partial\epsilon_f(z,t)}{\partial z}\}dz / \int |\epsilon_f(z,t)|^2 \, dz$$

5.5 Starting Oscillation Parameters

One of the important quantities for BWO characterization is the starting oscillation current. This is the minimum current required to begin oscillation. The starting oscillation current and frequency for BWO with end reflections was calculated by Johnson [30] using Pierce circuit model. The results were presented in terms of device normalized length. The same starting oscillation current was obtained using the RF field approach in Refs. [42] and [31], for zero and non-zero reflections, respectively. Another numerical method was proposed in Ref. [43] to calculate the starting current.

In all these calculations, it is assumed that the device starts to oscillate at a single frequency. We will use the same approach presented in Ref. [42] to calculate the starting current for the 1D BWO with end reflections. That method becomes so complicated when we try to apply for the 3D case. So the starting current for the PASOTRON BWO is calculated using the approach presented in Ref. [43].

5.5.1 One Dimensional BWO

The starting current for 1D BWO can be obtained by solving the linearized equations of motion together with the wave envelope equation [42]. The linearization is made in terms of the variables $\tilde{\psi}$, $\tilde{\gamma}$ and F, defined by,

$$\psi = \psi_0 + \Delta\bar{z} + \tilde{\psi}, \quad \gamma = \gamma_0 + \tilde{\gamma}, \quad F = \hat{\epsilon}e^{i\Delta z},$$

where $\Delta = \bar{k} - \bar{\omega}/\beta_{z0}$, and the '0' subscript represents the quantity at the entrance to the BWO. So in linearized equations in terms of these new variables

are,

$$\frac{d\tilde{\psi}}{d\bar{z}} = \frac{\bar{\omega}\tilde{\gamma}}{\gamma_0^3\beta_{z0}^3}, \tag{5.16a}$$

$$\frac{d\tilde{\gamma}}{d\bar{z}} = -E_z^f(\kappa r_0)Re\{Fe^{i\psi_0}\} \tag{5.16b}$$

$$i\Delta F - \frac{dF}{d\bar{z}} = -iC\left\langle E_z^f(\kappa r_0)\tilde{\psi}e^{-i\psi_0}\right\rangle. \tag{5.16c}$$

Now, we write the two equations of motions Eqs. (5.16a), and (5.16b) in terms of averaged variables $\tilde{\psi}_{av}$ and $\tilde{\gamma}_{av}$, where the averaging is over the entrance phase ψ_0 and entrance radius r_0. These averages are given by,

$$\tilde{\psi}_{av} = \left\langle \tilde{\psi}E_z^f(\kappa r_0)e^{i\psi_0}\right\rangle, \qquad \tilde{\gamma}_{av} = \left\langle \tilde{\gamma}E_z^f(\kappa r_0)e^{i\psi_0}\right\rangle.$$

So the linearized equations in terms of these averaged variables are given by,

$$\frac{d\tilde{\psi}_{av}}{d\bar{z}} = \frac{\bar{\omega}\tilde{\gamma}_{av}}{\gamma_0^3\beta_{z0}^3}, \tag{5.17a}$$

$$\frac{d\tilde{\gamma}_{av}}{d\bar{z}} = -F\int_0^{rb}[E_z^f(\kappa r_0)]^2 r_0 dr_0/r_{b^2}, \tag{5.17b}$$

$$i\Delta F - \frac{dF}{d\bar{z}} = -iC\tilde{\psi}_{av} \tag{5.17c}$$

These equation can be simplified (to the minimum number of parameters) [42], using the following new variable X, Y, and Z, defined by,

$$Z = D\bar{z}, \quad X = \frac{\bar{\omega}}{\gamma_0^3\beta_0^3 D}\tilde{\gamma}_{av}, \quad Y = (D/C)F,$$

Where D is the normalized device length, which is given by,

$$D = \left(\frac{\bar{\omega}C}{\gamma_0^3\beta_0^3}\int_0^{rb}[E_z^f(\kappa r_0)]^2 r_0 dr_0/r_{b^2}\right)^{1/3}.$$

In term of the new variables, Eqs. (5.17) become,

$$\frac{d\tilde{\psi}_{av}}{dZ} = X, \tag{5.18a}$$

$$\frac{dX}{d\bar{z}} = -Y, \tag{5.18b}$$

$$i\Delta' Y - \frac{dY}{dZ} = -i\tilde{\psi}_{av}, \quad \text{where, } \Delta' = \Delta/D. \tag{5.18c}$$

These equations are linear homogeneous system of differential equations, which has the characteristic polynomial,

$$\lambda^2(i\Delta' - \lambda) = i.$$

For each value of Δ' there are three solutions, λ_1, λ_2, and λ_3, for that polynomial. Thus the solutions for these differential equations are,

$$\tilde{\psi}_{av} = \alpha_1 e^{\lambda_1 Z} + \alpha_2 e^{\lambda_2 Z} + \alpha_3 e^{\lambda_3 Z}, \tag{5.19a}$$

$$X = \alpha_1\lambda_1 e^{\lambda_1 Z} + \alpha_2\lambda_2 e^{\lambda_2 Z} + \alpha_3\lambda_3 e^{\lambda_3 Z}, \tag{5.19b}$$

$$Y = -\alpha_1\lambda_1^2 e^{\lambda_1 Z} - \alpha_2\lambda_2^2 e^{\lambda_2 Z} - \alpha_3\lambda_3^2 e^{\lambda_3 Z}. \tag{5.19c}$$

This solution should also satisfy the boundary conditions:

$$\tilde{\psi}_{av}|_{Z=0} = 0, \quad X|_{Z=0} = 0, \quad Y(D) = Re^{-2i\bar{k}+i\Delta}Y(0). \tag{5.20}$$

Solving Eqs (5.19, 5.20) for α_1, α_2 and α_3, we get the different modes for the linearized BWO. There are specific values for variable pair Δ' and D, for which there exist a non trivial solution of these equations. The mode with lowest possible $D \propto I^{1/3}$, represent the starting oscillation variable D_{st}, and the corresponding current and frequency are the starting oscillation parameters of the device. For zero reflection case, these equations are simply those described in Ref. [42], which gives $D_{st} = 1.974$.

We used this linear model to calculate the starting oscillation current and frequency for the non-zero reflection case. As we are interested in studying the

effect of changing the reflection phase on the operation of the BWO, we plot the calculated staring oscillation current and frequency versus the reflection phase in Fig. 5.1. The starting current curves is used to bound the region of oscillation of the BWO in Fig. 5.9(a), where obtaining this information from solving the nonlinear device equations is impractical as it requires long simulation time as the current is reduced.

5.5.2 Three Dimensional BWO (helix PASOTRON BWO)

Linearizing the equations for the 3D BWO to get the starting oscillation parameters is very complicated. A simple way, based on solving the nonlinear device equations was presented in Ref. [43]. That method is based on computing the growth envelope growth rates δ_1 and δ_2, for two small currents, I_1 and I_2, respectively. The starting current I_{st} is determined through the relation [43],

$$I_{st} = \frac{(\delta_1/\delta_2)I_2 - I_1}{\delta_1/\delta_2 - 1}. \tag{5.21}$$

So, numerically solving equations of motion Eqs. (5.10), (5.11), (5.12), and (5.11); and the envelope equations Eqs. (5.14) and (5.15) together with the boundary conditions, we get the temporal exponential growth of envelope before saturation. This growth rates is calculated for two different small currents, and the starting oscillation current is computed using Eq. (5.21). This starting current is plotted as the thick boundary boundary in Fig. 5.9(b). This method was applied only in the regions of reflection phase where the oscillations starts with a single frequency and saturates at a stationary single frequency waveform. For some regions of the reflection phases, there was no single frequency output; the device exhibits automodulation when it starts to oscillate. So, it was not

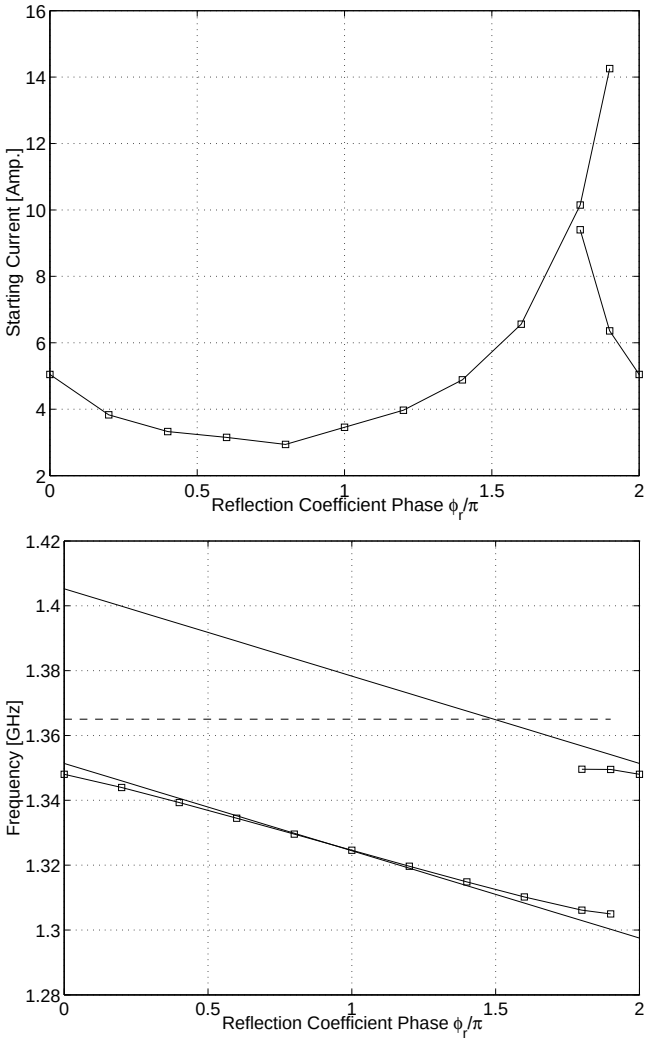

Figure 5.1: Starting oscillation current and frequency for the first two modes for 1D BWO. The BWO beam parameters used are 40 keV beam energy and 1.5 cm radius. The SWS is the helix loaded circular waveguide with $R_h = 2.5$ cm, $\lambda_h = 2.28$ cm, and $R_c = 5$ cm.

possible to apply that method for some ranges of reflection phase, see Fig. 5.9(b).

5.6 Numerical Results

The results obtained in this section were calculated for the typical beam parameters used in the University of Maryland PASOTRON BWO experiment [27]. The electron beam is assumed to be solid with uniform current density and 1.5 cm initial beam radius. The beam energy is 40 keV. The SWS helix parameters are as follows. The helix radius is 2.5 cm and is loaded inside a conducting cylinder of radius 5 cm. The helix pitch period is 2.28 cm.

The study is made for two kinds of boundary conditions. The first boundary condition is the zero reflection coefficient, with no feedback loop between the forward and backward waves. So, the only feedback loop is formed by the electron moving forward and the wave propagating backward. The second boundary condition is the strong reflection case $|R| = 0.80$, where the excitation of cavity resonant modes should be the dominant effect. The reflection coefficient magnitude for the latter case corresponds approximately to the measured cold cavity quality factor of 400 [27, 26]; see section 4.3 and Eq. (4.17).

5.6.1 Zero Reflection Coefficient

Zero reflection coefficient cuts the feedback loop between the forward and the backward waves in the BWO. However, there is an internal loop formed by the electron beam and the backward wave [2]. The typical device behavior for this case is shown in Figs. 5.2 for the 1D case and in Figs. 5.3 for the 3D case. In both cases, the device reaches a steady stationary state with single frequency

output. The transverse motion in the 3D case results in a higher efficiency (about 24.5%) compared to 10.28% for the 1D case.

Device stationary output depends on the beam current. The efficiency and frequency dependences on the beam current are shown in Figs. 5.4 and 5.5 for the 1D and 3D cases, respectively. For the 1D case, auto-modulation occurs when current exceeds 80 amps, while the start current is about 14 amps. This current (80 amp) approximately corresponds to the maximum achievable efficiency which is about 11%, see Figs. 5.4. As is shown in Fig. 5.5, device efficiency is higher (up to more than 30%)in the 3D case. Here, auto-modulation is not observed even at very large currents. The disappearance of auto-modulation can be attributed to electron interception by the device outer conducting tube. The electron interception reduces the effective length over which electrons interact with the wave. That effective length gets shorter as the injected beam current is increased. Thus, auto-modulation is avoided at larger currents. Shortening of the electron effective length with the increase in the beam current is shown in Fig. 5.6, where it is shown that for 120 Amp. current the electron beam is intercepted after shorter travel distance than the 40 Amp. beam current case.

The occurrence of auto-modulation in a 1D model of the BWO without reflection is due to electrons over-bunching in the strong field, i.e. the amplitude nonlinearity of the system was studied in for the 1D case without reflection by Ginzburg [42]. This mechanism is called the amplitude mechanism [44]. For a 3D BWO, when electrons give their energy to the wave, they become bunched 90° out of phase with the interacting longitudinal field. So the radial field which is 90° out of phase with the longitudinal electric field, pulls these electrons towards the outer conducting tube, as discussed in section 4.3. Thus, electron

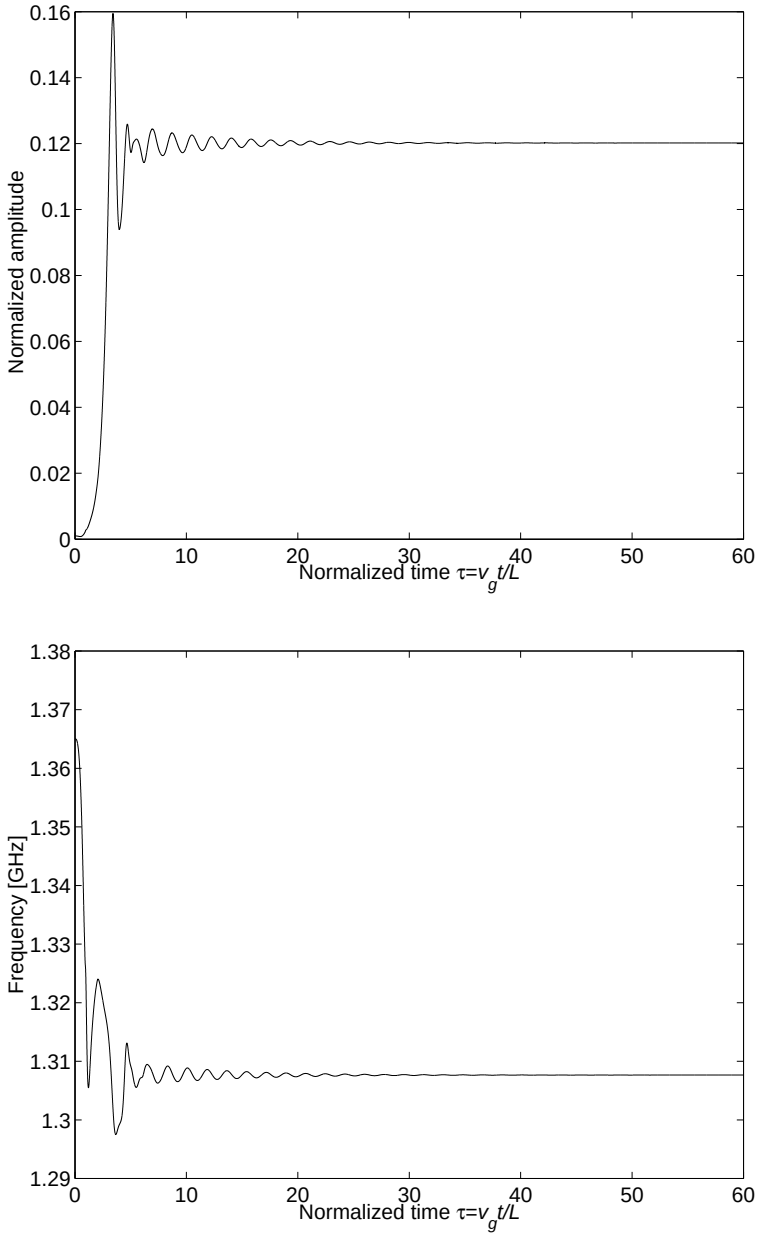

Figure 5.2: Normalized amplitude $|\hat{\epsilon}|$ and frequency versus the normalized time for 1D interaction. The beam radius is 1.5 cm, beam voltage is 40 kV, and current is 40 Amps.

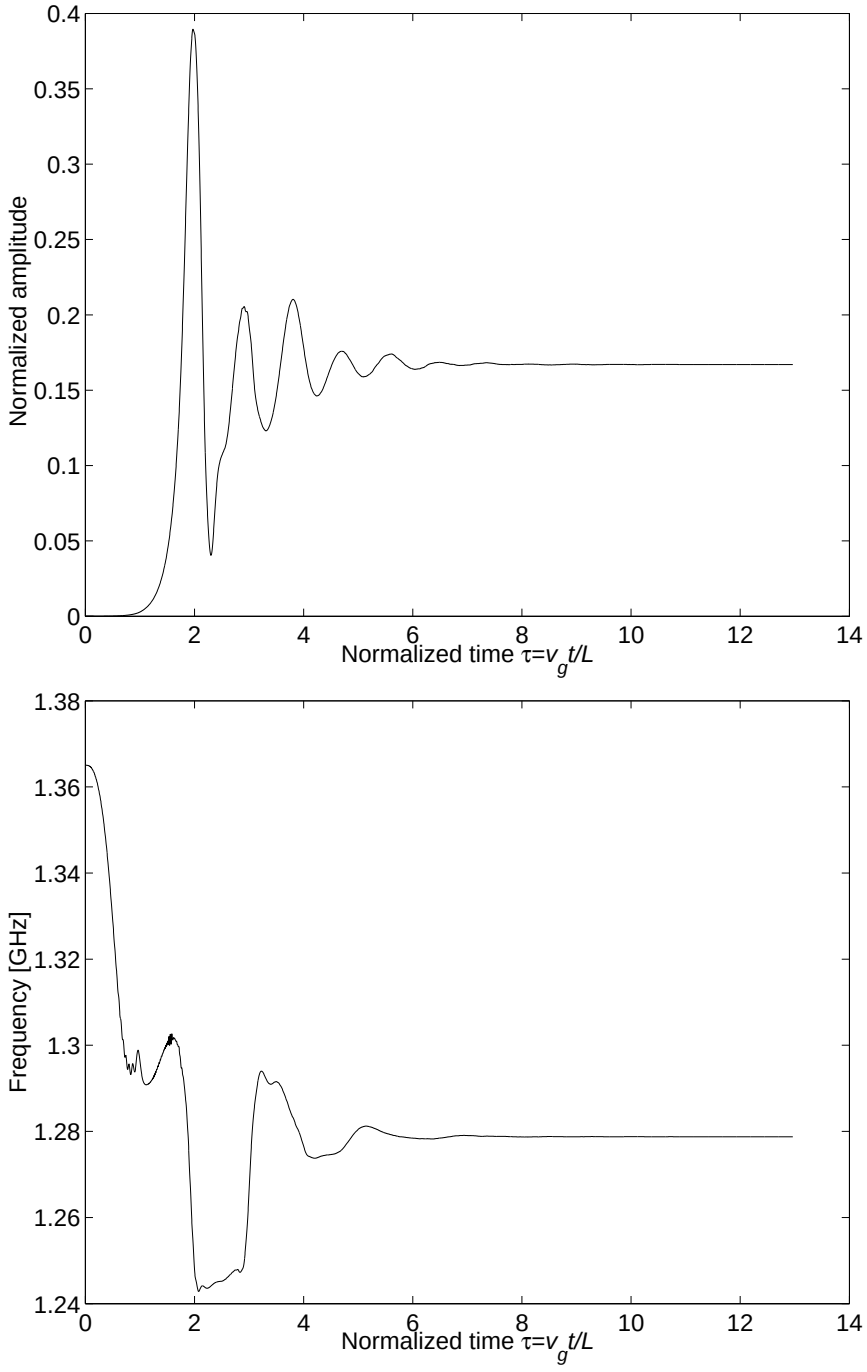

Figure 5.3: Normalized amplitude $|\hat{\epsilon}|$ and frequency versus the normalized time for 3D interaction. The beam radius is 1.5 cm, beam voltage is 40 kV, and current is 40 Amps.

bunches are intercepted by the outer tube without performing oscillations. This explains the disappearance of auto-modulation in an over-bunching regime in the 3D BWO.

5.6.2 Non-zero reflection

Non-zero reflection coefficient provides a closed loop feedback between the forward and the backward wave, which forms an electromagnetic cavity. It is not easy to determine exactly the reflection coefficient in BWO devices. However, the amplitude of the reflection coefficient can be estimated from the experimentally measured cavity quality factor; see Eq. 4.17. For the helix PASOTRON BWO the reflection coefficient amplitude was estimated to be 0.8 [27, 26].

In the case of non-zero reflections the stationary output of the device becomes sensitive to the phase of the reflection coefficient. The effect of the phase of the reflection coefficient is shown in Figs 5.7 and 5.8, for 1D and 3D cases, respectively. The beam current used in these two figures is 10 Amps. For the 1D device, the maximum efficiency is 17.4% for $|R| = 0.8$ compared with no oscillation for the zero reflection coefficient case; see Fig. 5.4 where the starting oscillation current is around 15 Amps. As is shown in Fig. 5.7a, the device output frequency closely follows the cold closed cavity resonance frequency shown by dashed lines. There is an empty region in Fig. 5.7 between $\phi_r = 0.1\pi$ and 0.5π, which corresponds to the non-stationary operation of the device. The phase $\phi_r = 0.1$ corresponds to total wave round trip inside the cavity with total phase change $\phi_r - 2kL = -21.97\pi$, which is close to the cold closed cavity total phase change of -22π, whereas at $\phi_r = 0.5$ the phase change is $\phi_r - 2kL = -20.13\pi$, which is close to -20π cold cavity value. The difference of

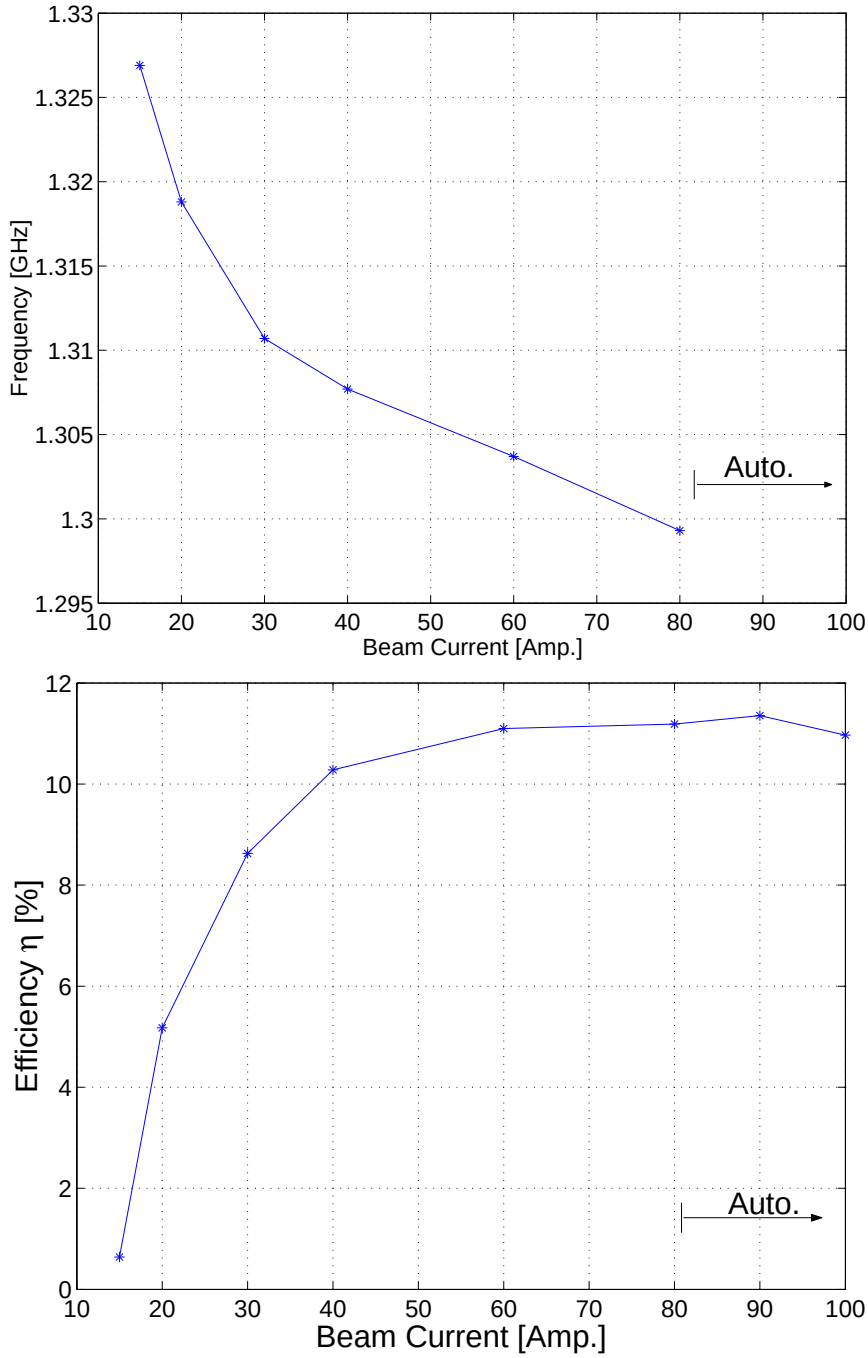

Figure 5.4: Frequency and average efficiency versus the beam current for 1D beam motion. The stationary single frequency operation is below 80 Amp. The maximum achievable efficiency for this case is about 11%.

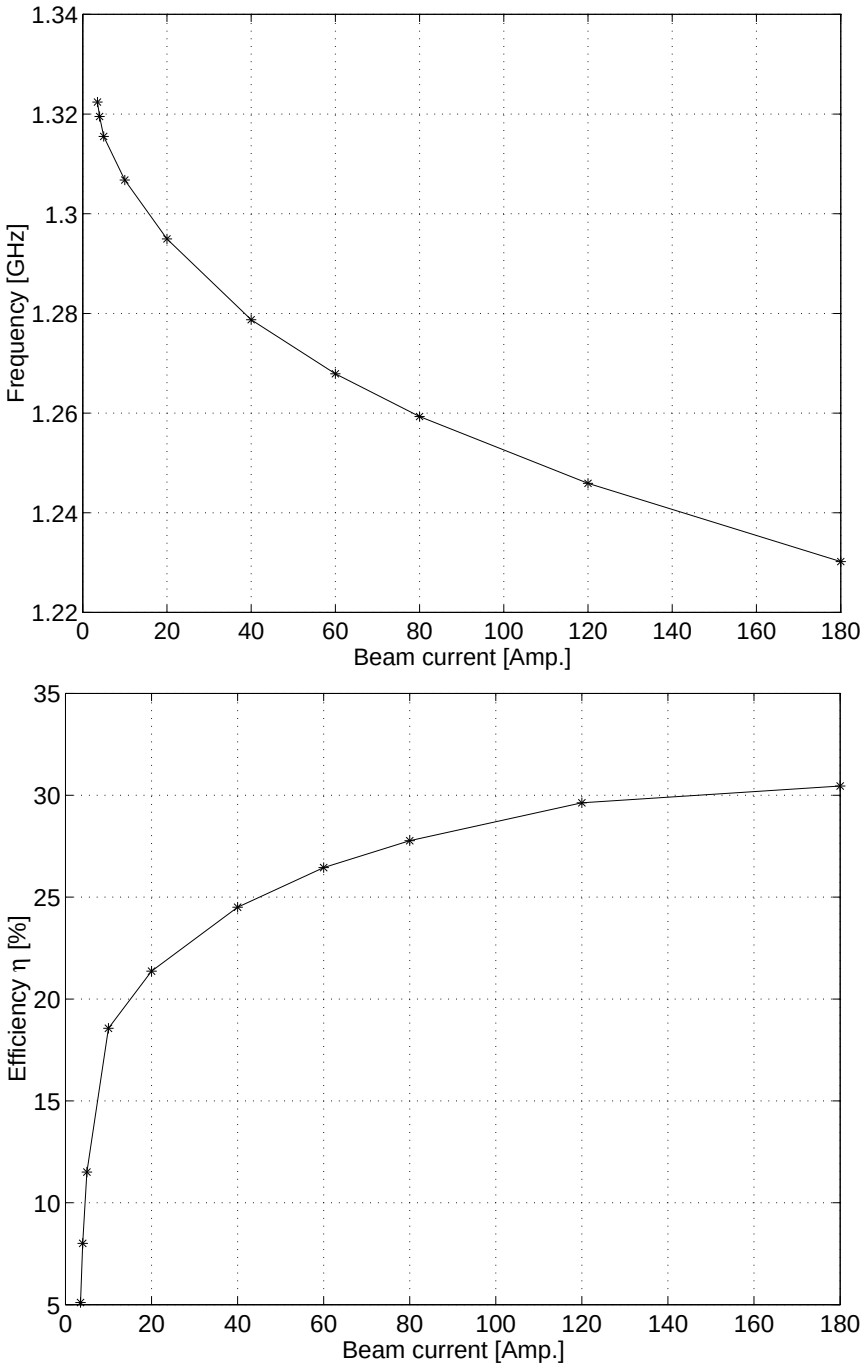

Figure 5.5: Frequency and average efficiency versus the beam current for 3D beam motion. Over all this current range, no automodulation was observed, the device operates in a single frequency stationary mode.

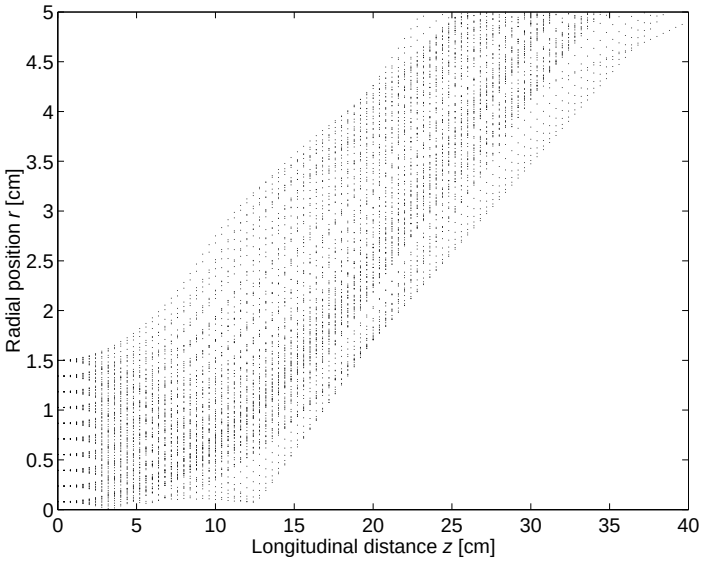

(a) I=40 Amp.

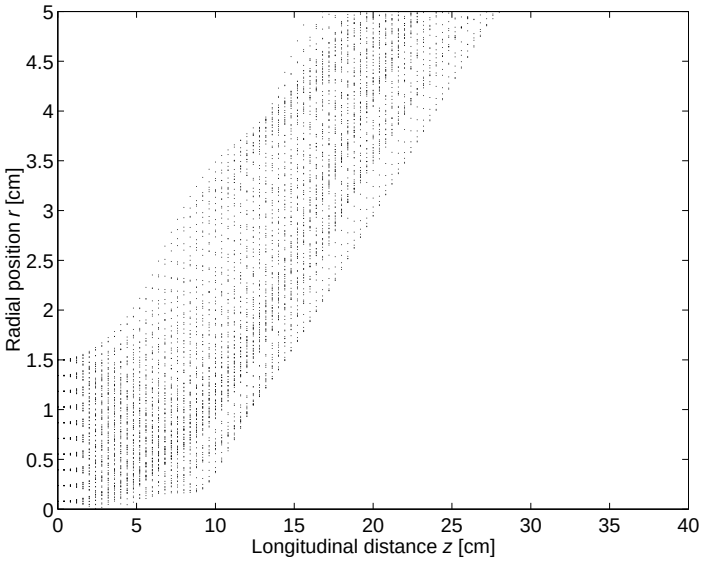

(b) I=120 Amp.

Figure 5.6: Electron radial trajectories for two different beam currents: (a)40 Amp., and (b)120 Amp. The effective longitudinal travel distance becomes shorter for larger beam currents.

total phase change by about 2π indicates the transition between two successive axial modes. The cold closed cavity resonance frequencies are represented by the dashed lines in Fig. 5.7a. Similar figures for the 3D case are shown in Fig. 5.8. The single frequency operation region get shrunk for this case where the non-stationary multi-frequency region extends between $\phi_r = 0.6\pi$ and 2π. The maximum efficiency for this case is slightly below 44% compared to 18.6% for zero reflection coefficient.

The regions of stationary single frequency operation in the $\phi_r - I_b$ plane is shown in Figs 5.9, for the 1D and 3D cases, respectively. In these figures, at each value of the current, we have a range of reflection phase ϕ_r over which we can get a single stationary frequency operation. This range of phase shrinks as we increase the current. Eventually, beyond a limiting current value, there is no stationary operation of the device. For the 1D BWO, this limiting current is about 19 Amp., and for 3D case, it is 15 Amp. (Compare this with the zero reflection case). The region of the stationary operation for the 3D BWO is smaller than their equivalence in the 1D case. The thick lines in Figs. 5.9 are the starting oscillation current calculated in section 5.5. As seen in Figs. 5.7 and 5.8, the output frequency and efficiency vary as we tune the reflection phase ϕ_r. The reflection is always tuned in the experiment using a sliding short at one termination; see Fig. 1.2. The range of efficiency and frequency tuning as a function of beam current is shown in Figs. 5.10 and 5.11, for one and 3D BWO respectively. From these figures it is evident that the frequency range shifts down with the increase of beam current (This is referred to as frequency pulling caused by beam effect.), accompanied by upshift in the efficiency range, till reaching saturation. We can also get the maximum achievable efficiency

for 0.8 reflection coefficient magnitude, which is about 18% for the 1D BWO compared with 45% for the 3D BWO.

5.7 Conclusion

A model describing non-stationary phenomena in 3D PASOTRON BWO with end reflections has been developed and used for characterizing the operation of the helix PASOTRON BWO. The results obtained have been compared with the 1D BWO. This comparison helped understanding the effect of the electron transverse motion. One observation in this study, which was also observed in the steady state model presented in chapter 4 and in Ref. [26], is that the stationary, single frequency operation of the 3D BWO is more than two times higher the 1D BWO efficiency, when all other parameters are the same. Another observation is that the efficiency enhancement is usually accompanied by a reduction in the output frequency (frequency downshift) .

In agreement with Ref. [42], when the 1D-BWO operates without reflection (R=0), auto-modulation appears at beam currents exceeding a certain value due to electron overbunching. However, such an auto-modulation is not observed in the 3D BWO model. This can be attributed to helix field configuration. The synchronous electric field has a 90° phase shift between the longitudinal and radial components. This results in a radial drift of electrons towards the outer conductor whenever overbunching starts (losses synchronism with the longitudinal component). Thus, electrons are intercepted by the outer conducting tube without performing oscillations in the overbunching regime.

In the presence of strong reflections, the high quality factor of the cavity

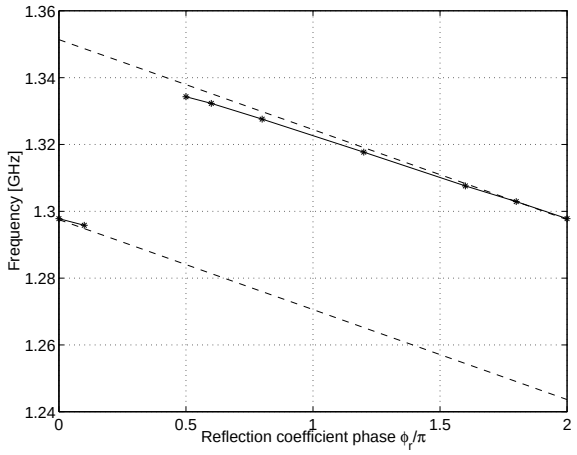

(a)

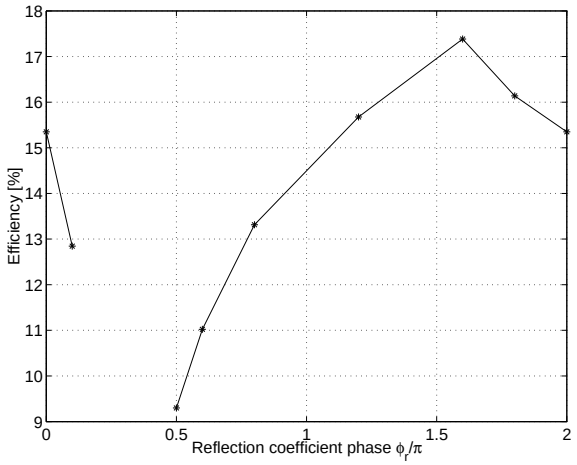

(b)

Figure 5.7: The frequency and output efficiency for the stationary mode for 1D helix BWO with reflection coefficient magnitude $|R| = 0.8$, and 10 Amp. current. The empty region between $\phi_r = 0.1\pi$ and $\phi_r = 0.5\pi$, corresponds to non-stationary multi-frequency operation region. The dashed lines in the frequency plot are the simple resonance frequency for the closed cavity (|R|=1.0) as a function of reflection phase.

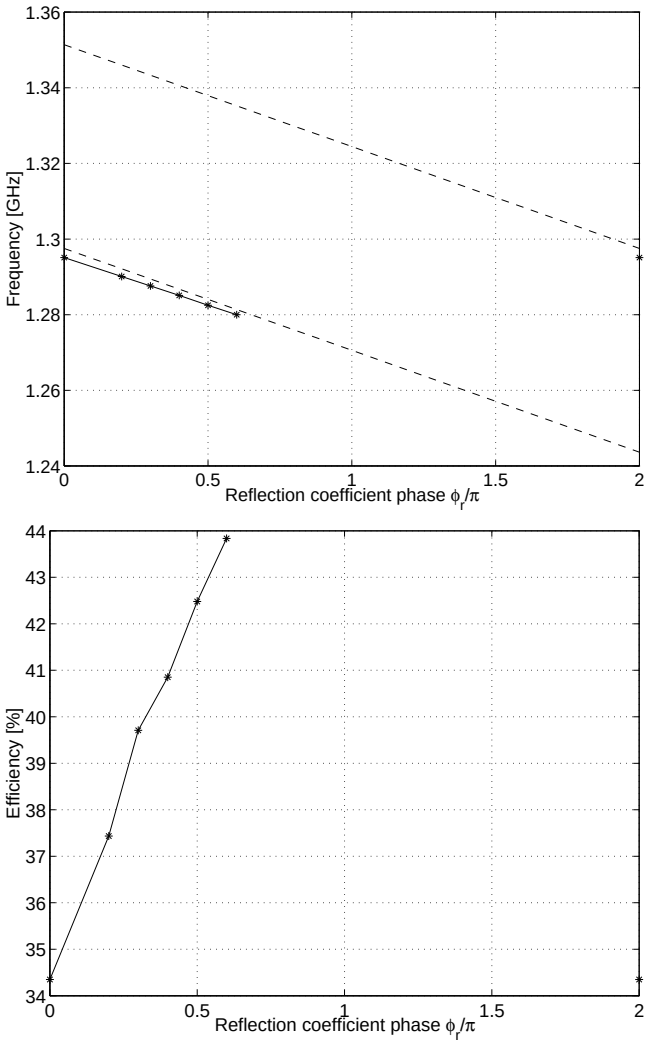

Figure 5.8: The frequency and output efficiency for the stationary mode for 3D helix PASOTRON BWO with reflection coefficient magnitude $|R| = 0.8$, and 10 Amp. current. The empty region between $\phi_r = 0.6\pi$ and $\phi_r = 2.0\pi$, corresponds to non-stationary multi-frequency operation region. The dashed lines in the frequency plot are the simple resonance frequency for the closed cavity (|R|=1.0) as a function of reflection phase.

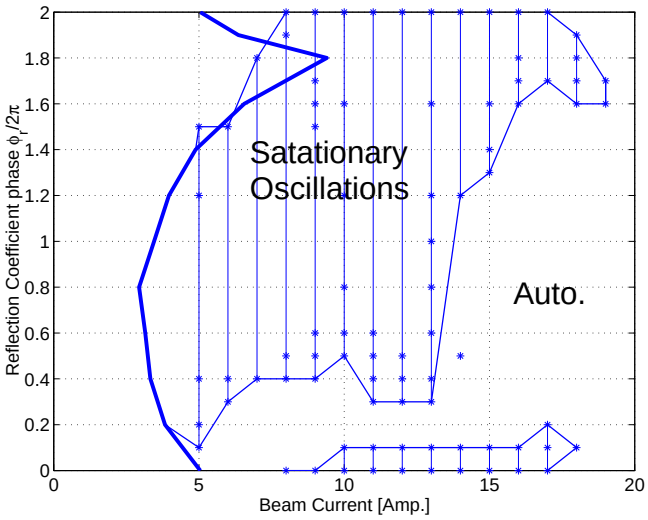

(a) 1D BWO

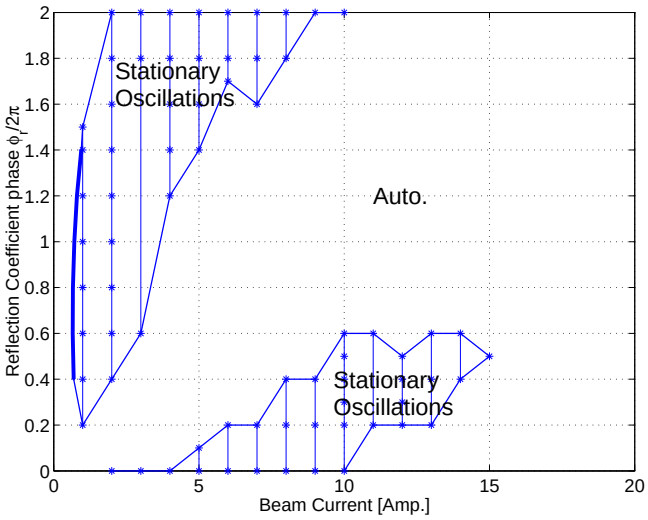

(b) 3D PASOTRON BWO

Figure 5.9: Region shaded with vertical lines is the stationary single frequency region in the $I_b - \phi_r$ plane: The thick line are the starting oscillations currents calculated in section 5.5. (The boundaries in (a) and (b) have accuracy limited to the number of points in the $I - \phi_r$ plane considered in the simulation.)

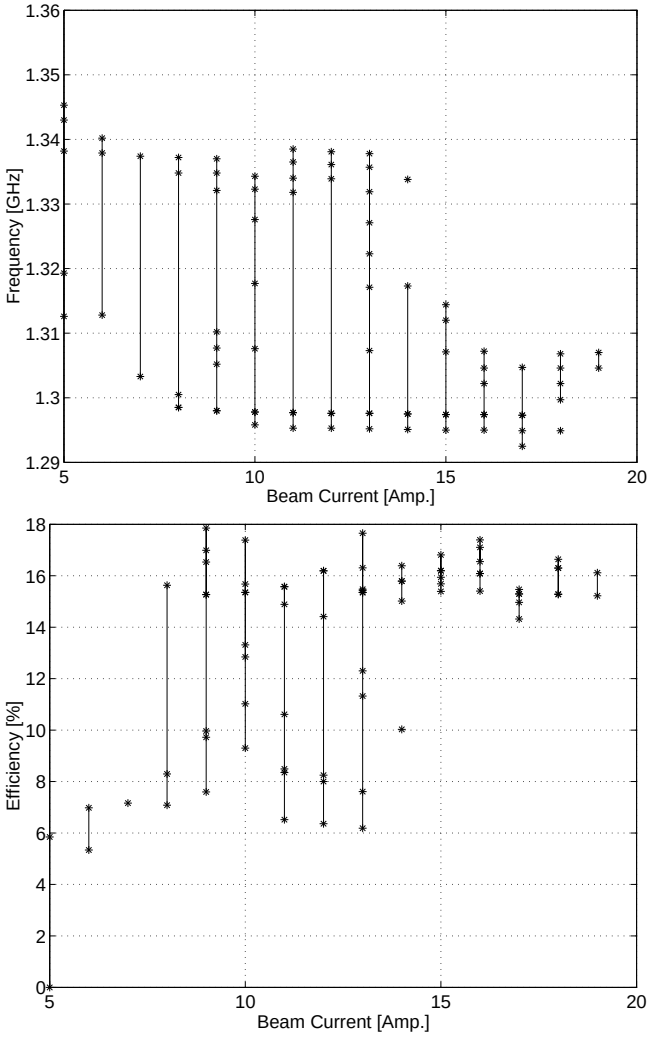

Figure 5.10: Frequency and efficiency tuning ranges for stationary single frequency operation as a function of beam current for 1D BWO.

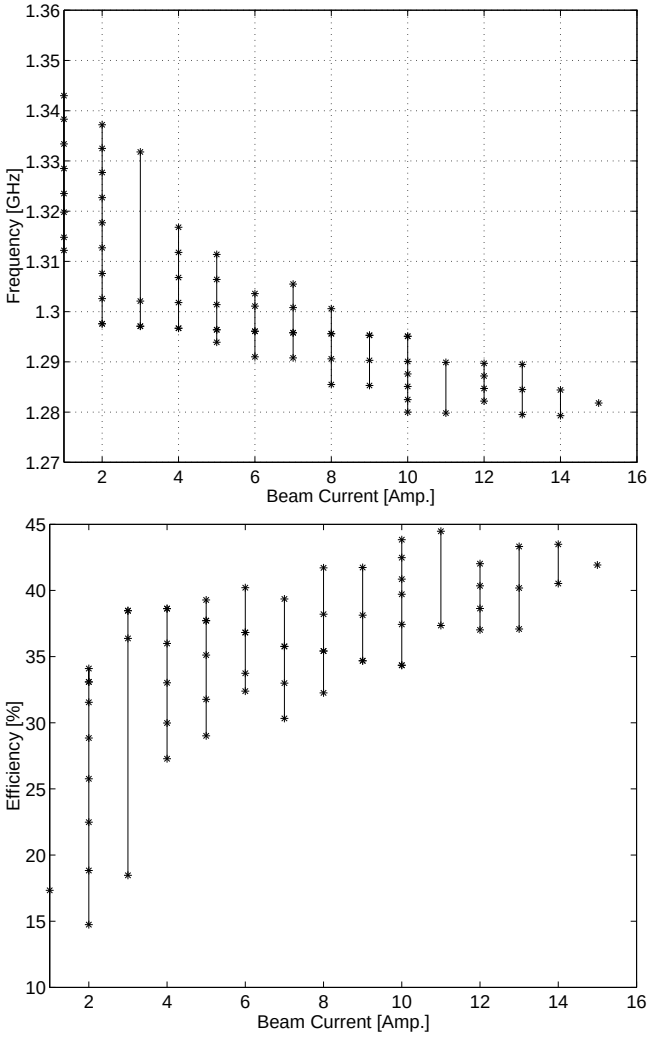

Figure 5.11: Frequency and efficiency tuning ranges for stationary single frequency operation as a function of beam current for 3D BWO.

dominates the operation of the device. The frequency of operation is very close to the closed cavity resonance frequency. The device becomes sensitive to the reflection phase. As we change the reflection coefficient phase, we pass through a transition region separating two different axial modes, where auto-modulation characterize this transition region.

Chapter 6

Summary

The dissertation discusses the theory of operation of plasma filled microwave devices, called PASOTRON (Plasma-Assisted Slow-wave Oscillator). One of the main features of these devices, is the absence of the guiding magnetic field. The electron beam transportation in these devices is provided by plasma ions, which compensate the repulsive self space charge forces of the beam. However beam electrons experience transverse motion under the action of the three components of the RF fields. This transverse motion is the major difference between these plasma devices and the conventional O-type devices, where only longitudinal motion of electrons is allowed.

The effect of this transverse motion on the operation the plasma filled tubes, was studied in chapter 2, where the tube is used as a TWT amplifier and as a BWO oscillator. The SWS structure considered is a symmetrical corrugated waveguide. This type of SWS has the maximum field intensity close to the SWS corrugated wall. So, it is desired to keep the electron beam as close as possible to the corrugated wall, in order to have strong interaction with the RF. Electron transverse motion provides the required proximity as the electrons moves radially

toward the corrugated wall. However, electron interception should be avoided at this high field intensity area. The study presented in chapter 2 deals with the tuning of the device, where a weak magnetic field can help to avoid interception, while keeping the favorable radial motion. It was shown that for TWT device this can increase the output power, whose main saturation cause is the electron interception. For the BWO PASOTRON, it was shown that the device efficiency can be enhanced, if it is long enough compared with the starting oscillation length. However the device operation deteriorate with the addition of external magnetic field, if it is slightly longer than the starting oscillation length.

The PASOTRON BWO at the university of Maryland, employs a helix loaded circular waveguide as the SWS. The helix SWS has its fields intensity concentrated around the helix, while it is almost transparent to the electrons moving transversely. This is advantageous, in terms of interaction, where electrons are exposed to the high field around the SWS, without being intercepted. A stationary "amplifier" model is presented in chapter 4. A very high efficient helix PASOTRON can be designed using that model. The model showed that electrons initially injected close to the axis, are the most efficient in giving their kinetic energy to the RF field. This can be explained by the field profile in the structure along the radial direction, where electrons initially injected close to the axis are bunched by a small field while their energy is extracted with high field close to the helix radius. So, it was shown that reducing the beam radius enhances the device electronic efficiency up to 55%. Another feature of the field profile along the radial direction for the synchronous harmonic, is that the radial and axial field components are 90^o out of phase. So when electron bunch is decelerated by the axial field component, they lose synchronization with this

component and become in phase with the radial one, which in turn expels the bunch toward the outer wall. Thus, we get rid of electrons when they begin to accelerate again. This mechanism is also a cause for efficiency enhancement of helix PASOTRON BWO.

Temporal study for the helix PASOTRON BWO is made in chapter 5. In that study, we compare the results for the 3D helix BWO with the 1D BWO. The parameters for the 1D are the same as the 3D, except of we limit the motion to be only longitudinal for the 1D case. The effect of reflections at the two device ends is studied. Two cases are separately dealt with, the zero reflection and the non-zero reflection. The results for each case is presented below.

For the zero reflection case, the 1D BWO begins to oscillate at a certain current, which is the starting oscillation current. The output efficiency increases and the frequency decreases, as we increase the beam current, until the device exhibits automodulation, where there is no more single frequency output of the BWO. Similar behavior was observed for the 3D BWO, but the output efficiency was higher. However, no automodulation was observed no matter how large we increase the beam current. This can be attributed to the 90^o phase difference between the radial and longitudinal field components of the synchronous harmonic. When the electron bunch interacting with the longitudinal components starts to perform overbunching oscillations, they become in phase with radial field which moves the electrons towards the outer tube for interception. So electrons die without performing such oscillations.

For the non-zero reflection case, the device becomes sensitive to the phase of reflection coefficient. For high quality cavity, the device operating frequency is very close to the cold closed cavity. As we change the reflection phase, the fre-

quency varies linearly until it reaches an automodulation region, characterizing a transition to another axial mode. In that automodulation region, two axial modes coexist. The regions of single frequency operation of the BWO in the parameter space formed by the beam current and reflection phase, were obtained. This region is smaller for the 3D BWO than the 1D BWO. The output of the BWO changes with the reflection phase. For each beam current value there is a range of frequency and efficiency of the device; each frequency and efficiency corresponds to a certain reflection phase. The range of efficiency is shifted up and the range of frequency is shifted down, as we increase the beam current. The output efficiencies were higher and the frequencies were lower for the 3D BWO than their values for the 1D BWO.

Appendix A

Derivation of the Envelope Evolution Equation

In this appendix the wave envelope evolution equation is derived from the Poynting theory. The Poynting theory can be written as,

$$\nabla \cdot \boldsymbol{\mathcal{S}}(\mathbf{x},t) + \frac{\partial}{\partial t} w(\mathbf{x},t) = -\boldsymbol{\mathcal{J}}(\mathbf{x},t) \cdot \boldsymbol{\mathcal{E}}_{tot}(\mathbf{x},t),$$

The quantities $\boldsymbol{\mathcal{S}}(\mathbf{x},t)$, $w(\mathbf{x},t)$, $\boldsymbol{\mathcal{J}}(\mathbf{x},t)$, and $\boldsymbol{\mathcal{E}}_{tot}(\mathbf{x},t)$ are the instantaneous Poynting vector, energy density, beam current density, and total electric field. The instantaneous current density $\boldsymbol{\mathcal{J}}(\mathbf{x},t)$ can be represented for the single frequency as,

$$\boldsymbol{\mathcal{J}}(\mathbf{x},t) = Re\{\mathbf{J}(\mathbf{x},t)e^{-i\omega t}\}, \qquad \mathbf{J}(\mathbf{x},t) = \frac{\omega}{\pi}\int_{t-2\pi/\omega}^{t} \boldsymbol{\mathcal{J}}(\mathbf{x},\tau)e^{i\omega\tau}d\tau \qquad \text{(A.1)}$$

where $\mathbf{J}(\mathbf{x},t)$ is a slowly time varying current phasor. Similarly the instantaneous fields can be written as $\boldsymbol{\mathcal{E}}_{tot} = Re\{\epsilon(z,t)\mathbf{E}_{tot}(\mathbf{x})e^{-i\omega t}\}$, and $\boldsymbol{\mathcal{B}}_{tot} = Re\{\epsilon(z,t)\mathbf{B}_{tot}(\mathbf{x})\}e^{-i\omega t}\}$, where $\epsilon(z,t)$ describes the envelope of the wave. So

the instantaneous Poynting vector and energy density can be written as,

$$\begin{aligned}\boldsymbol{\mathcal{S}}(\mathbf{x},t) &= \frac{1}{4}\frac{c}{4\pi}\left(\epsilon^2(z,t)\mathbf{E}_{tot}\times\mathbf{H}_{tot}e^{-2i\omega t}+|\epsilon(z,t)|^2\mathbf{E}_{tot}\times\mathbf{H}^*_{tot}+c.c.\right)\\ w(\mathbf{x},t) &= \frac{1}{4}\frac{1}{4\pi}\left[\epsilon^2(z,t)\left(\mathbf{E}_{tot}\cdot\mathbf{E}_{tot}+\mathbf{B}_{tot}\cdot\mathbf{B}_{tot}\right)e^{-2i\omega t}\right.\\ &\quad\left.+|\epsilon(z,t)|^2\left(|\mathbf{E}_{tot}|^2+|\mathbf{B}_{tot}|^2\right)+c.c.\right]\end{aligned} \tag{A.2}$$

The divergence for $|\epsilon(z,t)|^2\left(\mathbf{E}_{tot}\times\mathbf{H}^*_{tot}+\mathbf{E}^*_{tot}\times\mathbf{H}_{tot}\right)$ term is given as,

$$\begin{aligned}\nabla\cdot|\epsilon(z,t)|^2\left(\mathbf{E}_{tot}\times\mathbf{H}^*_{tot}+\mathbf{E}^*_{tot}\times\mathbf{H}_{tot}\right) =&\\ \epsilon^*(z,t)\frac{\partial\epsilon(z,t)}{\partial z}\hat{\mathbf{e}}_z\cdot\left(\mathbf{E}_{tot}\times\mathbf{H}^*_{tot}+\mathbf{E}^*_{tot}\times\mathbf{H}_{tot}\right)+c.c.&\end{aligned}$$

where $\mathbf{E}_{tot}$ and $\mathbf{H}_{tot}$ are the field solution inside the structure in the absence of the beam, with $\nabla\cdot\left(\mathbf{E}_{tot}\times\mathbf{H}^*_{tot}+\mathbf{E}^*_{tot}\times\mathbf{H}_{tot}\right)=0$.

Substituting in the Poynting equation and averaging over time period $2\pi/\omega$, and the cross section $S_\perp$,

$$\begin{aligned}\frac{1}{4}\epsilon^*(z,t)\frac{\partial\epsilon(z,t)}{\partial z}\frac{c}{4\pi}\int_{S_\perp}\hat{\mathbf{e}}_z\cdot\left(\mathbf{E}_{tot}\times\mathbf{H}^*_{tot}+\mathbf{E}^*_{tot}\times\mathbf{H}_{tot}\right)dS_\perp+&\\ \frac{1}{4}\epsilon^*(z,t)\frac{\partial\epsilon(z,t)}{\partial t}\frac{1}{4\pi}\int_{S_\perp}\left(|\mathbf{E}_{tot}|^2+|\mathbf{B}_{tot}|^2\right)dS_\perp+c.c.&\\ =-\frac{1}{4}\epsilon^*(z,t)\int_{S_\perp}\left(\mathbf{J}\cdot\mathbf{E}^*_{sync}\right)dS_\perp+c.c.,&\end{aligned} \tag{A.3}$$

where $\mathbf{E}^*_{sync}$ is the synchronous spatial harmonic in the Floquet series expansion. For Eq. (A.3) to be satisfied for any $\epsilon(z,t)$, we get,

$$\begin{aligned}\frac{\partial\epsilon(z,t)}{\partial z}\frac{c}{4\pi}\int_{S_\perp}\hat{\mathbf{e}}_z\cdot\left(\mathbf{E}_{tot}\times\mathbf{H}^*_{tot}+\mathbf{E}^*_{tot}\times\mathbf{H}_{tot}\right)dS_\perp+&\\ \frac{\partial\epsilon(z,t)}{\partial t}\frac{1}{4\pi}\int_{S_\perp}\left(|\mathbf{E}_{tot}|^2+|\mathbf{B}_{tot}|^2\right)dS_\perp=-\int_{S_\perp}\left(\mathbf{J}\cdot\mathbf{E}^*_{sync}\right)dS_\perp.&\end{aligned} \tag{A.4}$$

In another form,

$$\frac{\partial\epsilon(z,t)}{\partial z}+\frac{1}{v_g}\frac{\partial\epsilon(z,t)}{\partial t}=-\frac{1}{N}\int\mathbf{E}^*_{sync}\cdot\mathbf{J}dS_\perp, \tag{A.5}$$

where $\hat{\mathbf{E}}_{sync}$ is the synchronous spatial component of the Floquet expansion of $\hat{\mathbf{E}}_{tot}$ with the axial electron motion. The synchronous spatial harmonic has an axial wavenumber k. In Eq. (A.5) N and the group velocity v_g are,

$$N = \frac{c}{4\pi} \int \hat{\mathbf{a}}_z \cdot \left(\hat{\mathbf{E}}^*_{tot} \times \hat{\mathbf{B}}_{tot} + \hat{\mathbf{E}}_{tot} \times \hat{\mathbf{B}}^*_{tot} \right) dS,$$
$$v_g = 4\pi N / \int \left(\left| \hat{\mathbf{E}}_{tot} \right|^2 + \left| \hat{\mathbf{B}}_{tot} \right|^2 \right) dS.$$

Using the expression for $\mathbf{J}$ in Eq. (A.1), we get the envelope equation,

$$\frac{\partial \epsilon(z,t)}{\partial z} + \frac{1}{v_g} \frac{\partial \epsilon(z,t)}{\partial t} = -\frac{\omega}{\pi N} \int \int_{t-2\pi/\omega}^{t} \hat{\mathbf{E}}^*_{sync}(r,\theta) \cdot \mathcal{J}(\mathbf{x},z,\tau) e^{-i(kz-\omega\tau)} dS_\perp d\tau, \tag{A.6}$$

where the synchronous field is given by, $\mathbf{E}_{sync} = \hat{\mathbf{E}}_{sync} e^{i(kz-\omega t)}$. The instantaneous current density $\boldsymbol{\mathcal{J}}$ cab be represented by,

$$\boldsymbol{\mathcal{J}} = \sum_j q \mathbf{v}_j \delta(z - z_j(\tau)) \delta^2(\mathbf{x} - \mathbf{x}_j(\tau)).$$

Performing the integration in Eq. (A.6), we get,

$$\frac{\partial \epsilon(z,t)}{\partial z} + \frac{1}{v_g} \frac{\partial \epsilon(z,t)}{\partial t} = -\frac{\omega q}{\pi N} \sum \frac{\mathbf{v}_j}{v_{z_j}} \cdot \hat{\mathbf{E}}^*_{sync}(r_j,\theta) e^{-i\psi_j}. \tag{A.7}$$

For the helix SWS, it is possible to absorb the θ dependence of the synchronous harmonic in the phase $\psi = kz - \omega t - \theta$.

The summation in the above equation is over all the particle that reach the position z between the time instant $t - 2\pi/\omega$ and t. The number of particles that enter during this time period is $I(2\pi/\omega)/e$,$(q = -e)$. So, Eq. (A.7) simplifies to,

$$\frac{\partial \epsilon(z,t)}{\partial z} + \frac{1}{v_g} \frac{\partial \epsilon(z,t)}{\partial t} = \frac{2I}{N} \left\langle \frac{\mathbf{v}_j}{v_{z_j}} \cdot \hat{\mathbf{E}}^*_{sync}(r_j,\theta_j) e^{-i\psi_j} \right\rangle,$$

where the angle brackets represents averaging over both particles entrance phases $(\psi_j|_{z=0})$ and radii $(r_j|_{z=0})$. The quantity N, which is proportional to the power

flow P_r ($P_r = |N|/4$), can be substituted with an expression containing the interaction impedance Z_{int}, which is defined as,

$$Z_{int} = \frac{\left|\hat{E}_{z,sync}(R_b)\right|^2}{2k^2 P_r},$$

For the TWT, the RF power flow and the group velocity are in the same direction as the electron beam. The RF power $P_r = N/4$ and group velocity $v_g = |v_g|$ result in the following equation for the envelope evolution,

$$\frac{1}{|v_g|}\frac{\partial \epsilon(z,t)}{\partial t} + \frac{\partial \epsilon(z,t)}{\partial z} = \frac{k_1^2 Z_{int} I}{\left|\hat{E}_{z1}(R_b)\right|^2}\left\langle \frac{\mathbf{v}_j}{v_{z_j}} \cdot \hat{\mathbf{E}}^*_{sync}(r_j,\theta_j)e^{-i\psi_j}\right\rangle. \tag{A.8}$$

For the BWO, the RF power flow and the group velocity are in opposite direction to the electron beam flow. The RF power $P_r = -N/4$ and group velocity $v_g = -|v_g|$ result in the following equation for the envelope evolution,

$$\frac{1}{|v_g|}\frac{\partial \epsilon(z,t)}{\partial t} - \frac{\partial \epsilon(z,t)}{\partial z} = \frac{k_1^2 Z_{int} I}{\left|\hat{E}_{z1}(R_b)\right|^2}\left\langle \frac{\mathbf{v}_j}{v_{z_j}} \cdot \hat{\mathbf{E}}^*_{sync}(r_j,\theta_j)e^{-i\psi_j}\right\rangle. \tag{A.9}$$

Appendix B

First Harmonic Fields of Helix PASOTRON Tube

In Chapter 3, we applied the fields boundary conditions at the helix, to get the normalized fields for the n^{th} harmonic for the circular waveguide loaded with a tape helix. In this appendix we present the full expression of the first harmonic fields, which is the important harmonic to study the operation of BWO helix PASOTRON.

The normalized electric And magnetic field, denoted as $\hat{\mathbf{E}}(\rho, \theta, z; t)$ and $\hat{\mathbf{B}}(\rho, \theta, z; t)$, respectively, for the first harmonic can be written as,

$$\hat{\mathbf{E}}(\rho, \theta, z; t) = \left(-i\hat{E}_r^f(\rho)\hat{\mathbf{e}}_r + \hat{E}_\theta^f(\rho)\hat{\mathbf{e}}_\theta + \hat{E}_z^f(\rho)\hat{\mathbf{e}}_z\right) e^{i(k_1 z - \omega t - \theta)},$$

$$\hat{\mathbf{B}}(\rho, \theta, z; t) = \left(-i\hat{B}_r^f(\rho)\hat{\mathbf{e}}_r + \hat{B}_\theta^f(\rho)\hat{\mathbf{e}}_\theta + \hat{B}_z^f(\rho)\hat{\mathbf{e}}_z\right) e^{i(k_1 z - \omega t - \theta)},$$

where k_1 is the axial wavenumber for the first harmonic ($k_1 = k + 2\pi/\lambda_h$), the radial dimension r is normalized to $\rho = \kappa r$, and κ is the absolute value of the transverse wavenumber for the first harmonic ($\kappa^2 = k_1^2 - \omega^2/c^2$). The full expressions for the functions $\hat{E}_r^f(\rho)$, $\hat{E}_\theta^f(\rho)$, $\hat{E}_z^f(\rho)$, $\hat{B}_r^f(\rho)$, $\hat{B}_\theta^f(\rho)$, and $\hat{B}_z^f(\rho)$ are

$$\hat{E}_z^f(\rho) = I_1(\rho), \qquad \text{for } 0 \le \rho \le \eta, \tag{B.1a}$$

$$\hat{E}_z^f(\rho) = I_1(\eta)\frac{K_1(\zeta)I_1(\rho) - I_1(\zeta)K_1(\rho)}{K_1(\zeta)I_1(\eta) - I_1(\zeta)K_1(\eta)} \qquad \text{for } \eta \le \rho \le \zeta, \tag{B.1b}$$

$$\hat{E}_r^f(\rho) = \frac{h}{g}I_1'(\rho) + \frac{I_1(\zeta)}{I_1'(\zeta)}\frac{K_1'(\zeta)I_1'(\eta) - I_1'(\zeta)K_1'(\eta)}{K_1(\zeta)I_1(\eta) - I_1(\zeta)K_1(\eta)}\frac{\eta}{hg - \eta g^2 tan\phi}\frac{I_1(\rho)}{\rho}$$
$$\text{for } 0 \le \rho \le \eta. \tag{B.2a}$$

$$\hat{E}_r^f(\rho) = \frac{h}{g}I_1(\eta)\frac{K_1(\zeta)I_1'(\rho) - I_1(\zeta)K_1'(\rho)}{K_1(\zeta)I_1(\eta) - I_1(\zeta)K_1(\eta)} + \frac{\eta I_1'(\eta)}{hg - \eta g^2 tan\phi}\times$$
$$\frac{I_1(\zeta)}{I_1'(\zeta)}\frac{K_1'(\zeta)I_1(\rho)/\rho - I_1'(\zeta)K_1(\rho)/\rho}{K_1(\zeta)I_1(\eta) - I_1(\zeta 1)K_1(\eta)} \qquad \text{for } \eta \le \rho \le \zeta, \tag{B.2b}$$

$$\hat{E}_\theta^f(\rho) = \frac{-h}{g}\frac{I_1(\rho)}{\rho} - \frac{K_1'(\zeta)I_1'(\eta) - I_1'(\zeta)K_1'(\eta)}{K_1(\zeta)I_1(\eta) - I_1(\zeta)K_1(\eta)}\frac{I_1(\zeta)}{I_1'(\zeta)}\frac{\eta}{hg - \eta g^2 tan\phi}I_1'(\rho)$$
$$\text{for } 0 \le \rho \le \eta, \tag{B.3a}$$

$$\hat{E}_\theta^f(\rho) = \frac{-h}{g}I_1(\eta)\frac{K_1(\zeta)I_1(\rho)/\rho - I_1(\zeta)K_1(\rho)/\rho}{K_1(\zeta)I_1(\eta) - I_1(\zeta)K_1(\eta)} - \frac{\eta I_1'(\eta)}{hg - \eta g^2 tan\phi}\times$$
$$\frac{I_1(\zeta)}{I_1'(\zeta)}\frac{K_1'(\zeta)I_1'(\rho) - I_1'(\zeta)K_1'(\rho)}{K_1(\zeta)I_1(\eta) - I_1(\zeta)K_1(\eta)} \qquad \text{for } \eta \le \rho \le \zeta, \tag{B.3b}$$

$$\hat{B}_r^f = \left[\frac{K_1'(\zeta)I_1'(\eta) - I_1'(\zeta)K_1'(\eta)}{K_1(\zeta)I_1(\eta) - I_1(\zeta)K_1(\eta)}\frac{I_1(\zeta)}{I_1'(\zeta)}\frac{\eta h}{hg - \eta g^2 tan\phi}I_1'(\rho) + \frac{1}{g}\frac{I_1(\rho)}{\rho}\right],$$
$$\text{for } 0 \le \rho \le \eta. \tag{B.4a}$$

$$\hat{B}_r^f = \left[\frac{\eta h I_1'(\eta)}{hg - \eta g^2 tan\phi}\frac{I_1(\zeta)}{I_1'(\zeta)}\frac{K_1'(\zeta)I_1'(\rho) - I_1'(\zeta)K_1'(\rho)}{K_1(\zeta)I_1(\eta) - I_1(\zeta)K_1(\eta)}\right.$$
$$\left. + \frac{1}{g}I_1(\eta)\frac{K_1(\zeta)I_1(\rho)/\rho - I_1(\zeta)K_1(\rho)/\rho}{K_1(\zeta)I_1(\eta) - I_1(\zeta)K_1(\eta)}\right], \qquad \text{for } \eta \le \rho \le \zeta. \tag{B.4b}$$

$$\hat{B}_\theta^f = \left[\frac{K_1'(\zeta)I_1'(\eta) - I_1'(\zeta)K_1'(\eta)}{K_1(\zeta)I_1(\eta) - I_1(\zeta)K_1(\eta)}\frac{I_1(\zeta)}{I_1'(\zeta)}\frac{\eta h}{hg - \eta g^2 tan\phi}\frac{I_1(\rho)}{\rho} + \frac{1}{g}I_1'(\rho)\right],$$

$$\text{for } 0 \le \rho \le \eta. \quad \text{(B.5a)}$$

$$\hat{B}_\theta^f = \left[\frac{\eta h I_1'(\eta)}{hg - \eta g^2 tan\phi}\frac{I_1(\zeta)}{I_1'(\zeta)}\frac{K_1'(\zeta)I_1(\rho)/\rho - I_1'(\zeta)K_1(\rho)/\rho}{K_1(\zeta)I_1(\eta) - I_1(\zeta)K_1(\eta)}\right.$$
$$\left. + \frac{1}{g}I_1(\eta)\frac{K_1(\zeta)I_1'(\rho) - I_1(\zeta)K_1'(\rho)}{K_1(\zeta)I_1(\eta) - I_1(\zeta)K_1(\eta)}\right], \qquad \text{for } \eta \le \rho \le \zeta. \quad \text{(B.5b)}$$

$$\hat{B}_z^f = -\frac{K_1'(\zeta)I_1'(\eta) - I_1'(\zeta)K_1'(\eta)}{K_1(\zeta)I_1(\eta) - I_1(\zeta)K_1(\eta)}\frac{I_1(\zeta)}{I_1'(\zeta)}\frac{\eta I_1(\rho)}{h - \eta g tan\phi}, \qquad \text{for } 0 \le \rho \le \eta \quad \text{(B.6a)}$$

$$\hat{B}_z^f = -\frac{\eta I_1'(\eta)}{h - \eta g tan\phi}\frac{I_1(\zeta)}{I_1'(\zeta)}\frac{K_1'(\zeta)I_1(\rho) - I_1'(\zeta)K_1(\rho)}{K_1(\zeta)I_1(\eta) - I_1(\zeta)K_1(\eta)}, \qquad \text{for } \eta \le \rho \le \zeta \quad \text{(B.6b)}$$

where $\eta = \eta_1$, $\zeta = \zeta_1$, $h = k_1/(\omega/c)$ and $g = \kappa/(\omega/c)$.

REFERENCES

[1] Samuel Sensiper. Electromagnetic wave propagation on helical structures (a review and survey of recent progress). *Proceedings of the IRE*, 43:149–161, February 1955.

[2] R. Kompfner and N. T. Williams. Backward-wave tubes. *Proceedings of the IRE*, 41:1602–1611, November 1953.

[3] S. Millman. A spatial harmonic traveling-wave amplifier for six millimeters wavelength. *Proceedings of the IRE*, 39:1035–1043, September 1951.

[4] John A. Nation. On the coupling of an high-current relativistic electron beam to a slow wave structure. *Applied Physics Letters*, 17(11):491–494, 1970.

[5] N. F. Kovalev, M. I. Petelin, M. D. Raizer, A. V. Smorgonskii, and L. E. Tsopp. Generation of powerful electromagnetic radiation pulses by a beam of relativistic electrons. *JETP Letters*, 18(4):138–140, August 1973.

[6] Y. Carmel, J. Ivers, R, E. Kribel, and J. Nation. Intense coherent cherenkov radiation due to the interaction of a relativistic electron beam with a slow-wave structure. *Physical Review Letters*, 33(21):1278–1282, 1974.

[7] Yu F. Bondar, S. I. Zavorotnyi, A. L. Ipatov, N. I. Karbushev, N. F. Kovalev, O. T. Loza, G. P. Mkheidze, A. A. Ovchinnikov, A. A. Rukhadze, and L. É. Tsopp. Measurements of rf emission from carcinotron with a relativistic electron beam. *Sov. J. Plasma Phys.*, 9(2):223, 1983.

[8] S. P. Bugaev, V. I. Kanavets, A. I. Koshelev, and V. A. Cherepenin. Relativistic multiwave cherenkov generator. *Sov. Tech. Phys. lett.*, 9(11):596–597, November 1983.

[9] Alexander N. Vlasov, Anatoly G. Shkvarunets, John C. Rodgers, Yuval Carmel, Thomas M. Antonsen, Jr., Tamer M. Abuelfadl, Duan Lingze, Vladimir A. Cherepenin, Gregory S. Nusinovich, Moti Botton, and Victor L. Granatstein. Overmoded gw-class surface-wave microwave oscillator. *IEEE Transactions on Plasma Science*, 28(3):550–560, June 2000.

[10] David K. Abe, Yuval Carmel, Susanne M. Miller, Alan Bromborsky, Baruch Levuch, Thomas M. Antonsen, Jr., and William W. Destler. Experimental studies of overmoded relativistic backward-wave oscillators. *IEEE Transactions on Plasma Science*, 26(3):591–604, June 1998.

[11] A. S. El'chaninov, F. Ya. Zagulov, N. F. Kovalev, S. D. Korovin, N. V. Rostev, and A. V. Smorgonskii. Highly efficient relativistic backward-wave tube. *Sov. Tech. Phys. Lett.*, 6(4):191–192, April 1980.

[12] K. Minami, Yuval Carmel, Victor L. Granatstein, William W. Destler, Weiran Lou, D. K. Abe, R. Alan Kehs, M. M. Ali, T. Hosokawa, K. Ogura, and T. Watanabe. Linear theory of electromagnetic wave generation in a

plasma-loaded corrugated-wall resonator. *IEEE Transactions on Plasma Science*, 18(3):537–545, June 1990.

[13] Anatoly G. Shkvarunets, Satoru Kobayashi, James Weaver, Yuval Carmel, John Rodgers, Thomas M. Antonsen, Jr., and Victor L. Granatstein. Electromagnetic properties of corrugated and smooth waveguide filled with radially inhomogeneous plasma. *IEEE Transactions on Plasma Science*, 24(3):905–917, June 1996.

[14] Dan M. Goebel, Yuval Carmel, and Gregory S. Nusinovich. Advances in plasma-filled microwave sources. *Physics of Plasmas*, 6(5):2225–2232, May 1999.

[15] Y. Carmel, K. Minami, R. A. Kehs, W. W. Desteler, V. L. Granatstein, D. Abe, and W. L. Lou. Demonstration of efficiency enhancement in a high-power backward-wave oscillator by plasma injection. *Physical Review Letters*, 62(20):2389–2392, May 1989.

[16] K. Minami, W. R. Lou, W. W. Destler, R. A. Kehs, V. L. Granatstein, and Y. Carmel. Observation of a resonant enhancement of microwave radiation from a gas-filled backward wave oscillator. *Applied Physics letter*, 53(7):559–561, August 1988.

[17] M. A. Zavjalov, L. A. Mitin, V. I. Perevodchicov, V. N. Tskhai, and A. L. Shapiro. Powerful wideband amplifier based on hybrid plasma-cavity slow-wave structure. *IEEE Transactions on Plasma Science*, 22(5):600–607, October 1994.

[18] Saturo Kobayashi, Thomas M. Antonsen, Jr., and Gregory S. Nusinovich. Linear theory of a plasma loaded, helix type, slow wave amplifier. *IEEE Transactions on Plasma Science*, 26(3):669–679, June 1998.

[19] R. B. Miller. *Intense Charged Particle Beams*, chapter 4, pages 139–191. Plenum Press, New York, 1982.

[20] D. M. Goebel, J. M. Butler, R. W. Schumacher, J. Santoru, and R. L. Eisenhart. High-power microwave source based on an unmagnetized backward-wave oscillator. *IEEE Plasma Science*, 22(5):547–553, October 1994.

[21] Dan M. Goebel, E. A. Adler, S. Ponti, J. R. Feicht, Robert L. Eisenhart, and Raymond W. Lemke. Efficiency enhancement in high power backward-wave oscillators. *IEEE Plasma Science*, 27(3):800–809, June 1999.

[22] D. M. Goebel, E. S. Ponti, R. L. Eisenhart, and R. W. Lemke. Frequency and power response of high-power plasma-filled backward-wave oscillators. *Physics of Plasmas*, 6(6):2319–2322, June 1999.

[23] W. H. Bennett. Magnetically self-focusing streams. *Phys. Rev.*, 45:890, June 1934.

[24] G. S. Nusinovich and Yu P. Bliokh. Cherenkov radiation of electromagnetic waves by electron beams in the absence of an external magnetic field. *Physical Review E*, 62(2):2657–2666, August 2000.

[25] T. M. Abuelfadl, G. S. Nusinovich, A. G. Shkvarunets, Y. Carmel, T. M. Antonsen, Jr., and Dan Goebel. Traveling-wave tubes and backward-wave oscillators with weak external magnetic field. *Physical Review E*, 63, 2001. article no. 066501.

[26] T. M. Abu-elfadl, G.S. Nusinovich, A.G. Shkvarunets, Y. Carmel, T. M. Antonsen, Jr., V. L. Granatstein, and D. M. Goebel. Efficiency of helix pasotron backward wave oscillator. *IEEE Transactions on Plasma Science*, June 2002. To be published.

[27] A. G. Shkvarunets, Y. Carmel, G. S. Nusinovich, T. M. Abuelfadl, J. Rodgers, T. M. Antonsen, Jr., V. Granatstein, and D. M. Goebel. Realization of high efficiency in a plasma-assisted microwave source with two-dimensional electron motion. *Physics of Plasmas*, 9(10):4114–4117, October 2002.

[28] J. R. Pierce. *Traveling-Wave Tubes*, chapter 13, pages 168–181. Van Nostrand, Toronto, 1950.

[29] N. F. Kovalev and A. V. Smorgonskiy. The theory of an ultra-relativistic twt. *Radio Engineering and Electronic Physics*, 20(6):133–136, June 1974.

[30] H. R. Johnson. Backward-wave oscillators. *Proceedings of the IRE*, 43:684–697, June 1955.

[31] B. Levush, T. M. Antonsen, Jr., A. Bromborsky, Wei-Ran Lou, and Y. Carmel. Theory of relativistic backward-wave oscillators with end reflections. *IEEE Plasma Science*, 20(3):263–280, June 1992.

[32] David Chernin, T. M. Antonsen, Jr., and Baruch Levush. Exact treatment of the dispersion and beam interaction impedance of a thin tape helix surrounded by a radially stratified dielectric. *IEEE Transactions on Electron Devices*, 46(7):1472–1483, July 1999.

[33] T. M. Antonsen, Jr. and Baruch Levush. Christine: A multifrequency parametric simulation code for traveling wave tube amplifier. Technical report, Naval Research Laboratory, May 1997. NRL/FR/6840-97-9845.

[34] Dean A. Watkins. *Topics in Electromagnetic Theory*, chapter 2, pages 39–54. John Wiley and Sons, Inc., 1958.

[35] Hans A. Uhm and Joon Y. Choe. Properties of electromagnetic wave propagation in a helix-loaded waveguide. *Journal of Applied Physics*, 53(12):8483–8488, December 1982.

[36] Hans A. Uhm and Joon Y. Choe. Electromagnetic-wave propagation in a conducting waveguide loaded with a tape helix. *IEEE Transactions on Microwave Theory and Technologies*, 31(9):704–710, September 1983.

[37] G. S. Nusinovich, Y. P. Bliokh, T. M. Abue-Elfadl, A. G. Shkvarunets, D. M. Goebel, Y. Carmel, T. M. Antonsen, Jr., and V. L. Granatstein. Recent progress in understanding the physics of plasma-filled, high-power microwave sources. In Bruce E. Carlsten, editor, *High Energy density and High Power Rf: 5^{th} Workshop*, volume 625, pages 45–53, Melville, New York, 2002. U.S. Dept. of Energy, Office of Science and High Energy Physics Division, American Institute of Physics.

[38] Martin Reiser. *Theory and Design of Charged Particle Beams*, chapter 2, page 31. John Wiley and Sons, Inc., 1994.

[39] Herbert Goldstein. *Classical Mechanics*, chapter 9, page 378. Addison-Wesley Publishing Company, Inc., 1980.

[40] N. F. Kovalev and V. I. Petrukhina. Ultra-relativistic carcintron with a step-profile coupling impedance. *Elektronnaya Tekhnika, Ser. 1, Electronika SVCh*, (7):102–105, 1977.

[41] Y. Carmel, A. G. Shkvarunets, G. S. Nusinovich, T. Abu-Elfadl, T. Antonsen, Jr., and J. Rodgers. Progress in the pasotron theory and experiments. In *The 28th IEEE International Conference on Plasma Science and the 13th International Pulsed Power Conference, IEEE Conference Record-Abstracts*. The Plasma Science and Applications Committee and The Pulsed Power Science and Technology Committee of The IEEE nuclear and Plasma Sciences Society, IEEE, 2001.

[42] N. S. Ginzburg, S. P. Kuznetsov, and T. N. Fedoseeva. Theory of transients in relativistic backward-wave tubes. *Radiophysics and Quantum Electronics*, 21(7):728–39, July 1978.

[43] A. N. Vlasov, G. S. Nusinovich, and B. Levush. Effect of the zero spatial harmonic in a slow electromagnetic wave on operation of relativistic backward-wave oscillators. *Physics of Plasmas*, 4(5):1402–1412, 1997.

[44] N. M. Ryskin and V. N. Titov. Self-modulation and chaotic regimes of generation in a relativistic backward-wave oscillator with end reflections. *Radiophysics and Quantum Electronics*, 44(10):793–806, 2001.